NEUTRAL STRANGE PARTICLE PRODUCTION IN RELATIVISTIC CU+CU COLLISIONS AT $\sqrt{s_{NN}} = 200$ GeV

by

ANTHONY ROBERT TIMMINS

A thesis submitted to
The University of Birmingham
for the degree of
DOCTOR OF PHILOSOPHY

School of Physics and Astronomy
The University of Birmingham

July 10, 2008.

Synopsis

Collisions of relativistic heavy-ions aim to create a unique state of matter, where quarks and gluons over can move over large volumes in comparison to typical size of a hadron. This state is known as the *Quark Gluon Plasma* (QGP), and it is believed that the universe temporally existed in such a state shortly after the big bang. It is also expected to have larger numbers of strangeness carriers relative to a hadronic gas due to a drop in the strange quark's dynamical mass. This thesis reports measurements of strange baryon and meson V0 yields from Cu+Cu $\sqrt{s_{NN}} = 200$ GeV collisions, which reveal that collision geometry plays a crucial role for strangeness production. Relative to Au+Au collisions with similar numbers of participating nucleons, $\langle N_{part} \rangle$, at the same energy, Cu+Cu collisions with $\langle N_{part} \rangle \gtrsim 60$ exhibit higher mid-rapidity integrated yields for the Λ, $\bar{\Lambda}$, K^0_S particles. Beyond the phase space region associated with bulk strangeness production, higher mid-p_T ($2 \lesssim p_T \lesssim 5$ GeV/c) Λ/K^0_S ratios are observed in Cu+Cu compared to Au+Au in the overlapping $\langle N_{part} \rangle$ range. Nuclear modification factors are measured which reveal high-p_T ($p_T \gtrsim 5$ GeV/c) suppression occurs for strange particle yields in central Cu+Cu $\sqrt{s_{NN}} = 200$ GeV collisions. Implications with respect to QGP formation are discussed.

Author's Contribution

As member of the STAR experiment at the Relativistic Heavy-Ion Collider, the author has contributed in a number of ways to experimental operations. Detailed in chapter 4, for the Cu+Cu $\sqrt{s_{NN}} = 200$ GeV data-set, the author developed pile-up rejection methods and determined centrality parameters which are experiment wide in terms of their use. The author developed a momentum re-weighting method for V0 corrections which is currently used in the strangeness working group for a number of analyses (chapter 5). The author helped in the quality assurance drive for the SVT detector by evaluating the vertex finding performance and momentum resolution when SVT hits were included in tracking, worked on experimental shifts for a total of five weeks, attended experimental meetings where talks were given, and participated in phone conferences on a weekly basis.

Regarding the V0 yield extraction in chapter 5, the author tuned cuts, determined a method for calculating the feed down contribution to Λ, $\bar{\Lambda}$ yields and determined systematic uncertainties for V0 yields. The author was privileged enough to present his P.h.D. work on strangeness production at two major international conferences. This took the form of a poster at Quark Matter 2006 (Shanghai, China), and a talk at Strange Quark Matter 2007 (Levoča, Slovakia). In both cases, the proceedings were referee reviewed and consequently accepted with the references being J. Mod. Phys. E16, 2055 (2007) and J. Phys. G: Nucl. Part. Phys. 35 (2008) 044062 respectively. A talk was also given at the Institute of Physics conference at Guildford, UK in 2007. Finally, the author was invited to give two seminars; one at Yale University, USA and other at The University of Birmingham, UK.

Acknowledgements

First and foremost, I would like thank Dr Peter Jones for giving me the opportunity to work on the cutting edge of fundamental physics at the STAR experiment, and for providing excellent guidance and support throughout my P.h.D. As with past, present, and future students in the Birmingham Relativistic Heavy-Ion group, his careful reading of this document has risen the standard immensely. I would also like to thank the other senior members of the RHI group: Professor John Nelson who introduced me to world of high energy nuclear physics in my undergraduate years, Dr Lee Barnby who acted as an excellent mentor and edited/ran the STAR embedding software for the corrections in this thesis (no easy task!), and Dr Marek Bombara who in addition to giving me sound scientific advice, provided many rent free nights at his flat in my write up year. I am very grateful to the past and present RHI students John, Léon, Tom, and Essam for all the discussions and help they have given me and I almost certainty owe them a beer (cider in Tom's case) or two. I also extend my gratitude to past and present members of Birmingham Nuclear Group: Gary, Martin, Gordon, Paul J, Victor, Neil, Nic, Dave F, Tom B, Dave P, Paul M, Mark H, Matt G, Louise, Pete, and Tom L, and Mark B.

As a member of the Strangeness Physics Working Group at STAR, I am hugely indebted to my fellow members who provided valuable input throughout my P.h.D. Thanks Matt, Helen, Rene, Jun, Marcelo, Christine, Betty, Sevil, Mark, Christina, Xiaobin, Gene, and Richard: it has been a privilege to work along side so many talented and dedicated scientists. Outside of the Strangeness PWG, I would like to thank Jerome Laurent, Nu Xu, and Bedanga Mohanty for the personal encouragement they gave me in the later stages of my P.h.D. I am also grateful to James Dunlop, Lanny Ray, and Tom Trainor for the insightful discussions on Cu+Cu centrality, and Marco Van Leeuwen who wrote a very accomplished vertex finder which I had the pleasure of testing. I would like to thank Terry, Jason, and Oana for their

friendship at the many of the STAR meetings and shifts. Finally, I thank all the members of the STAR software and operations teams as their hard work made this thesis possible.

Beyond my scientific endeavours, I have been very lucky to have a brilliant set of friends in Birmingham throughout my university years. Thanks Anna, Becca, Chris B, Chris R, Helen, Fred, Gaz, Ginge, Kate, Kemi, Ian H, Ian O, Jersey, Laura B, Laura C, Lauren, Liz, Marianne, Mike B, Mike C, Ro, Rachel D, Rachel N, Russell, Webbie and Will for all the great times. In particular, I thank Simon Hughes who despite my intimate knowledge of his university years, has asked me to be best man at his forth coming wedding. In the same regard, I thank all the lads from home: Dom, Tom, Kink, Matt, Pickle, Greg and Dan F for being great mates throughout my school years and beyond. As you all know, we were all hugely privileged to have fantastic schooling, and (for better or worse ;-)) and all made the most of our time. Finally, I thank my family for the boundless love and support they have provided throughout my education. The joy of completing this chapter in my life, is as much theirs, as it is mine.

Dedication

Whatever good may come of my work, I dedicate to my grandfather Leslie Ernest Timmins and my grandmother Soad Estanphonus, who both passed away while this thesis was being written. May God bless their souls...

Gloria Dei est celare verbum, et gloria regum investigare sermonem...

Proverbs 25:2

Contents

List of Figures

List of Tables

Chapter 1

INTRODUCTION

Characterising the interactions between quarks and gluons, the strong force has perhaps been the most challenging of all the fundamental forces to understand. Quantum Chromodymamics (QCD) is a Quantum Field theory used to describe the strong interaction. At large momentum transfers between partons (quarks and gluons), perturbative QCD (pQCD) has been shown to describe the coupling to a very high level of precision [1, 2]. When the scale of the momentum transfer approaches infinity, the coupling strength tends to zero and this is known as *Asymptotic Freedom*. At low momentum transfers, the QCD coupling strength becomes large and requires non-perturbative methods such as lattice gauge calculations to describe the underlying dynamics.

This chapter will proceed to review all of these concepts and describe a state of matter predicted by QCD; the *Quark Gluon Plasma* (QGP). It will then give a brief description of two signatures proposed for QGP formation, and finish with an outline of the work contained in this thesis.

1.1 Quarks and Gluons

After the discovery of a wealth of baryon and meson resonances, *the quark model* was proposed to account for the respective hadron constituents [3]. The model's principle assumption was that a baryon consisted of three quarks, and a meson of a quark anti-quark pair. Taking the lead from the Rutherford scattering experiments, deep-inelastic scattering experiments then showed that nucleons did indeed contain point-like fractionally charged fermions [4]. These experiments demonstrated that the constituent quarks have an electrical charge of either $+2/3$ or $-1/3$, carry a third of the nucleon mass, and in total only half of the nucleon's momentum. It was therefore proposed the missing half should be attributed to the force carrier that binds the quarks, the *gluon*. In 1979, direct experimental evidence for the existence of the gluon emerged via the observation of 3-jet events in $e^+ + e^-$ collisions [6]. Collectively, quarks and gluons are known as *partons* and the properties of all the known quarks are shown in table 1.1.

Name	Symbol	Mass (MeV)	Charge (e)	Quantum Number
Up	u	$1.5 \rightarrow 4$	$+\frac{2}{3}$	Isospin $= +\frac{1}{2}$
Down	d	$3 \rightarrow 8$	$-\frac{1}{3}$	Isospin $= -\frac{1}{2}$
Strange	s	$80 \rightarrow 130$	$-\frac{1}{3}$	Strangeness = -1
Charm	c	$1150 \rightarrow 1350$	$+\frac{2}{3}$	Charm = +1
Bottom	b	$4100 \rightarrow 4400$	$-\frac{1}{3}$	Bottom = -1
Top	t	$174300 \pm 5\ 100$	$+\frac{2}{3}$	Top = +1

Table 1.1: The bare quark masses. Name, mass, charge and quantum number of the discovered quarks [7].

Despite the initial success of the quark model, the discovery of the Δ^{++} and Ω^- particles posed a problem. Each particle contained three identical quarks with parallel spins and identical s-wave states. As quarks are fermions, the described state violates the Pauli Exclusion Principle. A new quantum number, colour charge, was thus introduced as the source of colour which binds quarks within hadrons via

the strong interaction [5]. For Quantum Electrodynamics (QED), the analogy is electrical charge. The binding associated with the strong interaction requires each quark to have a different colour quantum number so the Pauli Exclusion Principle is not violated. As this quantum number is not observed in nature it must sum to zero. The values are red, blue, green, anti-red, anti-green, anti-blue. The combination red, green, blue sums to zero, as does anti-red, anti-blue and anti-green. Two oppositely colour charged values such as red and anti-red will also sum to zero. Baryons such as the proton will contain the three colour combination and anti-baryons the three anti-colour. Mesons such as the pion will contain two oppositely charged colours.

When Standard Model techniques are used to describe the strong interaction, the exchange boson which is the gluon, is calculated to be doubly charged with a colour/anti-colour combination. For two quarks participating in the strong interaction, colour can be transported and this is demonstrated in figure 1.1. All strong interactions require the conservation of total colour charge just as QED requires the conservation of electrical charge. However, as the gluon carries colour, this adds an extra layer of complexity in calculating the strong potential as, unlike QED, the exchange particles can interact with themselves.

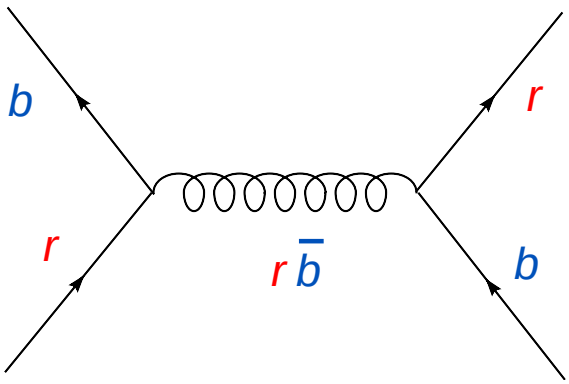

Figure 1.1: A Feynman diagram representing colour exchange in the strong interaction. The lines represent the singly charged quarks, and the curves represent the exchanged doubly charged gluon.

1.2 The Strong Potential

The non Abelian potential that characterises the strong force between two interacting quarks, such as those in a meson, may be written as follows:

$$V(r) = -\frac{4\alpha_s}{3r} + kr \tag{1.1}$$

where r is the distance between the two quarks, α_s the running coupling constant, and k is the string constant which is usually quoted as $\simeq$ 850 MeV fm^{-1} [5]. It is clear that at small distances the potential is coulomb like as the first term dominates, while a large distances the potential grows linearly with distance as the second term dominates.

1.2.1 Small Distance Behaviour

The running coupling constant in equation 1.1 depends on the momentum transfer, and can be given by following equation:

$$\alpha_s(q^2) = \frac{\alpha_0}{1 + (\beta_1/4\pi)\alpha_0 \ln\left(\frac{q^2}{u^2}\right)} \tag{1.2}$$

where q^2 is the square of momentum transfer in the interaction, and α_0 is the value of the coupling when $q^2 = u^2$ [1]. The relation is derived from the first two terms of the renormlisation group equation in Quantum Field Theory, which essentially maps a predicted α_s from a measured α_0. The coefficient β_1 is defined as:

$$\beta_1 = (11N_c - 2n_f)/3. \tag{1.3}$$

where N_c is number of charges involved in the boson exchange, and n_f is the number of fermions flavours that may form a loop in the boson exchange [5]. For QCD

coupling, $N_c = 3$ (three color charges) and $n_f = 6$ (six quark flavours) which gives $\beta_1 = 5$. The coupling shown in equation 1.3 is equally applicable for QED which in this case, $N_c = 0$ (photon carries no electric charge) and $n_f = 6$ (six leptons) which gives $\beta_1 = -4$. The differing β_1 sign leads to dramatically different behaviour for the QED coupling compared to QCD with increasing q^2; the QED coupling constant increases as the dominator in equation 1.2 decreases, while the strong coupling constant decreases as the dominator increases. Regarding the strong coupling constant, in order to re-express the α_0 and u^2 as a single value, equation 1.2 can be rewritten as:

$$\alpha_s = \frac{4\pi}{5\ln\left(\frac{q^2}{\Lambda^2_{QCD}}\right)} \tag{1.4}$$

where $\Lambda^2_{QCD} = u^2\exp\{4\pi/7\alpha_0\}$. Λ_{QCD} is known as the QCD scale constant, and can experimentally determined by measuring α_s at various values of q^2; a typically quoted value is $\Lambda_{QCD} \simeq 200\text{MeV}$ [8]. A high momentum transfer ($q^2 \gg \Lambda^2_{QCD}$) will involve a short-range interaction, and these are typically known as *hard processes*. In this case, the potential shown by equation 1.1 will tend to zero, as the strong coupling constant tends to zero at a faster rate than the distance. It is this dependence on q^2 that leads to α_s being called the running coupling constant. When the potential becomes small, this enables the use of perturbation methods to calculate physical quantities such as cross sections at high energies. This is referred to as *perturbative regime* and corresponds to $\alpha_s \ll 1$.

The underlying microscopic processes behind this relation can be explained as follows. Heinsberg's Uncertainly Principle allows virtual particle creation and destruction within the vacuum. Regarding QED, if an electron is placed in the vacuum, the virtual electron-positron pairs subject to $\Delta E \Delta\, t \geq \hbar/2$, are polarised in a way which brings the virtual positrons closer to real electron. This serves to screen the real electron's effective charge relative to the bare charge (1e). As closer distances are probed, the real electron's charge is more "visible" leading to the effective charge

tending to the bare charge. The respective coupling constant consequently increases with decreasing distance which leads to point like interactions for high momentum transfers. For QCD, the situation is somewhat reserved. If a real quark (or gluon) is inserted into the vacuum, the created virtual quark anti-quark pairs are also polarised in the vicinity. However, the colour charged gluons that are subsequently exchanged inhibit the screening effect, and as distances closer to the quark are probed (via another quark), the anti-screeing provided by the gluons actually serves to reduce the effective quark colour charge.

1.2.2 Long Distance Behaviour

At large distances ($r \gtrsim 1$ fm), the second term in equation 1.1 begins to dominate and the potential becomes proportional to the distance. Such linear behaviour again supports the idea that gluons carry colour charge, and can thus interact with themselves. This is shown schematically in figure 1.2 where the colour flux lines between two quarks are essentially pulled together by the interacting force mediators (gluons). The dependance also supports the reason why free quarks are never seen in nature. Contrary to what happens for the electromagnetic interaction between two charges, if two quarks are "pulled apart", the potential energy will increase with distance. At some point this potential energy will be larger than what is needed to produce a quark anti-quark pair, and when energetically favourable, such a pair will be produced. The process is also illustrated in figure 1.2 and is known as *string fragmentation*.

For hadron production in high energy elementary p+p collisions, fragmentation is often classified into two categories. *Transverse fragmentation* involves a high angle parton scatter relative to the beam axis in which the parton is "dislodged" from proton. The string is stretched in the direction transverse to the beam to produce a *jet*, or cluster of hadrons in the final state, with a total momentum and energy

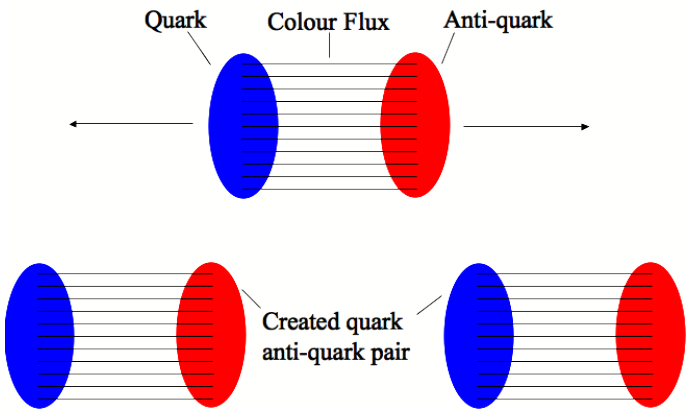

Figure 1.2: A diagram illustrating the linear nature of the strong potential, and particle production via string breaking.

equal to that of the initially scattered parton. As described previously, if the q^2 is high enough the scattering probability is pQCD calculable (short range behaviour), however the fragmentation processes (long range behaviour) are not. *Longitudinal fragmentation* involves small angle parton scatters, i.e with low q^2, thus neither the scattering nor the hadronisation process can be described with pQCD. As a result, phenomenological descriptions such as the Lund string model [9] are often used to describe both of these fragmentation processes.

1.3 Deconfinement

In the partonic sense, deconfinement is characterised by quarks and gluons that are able to move over larger distances than that of the size of a nucleon ($\sim$ 1 fm). This is believed to occur in two scenarios; either at very high energies where the parton's effective colour charge approaches zero (asymptotic freedom), or at high density where the hadronic wave functions overlap delocalising the partons (Debye screening). The *Quark Gluon Plasma* (QGP), which may occur for either of the two scenarios, is thus a bulk state of quark and gluon matter where the degrees of freedom are colour charged. The universe was expected to exist in such a state

$\sim 10\mu$s after the Big Bang [11]. Figure 1.3 shows expected phase diagram for hadronic matter. The early univserse lies in the high temperature low net baryon density domain where the amount of matter and anti-matter were approximately equal. It is also possible that the high baryon density and low temperature core of a neutron star, may contain colour superconducting matter [12]. The possible critical point will be discussed later.

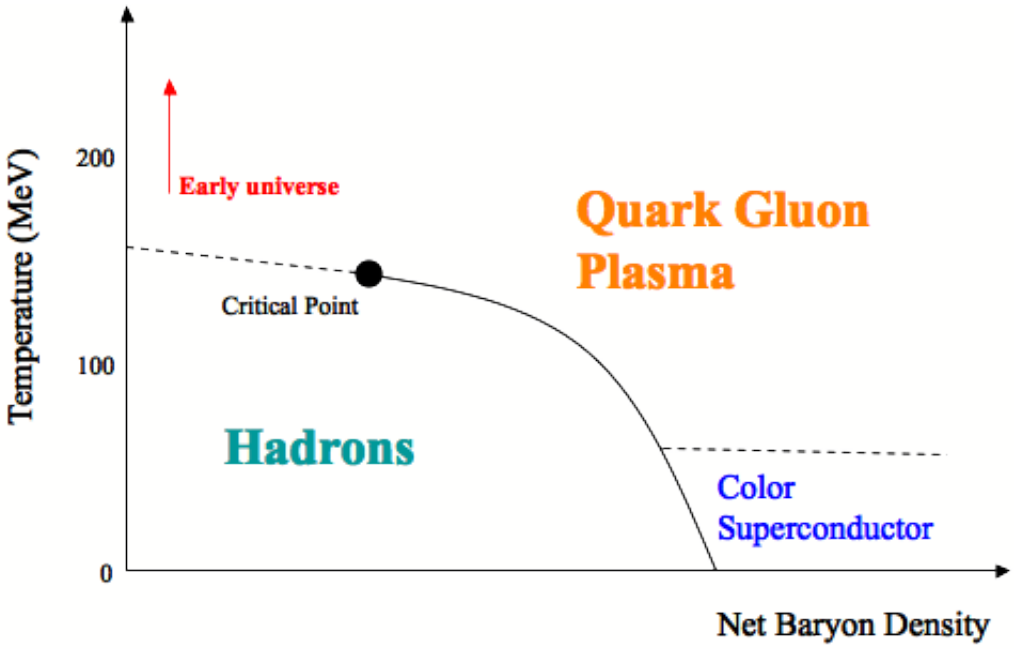

Figure 1.3: The QCD Phase Diagram.

1.3.1 Asymptotic Freedom and Debye Screening

Partons are known to be asymptotically free for high momentum transfers which allows for the existence of QGP where the equation of state corresponds to a high temperature ideal gas, i.e. $T \gg \Lambda_{QCD}$. In this case, the energy density, ϵ, and temperature, T, are simply related by:

$$\frac{\epsilon}{T^4} = (16 + \frac{21}{2} n_f) \frac{\pi^2}{30} \tag{1.5}$$

where n_f is the number of quark flavours [13]. The equation is applicable when the degrees of freedom are non-interacting, and there are similar numbers of anti-quarks and quarks (low net baryon density). It is known as the Stefan-Boltzmann Law.

In addition to asymptotic freedom, deconfinement can also manifest itself via Debye screening. In contrast to the high temperatures required for an asymptotically free QGP, deconfinement is achieved with a compression of hadronic matter which leads to partons from one hadron interacting with partons from another. It then becomes impossible to class partons as localised in confined hadrons, thus deconfinement is achieved. In this scenario, long range interactions are screened with the Deybe radius r_D characterising the screening distance. When r_D becomes less than the nucleon radius, parton delocalisation will occur. An analogous process occurs in condensed matter and this is called the Mott Transition [10]. As atoms are compressed, their electron orbitals overlap resulting in the electrons becoming delocalised, and this reduces the electric potential between two charges by the factor e^{-r/r_D} where r is the distance. When this happens an insulator becomes a conductor. Unlike asymptotically free quarks, the Debye screened quarks may undergo significant interactions and thus are characterised by non-perturbative QCD where $\alpha_s \neq 0$. The next section details how the thermodynamic properties of such a state are explored.

1.3.2 Lattice QCD

Where the non-perturbative regime applies, lattice QCD calculations can be employed to predict the thermodynamic properties of hadronic matter. These calculations involve imposing quarks and gluons on a discrete space-time lattice, and then use computational numerical methods to predict temperature and energy density. The results of such a computation are shown in figure 1.4 for various numbers of quark flavour. The steep rise at the critical temperature indicates that quarks and

gluons become the relevant degrees of freedom. This is accompanied by a rise in entropy which is seen for many other thermodynamic phase transitions. At temperatures around the critical temperature, the calculations indicate asymptotic freedom is not achieved for $T \lesssim 4T_C$ as the energy densities lie below the Stefan-Boltzmann values. Although the critical temperature and critical energy density appear largely independent of number of the included quark flavours, beyond this, the absolute values of energy density are not.

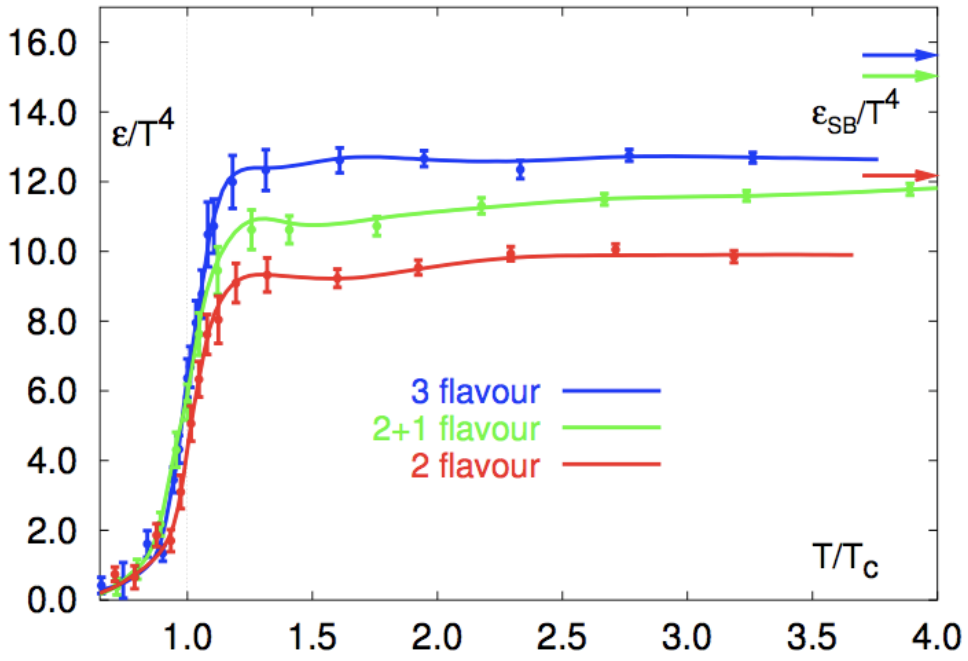

Figure 1.4: The energy density of bulk hadronic matter from lattice QCD calculations [14]. T denotes temperature and T_C the critical temperature for QGP formation. ϵ is the energy density. The red lines show calculations for two degenerate massless quarks flavours, the green lines for two massless quarks and a strange quark, and the blue lines are for three massless quarks. The arrows represent the equivalent Stefan-Boltzmann values.

In addition to a phase transition temperature $T_C = 170 \pm 18$ MeV with a corresponding energy density $\epsilon_C = 700 \pm 350$ MeV [14], further Lattice QCD calculations include: a screened coulomb like potential which acts between a heavy quark

anti-quark pair [15], and an accompanying partial chiral symmetry restoration [16]. Interestingly, partial chiral symmetry restoration is a phase transition in its own right and is connected to the helicity of a fermion. A prediction of QCD is that as a quark becomes deconfined, its mass will drop considerably from the dynamical value of ~ 300 MeV (within a baryon) [17], to a bare value of ~ 5 MeV [1]. The helicity of a fermion is determined by considering the spin and momentum vectors. If they are parallel, the fermion is considered have right handed helicity, if anti-parallel, the fermion is considered to have left handed helicity. If the fermion has zero mass, it is impossible to Lorentz boost to a frame where by the helicity changes. Such a conservation is known as *chiral symmetry* and this will be partially restored for reductions in quark mass.

Recently, there has been interest in the possibility of a critical point which is predicted by various Lattice QCD calculations [18, 19, 20, 21] and is shown in figure 1.3. To the right of the critical point, two distinct phases will exist either side of the solid line, and thus the QGP will hadronise via a first order phase transition. However, due to the extra numerical challenges involved in introducing a non zero baryon chemical potential (which is directly related to net baryon density), lattice QCD calculations have yet to reach a unanimous value. For example, two calculations give a range of $\mu_B = 350 - 750$ MeV [18, 21]. To left of the critical point, the transition is expected to be of the cross-over type with no discontinuities in thermodynamic variables observed [22]. Finally, at the time of writing, including all quark flavours in such calculations is too computationally demanding. However, for the heavy quarks such as charm, bottom and top, thermal production will be sparse for temperatures close to $T_C \sim 200$ MeV as these are significantly less than the respective masses, thus they should have little influence on the equation of state in this temperature region.

1.3.3 Strangeness Enhancement

The possible reduction of the mass of a strange quark in a QGP has led to the belief that strangeness should be enhanced relative to a hadronic gas. This enhancement can be partially understood by examining strangeness production channels for hadronic and partonic interactions. In a hadronic gas, the main channels are as follows:

$$\pi + N \rightarrow \Lambda + K \qquad E_{thres} \sim 540\text{MeV} \tag{1.6}$$

$$\pi + \bar{N} \rightarrow \bar{\Lambda} + \bar{K} \qquad E_{thres} \sim 540\text{MeV} \tag{1.7}$$

$$N + N \rightarrow N + \Lambda + K^{+} \qquad E_{thres} \sim 700\text{MeV} \tag{1.8}$$

$$\pi + \pi \rightarrow K + \bar{K} \qquad E_{thres} \sim 720\text{MeV} \tag{1.9}$$

$$N + N \rightarrow N + N + \Lambda + \bar{\Lambda} \qquad E_{thres} \sim 2200\text{MeV} \tag{1.10}$$

where N represents nucleons, π represents pions, Λ represents the singly strange baryons (lambdas), K represents the singly strange mesons (kaons), and E_{thres} represents the respective energy thresholds. For the deconfined case, the energy threshold is just the sum of the combined mass of a strange quark anti-quark pair which is ~ 200 MeV. The production channels will be $q + \bar{q} \rightarrow s + \bar{s}$ for quarks and $g + g \rightarrow s + \bar{s}$ for gluons. The energy threshold for strangeness is smaller compared to any for the hadronic gas where the lowest $E_{thres} \sim 540$ MeV. Furthermore, interaction cross sections are invariably higher for coloured matter (QGP) compared to colour neutral matter (hadron gas) which may also lead to higher strangeness production rates in the former case. Rafelski and Müller were the first to calculate such production rates in a QGP [23]. They concluded that if the QGP starts off with no strangeness carriers, (anti) strange quark densities would reach equilibrium values (or thermal expectations) in a time ~ 3 fm/c for temperatures around T_C. In a hadron gas, the predicted time scales for kaon (the most abundant strange

hadrons) equilibration are roughly an order of magnitude higher [24]. These facts, coupled with the fact that the energy to produce a $s + \bar{s}$ pair is comparable to the critical temperature, indicate that strangeness will be more readily produced in the QGP.

As will be described in detail in the next chapter, experimentally, *relativistic heavy-ion collisions* are used to try and create the QGP. These collisions deposit hadronic matter in a collision zone with the (experimental) hope that the respective energy density exceeds the critical value for QGP formation. In this case, the gluon channels are expected to dominate the production of strangeness. This is due to the strangeness producing gluonic cross sections being higher than the quarks cross sections [26], and that gluons are likely to be equilibrated on a smaller time scale $\tau_g \sim$ 0.3 fm/c compared to a quark time scale $\tau_q \sim 2$ fm/c [25]. Experimental evidence for strangeness enhancement is shown in figure 1.5. The $\sqrt{s_{NN}}$ term is the centre of mass energy for a colliding nucleon pair. Rapidity, y, will be defined in the next chapter. N_{part} is the mean number of nucleons which participate in the heavy-ion collision and is more commonly labeled $\langle N_{part} \rangle$ and referred to as participants. As heavy-ion collisions have a variety of impact parameters, there will be a variety in numbers of nucleons participating in the collision. Central collisions (small impact parameters) have the largest possible N_{part} values, peripheral collisions (large impact parameters) have the smallest N_{part} values. The term centrality is used to describe such a measure. The enhancement factor, E, is defined as follows:

$$E = \frac{Yield_{AA}/\langle N_{part} \rangle_{AA}}{Yield_{ee}/\langle N_{part} \rangle_{ee}} \tag{1.11}$$

where AA corresponds to the heavy-ions collisions, and ee corresponds to the elementary collisions such as p+p or p+Be. It calculates the deviation in heavy-ion yields per participant from a superposition of elementary collisions. The enhancement factor for charged hadrons is typically $1 \rightarrow 1.4$ for the centre of mass energy

$\sqrt{s_{NN}} = 200$ GeV and a centre of mass energy (19.3 GeV) close to $\sqrt{s_{NN}} = 17.3$ GeV [29]. It is clear that E is well above one for all strange particles, and the magnitude

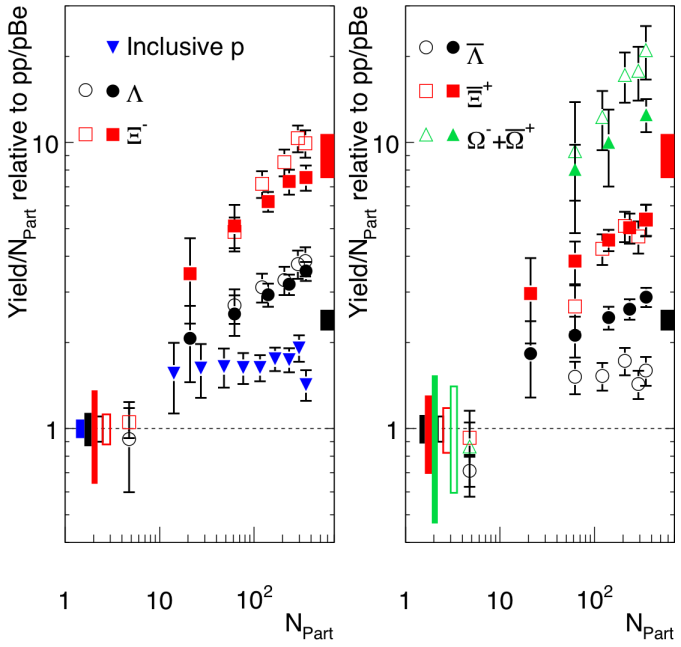

Figure 1.5: Mid-rapidity enhancements as a function of the number of participants for the Λ, $\bar{\Lambda}$, Ξ^-, $\bar{\Xi}^+$, Ω^-, $\bar{\Omega}^+$ particles and inclusive protons. Boxes at unity show statistical and systematical uncertainties combined in the p+p (p+Be) data. Error bars on the data points represent those from the heavy-ions. The solid markers are for Au+Au at $\sqrt{s_{NN}} = 200$ GeV and the open symbols for Pb+Pb ($|y - y_{cm}| < 0.5$) at $\sqrt{s_{NN}} = 17.3$ GeV. Boxes on the right axes mark Canonical predictions at the Grand Canonical limit when varying the temperature from 165 to 170 MeV [27, 28].

of this depends on the (anti) strange quark content i.e. a Λ contains one strange valance quark, a Ξ contains two, and an Ω contains three. The (multi) strange baryon values of E show little dependence on the collisional energy. The Au+Au $\sqrt{s_{NN}} = 200$ GeV $\bar{\Lambda}$ values are roughly a factor of $\sim 1.5 - 2$ higher than the lower collisional energy values. This energy dependence appears negligible for the $\bar{\Xi}^+$ values. The reason for the differing $\bar{\Lambda}$ and $\bar{\Xi}^+$ behaviour is not clear, and it reflects the different production/annihilation mechanisms for the (multi) strange anti-baryons at the different energies. Regarding the proton yields, these are inclusive which means that the measured protons can originate from decays of other particles. As-

suming primordial protons approximately scale with $\langle N_{part} \rangle$, the small enhancement maybe due to the sizable contribution from $\Lambda \rightarrow p^+ + \pi^-$ and $\Sigma^+ \rightarrow p^+ + \pi^0$ which is estimated to be $\sim 40\%$ [30].

Most importantly, the boxes show thermal model predictions for the final state hadron gas temperatures extracted from heavy-ion collisions at both energies. These models will be further described in the next chapter. For Au+Au $\sqrt{s_{NN}} = 200$ GeV collisions, it has been shown that the system lifetime is $4 \rightarrow 10$ fm/c [31]. In the previously mentioned hadronic gas model [24], the time scales for the Λ and Ξ particles to reach thermal equilibrium yield densities were calculated to be $\sim$ 200 fm/c for temperatures similar to the ones shown in figure 1.5. Therefore, the fact that some of the measured values of E are equal or sometimes higher than thermal model predictions, strongly indicates that hadronic interactions are not solely responsible for the production of the strange quarks in the strange baryons. Such a scenario is consistent with QGP formation at both energies assuming the system lifetime is not radically different for heavy-ion collisions with $\sqrt{s_{NN}} = 17.3$ GeV.

1.3.4 High-p_T Suppression

Bjorken first suggested that the QGP state should manifest itself by the suppression of the high momentum partons as they interact with elastically with the medium [33]. It was then proposed that inelastic collisions would also lead to energy loss via gluon radiation [34, 35]. In relativistic heavy-ion collisions, the main source of high momentum particle production is from scattered partons within the initial nucleons which fragment into hadron jets. In order to compare jet production rates in Au+Au (or d+Au) and p+p collisions, R_{AA} is measured which is defined as follows:

$$R_{AA}(p_T) = \frac{\text{Yield}_{\text{ heavy-ion collisions}}/\langle N_{bin} \rangle}{\text{Yield}_{\text{ p+p collisions}}} \tag{1.12}$$

where p_T is the hadron momentum component transverse to the beam, and $\langle N_{bin} \rangle$ is the mean number of binary collisions occurring in a subset of heavy-ion collisions. R_{AA} is also known as a *Nuclear Modification Factor* and is shown in figure 1.6 for charged hadrons in central (small impact parameter, large $\langle N_{part} \rangle$ and $\langle N_{bin} \rangle$) Au+Au and d+Au collisions with $\sqrt{s_{NN}} = 200$ GeV. For heavy-ion collisions, hadrons resulting from high-p_T processes are expected to scale with the number of binary collisions in the *absence* any of medium effects. In this case, $R_{AA} = 1$ which is characteristic of rare probes because the scaling relation results from production in the initial i.e highest energy collisions, and not in any subsequent re-scattering. A stringent test is high-p_T direct photon production which arises from parton-parton hard scatters in the initial nucleon collisions. Due to the fact that photons interact weakly with any form of hadronic matter, R_{AA} is expected to be 1 and the right panel of figure 1.6 shows that above $p_T \gtrsim 2$ GeV/c, this is indeed the case.

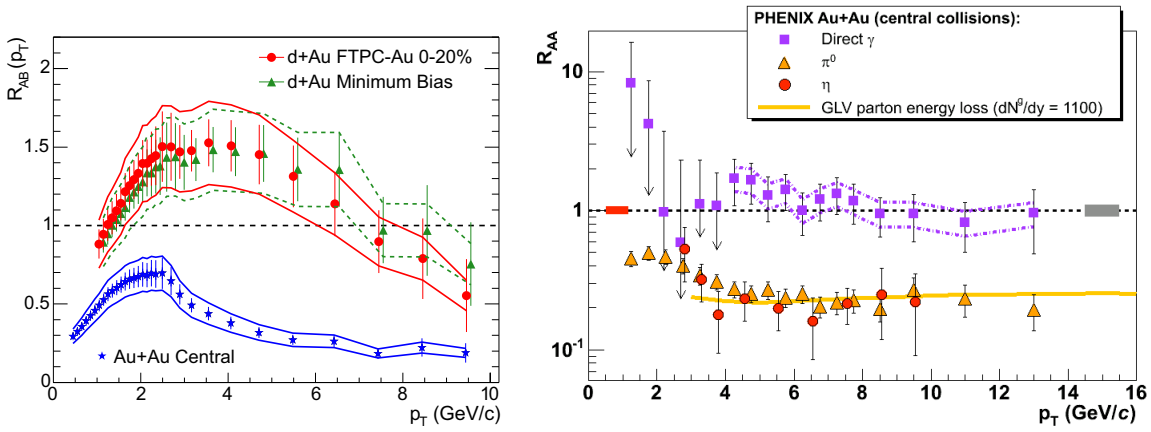

Figure 1.6: Left Panel: R_{AA} (also known as R_{AB}) measured in central Au+Au and d+Au collisions with $\sqrt{s_{NN}} = 200$ GeV for charged hadrons [36]. The percentage refers to the centrality which will be defined in section 2.2.2. Minimum bias means no selection is made on centrality. Right Panel: R_{AA} measured in central Au+Au at $\sqrt{s_{NN}} = 200$ GeV for η, π^0 and direct photons [37]. The grey error band reflects the uncertainty in the number of binary collisions for central Au+Au collisions. The solid yellow curve is a parton energy loss prediction for a medium with a gluon density of 1100 per rapidity unit [38].

However for hadron production in central Au+Au collisions, figure 1.6 shows that

for the charged hadrons and the π^0 and η particles, this is not the case as $R_{AA} \sim 0.2$ for $p_T > 4$ GeV/c. This phenomenon is known as *jet quenching*. Moreover, for d+Au collisions where the QGP is not expected to form, an *enhancement* is observed across most of the p_T range for both centralities. The enhancement is commonly attributed to the Cronin effect [39] which is the result of the initial longitudinal momentum being transfered to transverse momentum via multiple scattering, and is also expected to occur A+A for collisions. Of course, $R_{AA} < 1$ for central Au+Au is consistent with high-p_T suppression which appears to completely overwhelm the Cronin effect. On figure 1.6, a pQCD calculation which determines the hadron suppression production rates via QGP modified jet cross sections reproduces the observation very well.

1.4 Outline

This analysis concerns measurements of Λ, $\bar{\Lambda}$, K^0_S yields from ^{63}Cu+^{63}Cu $\sqrt{s_{NN}} =$ 200 GeV collisions at the Relativistic Heavy-Ion Collider (RHIC). A large amount of data (80 million collisions) was acquired by the STAR experiment in early 2005, which enables a detailed study of the smaller system size. Firstly, measurements from Cu+Cu collisions will help with more precise mapping of the $N_{part} < 126$ region. The Au+Au $\sqrt{s_{NN}} = 200$ GeV measurements in figure 1.5 only contain a single data point in this region despite the rapid rise in per participant yields from p+p to mid-central Au+Au ($\langle N_{part} \rangle \sim 200$) collisions. On the other hand, at lower centre of mass energies per nucleon, both the K/π ratio and strangeness yields per participant have shown higher values in the lighter systems compared to heavier systems with similar numbers of participants. The K/π ratio contrasts bulk strangeness production to bulk non-strangeness production; kaons and pion represent the most most abundant strange and non-strange particles produced respectively.

As shown in figure 1.7, for Si+Al and Si+Au $\sqrt{s_{NN}} \sim 5$ GeV collisions the

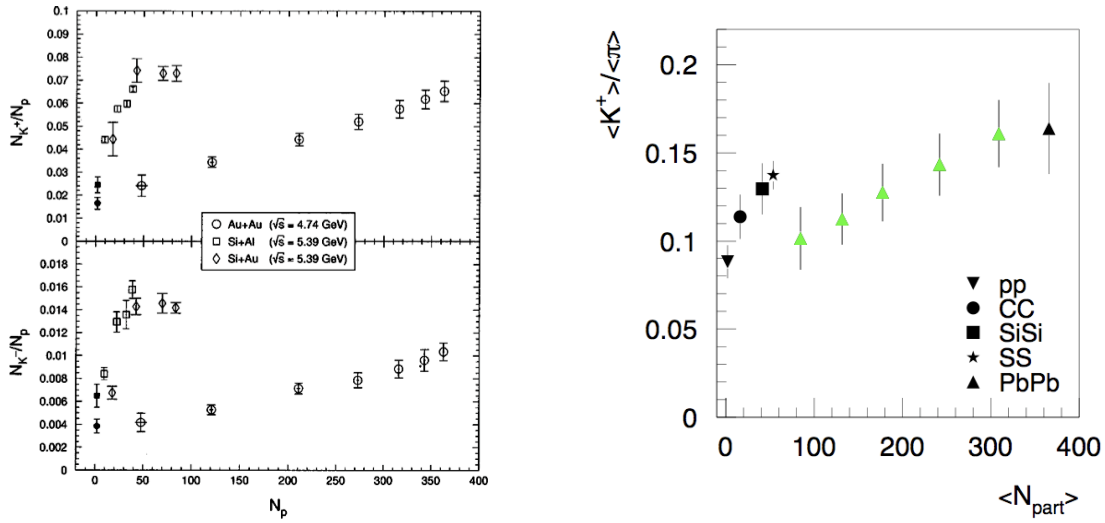

Figure 1.7: Strangeness production in light and heavy systems. Left Panel: Charged kaon yields per $\langle N_{part} \rangle$ as a function of $\langle N_{part} \rangle$ [41]. Right Panel: K/π ratio as a function $\langle N_{part} \rangle$ for $\sqrt{s_{NN}} = 17.3$ GeV collisions [42].

$\langle K^+ \rangle / \langle N_{part} \rangle$ and $\langle K^- \rangle / \langle N_{part} \rangle$ ratios were factors of 2-3 higher compared to Au+Au collisions with similar centre of mass energies per nucleon and similar values of $\langle N_{part} \rangle$[41]. For $\sqrt{s_{NN}} = 17.3$ GeV collisions, higher $\langle K^+ \rangle / \langle \pi^+ \rangle$, $\langle K^- \rangle / \langle \pi^+ \rangle$ and $\langle \phi \rangle / \langle \pi^+ \rangle$ ratios were reported for Si+Si and C+C collisions compared to peripheral and mid-central Pb+Pb collisions [42]. Both measurements show collision geometry (as well as size) may play an important role for strangeness production. One would expect that the reaction region would have a different shape for light systems with similar $\langle N_{part} \rangle$ to heavier systems. For example, a very central Si+Si collision ($\langle N_{part} \rangle \sim 54$) will have a spherical overlap region compared to a Pb+Pb collision of similar $\langle N_{part} \rangle$ which would be elliptical in shape. In light of this, and the other observations mentioned, the following questions can be addressed:

- Are strangeness yields per $\langle N_{part} \rangle$ at RHIC really controlled by system size?
- Will high-p_T Λ, $\bar{\Lambda}$, K^0_S production be suppressed in Cu+Cu collisions despite the smaller system sizes compared to Au+Au?

Chapter 2 will describe the key experimental programs and the relevant exper-

iment variables for relativistic heavy-ion collisions. Along with others, the previously mentioned experimental measurements of strange particles yields will also be reviewed further with possible interpretations discussed. Chapter 3 will describe the STAR experiment at the Relativistic Heavy Ion Collider at Brookhaven National Laboratory on Long Island, USA. Chapter 4 will describe vertex finding and centrality determination for the STAR experiment, and chapter 5 will then describe the techniques for strange particle yield extraction. Chapter 6 will then discuss the results with the conclusions being made in chapter 7.

Chapter 2

RELATIVISTIC HEAVY-ION COLLISIONS

Collisions of heavy-ions travelling at relativistic velocities are used to try and create the *Quark Gluon Plasma* (QGP) in the laboratory. Put simply, as the heavy-ions collide they interact inelastically and lose kinetic energy. This loss of kinetic energy leads to the creation of matter in the vicinity of the collision which is often labelled the *fireball*, and if this is hot enough, the QGP will be formed. As shown in figure 2.1, in the conventional picture the fireball will then expand due to pressure gradients relative to the vacuum. As it expands and cools, quarks and gluons will then form a hadron gas when the critical temperature T_C is reached. As the hadron gas expands, inelastic collisions will eventually cease at the *chemical freeze-out*, temperature T_{ch}. The chemical make-up from this point onwards will remain the same. After further expansion, elastic collisions will cease and this is known as *thermal freeze-out*, with a corresponding temperature T_{fo}.

This chapter will give a brief overview of past, present and future experimental programs, and will then describe the key experimental observables for relativistic heavy-ion collisions. The chapter will then finish with more on experimental strange particle yield measurements, and their possible relation to deconfinement.

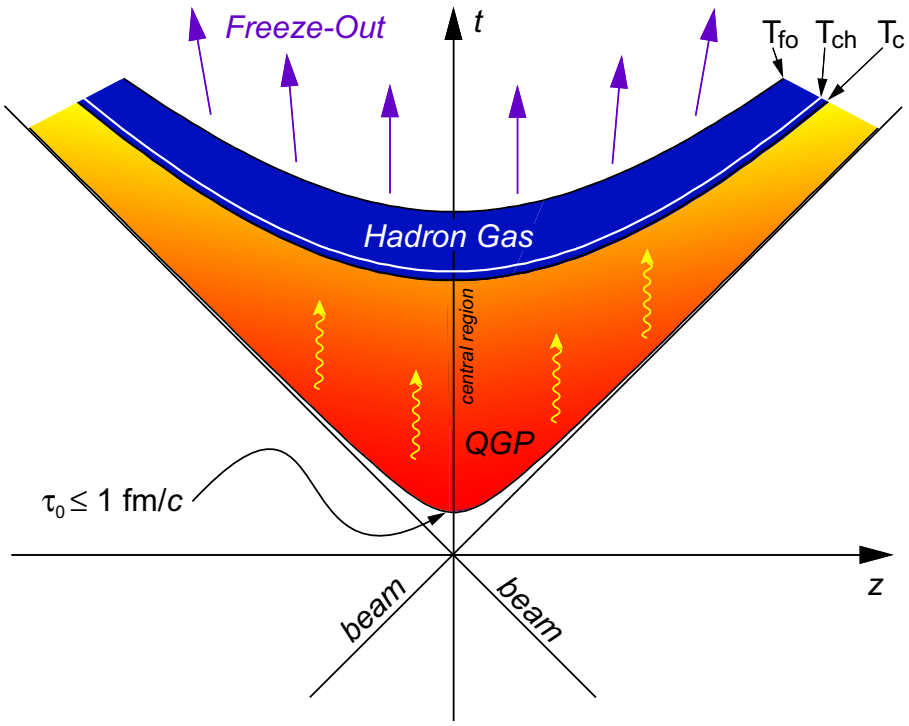

Figure 2.1: The space-time evolution of a heavy-ion collision [43]. τ_0 is the particle formation time, T_C is the critical temperature, T_{ch} is the chemical freeze-out temperature, and T_{fo} is the thermal freeze-out temperature.

2.1 Experimental Programs

To date, there have been three dedicated experimental programs in search of the QGP using relativistic heavy-ion collisions. The Alternating Gradient Synchrotron (AGS) at Brookhaven National Laboratory, USA, collided Si+Al, Si+Au and Au+Au nuclei in the centre of mass energy per nucleon range $\sqrt{s_{NN}}$ ~ 2-5 GeV. The Super Proton Synchrotron (SPS) at CERN, Switzerland, collided various ions such as p+Be, O+O, S+S and Pb+Pb in range $\sqrt{s_{NN}}$ ~ 8-17 GeV. Both facilities which started operations in the mid 1980s, ran in a fixed target mode which involved colliding beams with stationary targets. The Relativistic Heavy Ion Collider (RHIC), which began operations in 1999, is also able collide a variety of species such as p+p, d+Au, Cu+Cu, and Au+Au nuclei with centre of mass energies $\sqrt{s_{NN}}$ ~10-200

GeV. The Large Hadron Collider (LHC), which will be able to collide p+p and Pb+Pb nuclei with $\sqrt{s_{NN}} = 5.5$ TeV, is expected to be begin operations in 2008 with the heavy-ion program starting in 2009-2010. As opposed to the AGS and SPS programs, both RHIC and LHC accelerate ions in concentric rings which are brought together at a number of interaction points. This approach enables higher centre of mass energies to be achieved.

2.2 Experimental Observables

There is a range of information one needs to extract from the products of a heavy-ion collision in order to ascertain the properties of the fireball. As outlined in the previous chapter, the temperature and energy density of the fireball, and the net baryon density are very important parameters in determining whether the QGP is formed. In addition, for a variety of reasons, knowledge of the amount of matter participating in a collision (centrality) is also of vital importance.

2.2.1 Rapidity and Transverse Momentum

The two important experimental phase space observables of the particles emerging from a heavy-ion collision are rapidity and transverse momentum. Rapidity is given by the following equation:

$$y = \frac{1}{2}\ln\left(\frac{E + p_L}{E - p_L}\right) \tag{2.1}$$

where p_L is the longitudinal momentum component along the beam direction, and E is the total energy of the particle. It is a logarithmic measure of the longitudinal momentum and has the property of being Lorentz additive when switching between reference frames. This is useful when comparing rapidity distributions of particles from fixed target to collider experiments; the rapidity measured in the fixed target frame will be equivalent to the rapidity measured in the centre of momentum frame

plus some constant. In the centre of momentum frame which coincides with the laboratory frame for collider experiments, mid-rapidity corresponds to $y \sim 0$. Beam rapidity is calculated from the longitudinal momentum of the nuclei prior to the collision. If the particle mass is not known, a quantity known as pseudorapidity can be used and is defined as follows:

$$\eta = -\ln\left(\tan\frac{\theta}{2}\right) \tag{2.2}$$

where the angle θ is calculated from the particle direction relative to the beam axis. When a particle's momentum magnitude tends to the total energy ($p \to E$), pseudorapidity tends to rapidity ($\eta \to y$). The transverse momentum, p_T, is another very useful quantity, and is defined as the momentum component transverse to the beam axis. It is extensively measured in all heavy-ion experiments because it has the advantage of being Lorentz invariant upon transformations in the beam direction, and is thus directly comparable between the two types of experiment. Moreover, it will be generated as a result of the collision, and thus offers an insight into the collision dynamics.

2.2.2 Collision Centrality

Figure 2.2 illustrates a heavy-ion collision. As mentioned in the introduction, central collisions are defined as having a small impact parameter thus a large amount of participating matter, peripheral collisions are defined as having a large impact parameter with a small amount of participating matter. As the impact parameter cannot be directly determined experimentally, the produced charged particle multiplicity is often used to characterise centrality. The intuitive assumption here is that particle production increases monotonically with an increasing number of participating nucleons, thus the event-wise particle multiplicity (usually within a fixed

acceptance) can then be used to define centrality. Figure 2.3 shows the multiplic-

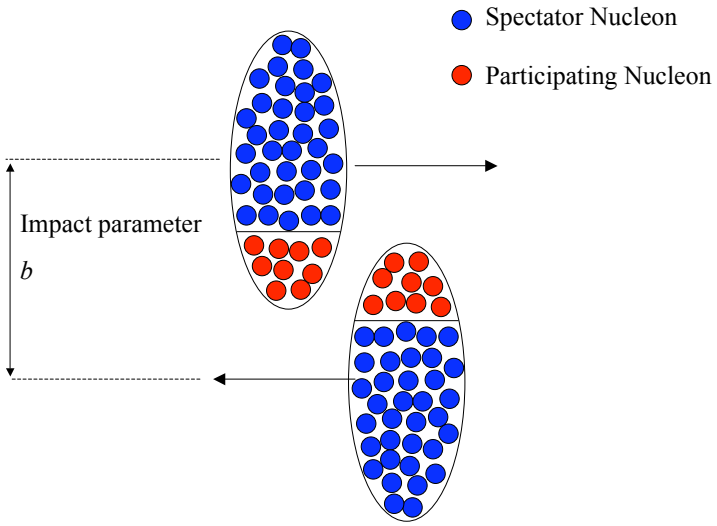

Figure 2.2: A heavy-ion collision showing the impact parameter, and spectating/participating nucleons.

ity distribution for Cu+Cu $\sqrt{s_{NN}}$ = 200 GeV collisions applicable to this analysis. The centrality classes are determined by binning the distribution into fractions with respect to the total integral. For example, in figure 2.3, the area within the 0-10 % range corresponds to a tenth of the total integral. A Cu+Cu event with a reference multiplicity of 200 will be deemed a central event, as it lies in the 0-10% range. Conversely, an event with a reference multiplicity of 26, will be deemed peripheral as it lies in the 40-60% range. Algebraically, the centrality fraction is defined as follows:

$$C_f = \frac{1}{N_{events}} \int_{M_0}^{\infty} \frac{dN}{dM} dM \tag{2.3}$$

where C_f is the centrality fraction for events with multiplicity M_0 and above. The term in the integral represents the multiplicity distribution (number of events per multiplicity unit), and N_{events} is total number of events from which the multiplicity distribution is derived. In figure 2.3, when $M_0 = 139$, the corresponding centrality

fraction is 0.1; $M_0 = 98$ corresponds to 0.2, etc.

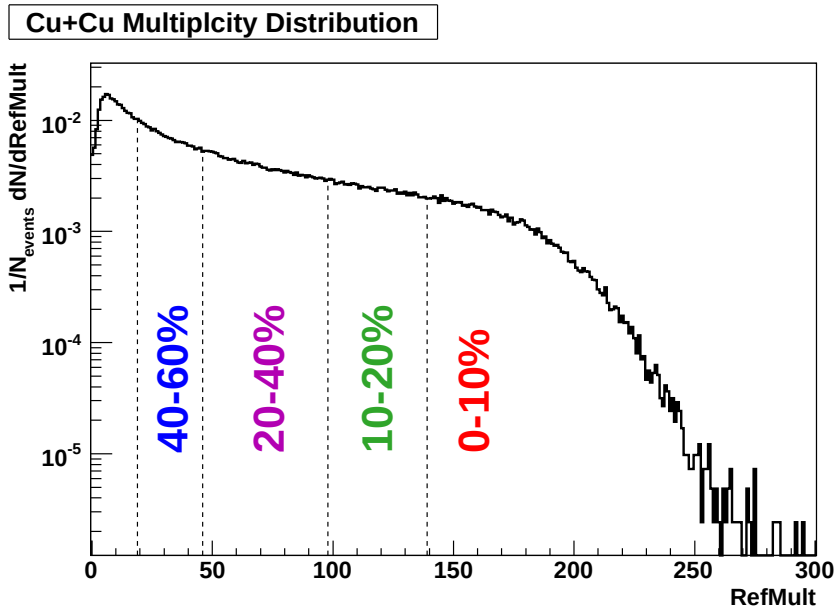

Figure 2.3: The Cu+Cu $\sqrt{s_{NN}} = 200$ GeV reference multiplicity (RefMult) distribution with centrality definitions. For a given event, RefMult is the number of charged particles originating from collision vertex with $|\eta| < 0.5$.

For a given amount, or range of particles produced, Glauber theory can then be used to infer the mean impact parameter, along with the mean number of participating nucleons, $\langle N_{part} \rangle$, and the mean number of binary collisions, $\langle N_{bin} \rangle$. For the limiting case $N_{part} = 2$, N_{bin} is defined as 1. It is possible that a participating nucleon will undergo more than one collision, thus the ratio of binary collisions to participant pairs, ν, is nearly always greater than 1 in heavy-ion collisons. Within the Glauber framework, heavy-ion collisions are described under these principal assumptions [44]:

- A nucleus-nucleus collision is treated as the superposition of many nucleon-nucleon collisions.

- The nucleons travel in straight line trajectroies.

The distribution of the nucleons in coordinate space is usually determined by the Woods-Saxon formula. For a given impact parameter, a nucleon-nucleon collision is registered if they overlap in space and time during the collision. The nucleon size is represented by the measured p+p inelastic cross-section, σ_{inel}, for the particular energy range studied. The exact implementation of this procedure comes in two varieties, Optical Glauber and Monte Carlo Glauber. The former uses an analytic approach to calculate $\langle N_{part} \rangle$, $\langle N_{bin} \rangle$ from the Woods-Saxon distribution, while the latter simulates nucleons randomly according to the Woods-Saxon distribution. Monte Carlo Glauber receives more widespread use, as Optical Glauber calculations lead to N_{part} and N_{bin} tending to 0 for the collisions with large impact parameters whereas the physical limit is 2 and 1 receptively [45]. For Cu+Cu $\sqrt{s_{NN}} = 200$ GeV collisions, centrality determination and calculation of $\langle N_{part} \rangle$ and $\langle N_{bin} \rangle$ for a given centrality bin was part of this work, and will be described in section 4.4.

2.2.3 Energy Density

The initial energy density in heavy-ion collisions also cannot be measured directly, and thus has to be inferred from the final state products. The most popular model for determining the initial energy density in heavy-ion collisions at RHIC is the Bjorken Model [46]. This assumes that the particles created at mid-rapidity result from inelastic processes and after some formation time, τ_0, they can undergo rescattering. The particles are refereed to as quanta and the model does not distinguish between whether these particles are hadrons or partons. Figure 2.4 helps illustrate how the energy density is derived. The formed particles radiating from the thin disk in the yellow region will have a maximum velocity of $\beta = d/\tau_0$, thus the number of particles in this region will have velocities from 0 to β at τ_0. For small values of β, the number of particles is $\beta dN/d\beta$ within volume $\beta\tau_0 A$ where A is the overlap area. This gives

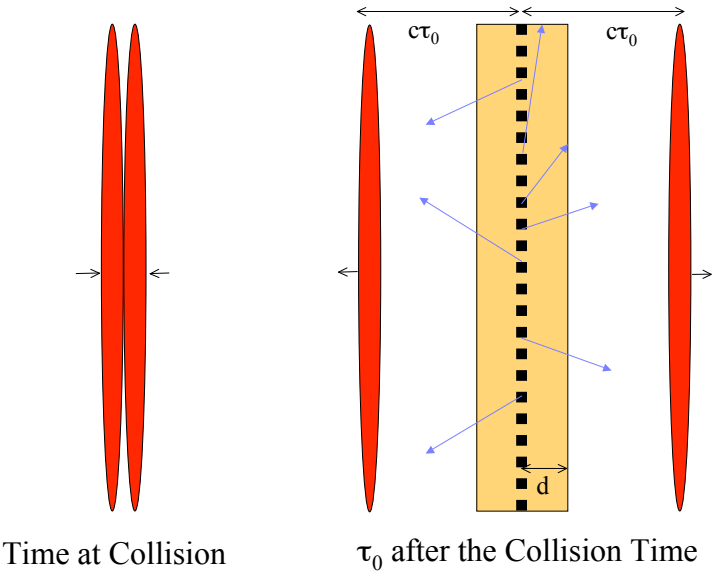

Figure 2.4: Illustration of Bjorken energy density calculation. The red discs indicate the highly relativistic colliding ions and blue arrows indicate quanta radiating from the collision region represented by the dashed line. τ_0 is quanta formation time and d is the distance at which a particle with an arbitrary velocity is formed.

an energy density of:

$$\epsilon_{Bj} = \frac{dE_T}{dy}\frac{1}{\tau_0 \mathrm{A}} \tag{2.4}$$

as $dE_T = \langle m_T \rangle dN$, $\langle m_T \rangle$ is the mean transverse mass with $\langle m_T \rangle = \sqrt{\langle p_T \rangle^2 + m_0^2}$ where m_0 is the particle rest mass, and $dy = d\beta$. dE_T/dy is thus total transverse energy carried by the particles emerging per unit of rapidity at $y \sim 0$. The Bjorken model is valid as long as the particles are formed in volume much bigger the collision volume i.e. the length $\tau_0 c >> 2R/\gamma$ where R is heavy-ion radius and γ is the Lorentz contraction factor. Otherwise, particles with the same β can form in different regions which invalidates the thin disk assumption thus the use of dA as the active volume. The Bjorken energy density has been estimated for central Au+Au collisions with $\sqrt{s_{NN}} = 200$ GeV using the measured $dE_T/dy \simeq 620$ GeV, and an overlap area $A \simeq 130$ fm^2 [47]. The estimation proceeds as follows [48].

Although τ_0 is not directly observable, it was calculated to be $\tau_0 \simeq 0.35$ fm/c using the uncertainty principle ($\tau_0 \simeq 0.2/\langle m_T \rangle$ in $\hbar$ units of GeV fm/c) and the hadron $\langle m_T \rangle \simeq 0.57$ GeV which is applicable over a wide range of collision energies. With these values, the Bjorken energy density $\epsilon_{Bj} \simeq 14$ GeV fm^{-3}. This is significantly higher than the critical energy density, $\epsilon_C \sim 0.7$ GeV fm^{-3} quoted in section 1.3.2, further suggesting deconfinement is achieved at RHIC energies. Finally, although relating the mean final state hadron energy to the mean initial state parton energy appears questionable, the argument is often made on grounds of entropy conservation, i.e. the local number density of particles can never decrease during the fireball evolution [49].

2.2.4 Particle Spectra and Temperature

Particle momentum distributions (spectra) are usually studied by calculating the invariant cross section given by:

$$E\frac{d^3N}{dp^3} = \frac{1}{2\pi p_T}\frac{d^2N}{dp_T dy} \tag{2.5}$$

where E is the particle energy. $d^2N/dp_T dy$ repesents a event-wise yield density and in practice is approximated by $N/\delta p_T \delta y$ with N being the number of particles per event in a p_T interval of width δp_T and y interval of width δy. Figure 2.5 shows spectra measurements for strange particles at RHIC [51]. Hagedorn postulated that the temperature T of a static source can be extracted using Boltzman statistics which assumes $d^3N/dp^3 \propto e^{-E/T}$ [50]. The resulting momentum distribution at mid-rapidity is known as a m_T exponential given by:

$$\frac{1}{2\pi p_T}\frac{d^2N}{dp_T dy} = Ae^{-m_T/T} \tag{2.6}$$

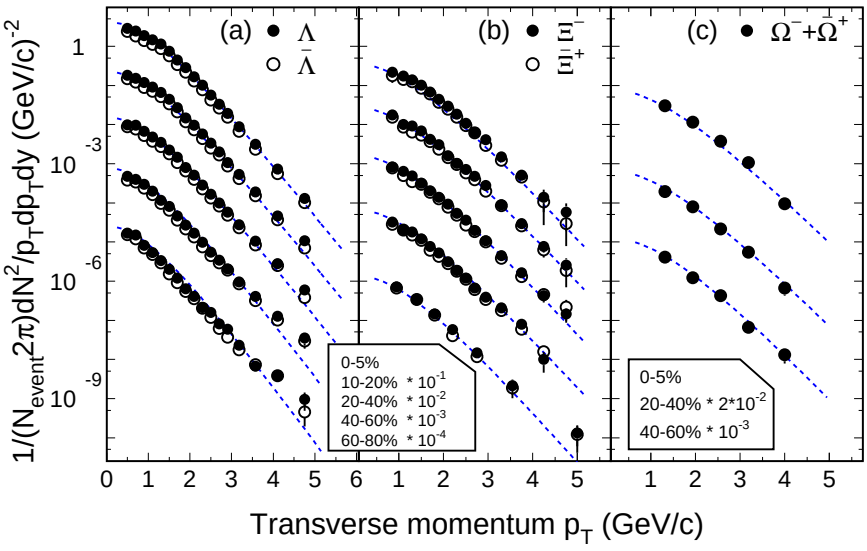

Figure 2.5: Mid-rapidity p_T spectra of Λ, $\bar{\Lambda}$, Ξ, $\bar{\Xi}$, Ω and $\bar{\Omega}$ particles for various centralities in Au+Au $\sqrt{s_{NN}} = 200$ GeV collisions [51]. $1/N_{events} d^2N/dp_T dy$ in this figure is equivalent to $d^2N/dp_T dy$ in the text.

where m_T is the transverse mass. Interestingly, it has also been shown with QCD string phenomenology, m_T exponential like distributions are expected when particles are produced via string breaking for strong fields which fluctuate [52]. In this case, T is proportional to the square root of the string constant k. For the case of a static thermalised fireball, in principle extracting T for various particles should give a common thermal freeze-out temperature T_{fo}. However, if the fireball has developed collective flow prior to thermal decoupling, this leads to a particle mass dependance of T which can be given by:

$$T = T_{fo} + m_0 \langle \beta_T \rangle^2 \tag{2.7}$$

where β_T is the mean transverse flow velocity and m_0 is particle mass. Such collective behaviour can be generated from pressure gradients in the fireball which blue shifts the measured temperature T. Because of this T, is simply known as the inverse

slope parameter. At SPS energies, such a mass dependance was observed for central Pb+Pb $\sqrt{s_{NN}}$ = 17.3 GeV collisions with the extracted $\beta_T = 0.39 \pm 0.18c$ [53]. Both β_T and T_{fo} can also be extracted using the more sophisticated *blast wave fits* [54, 55]. This model was also applied to the previously mentioned SPS data and was found to give similar flow velocities.

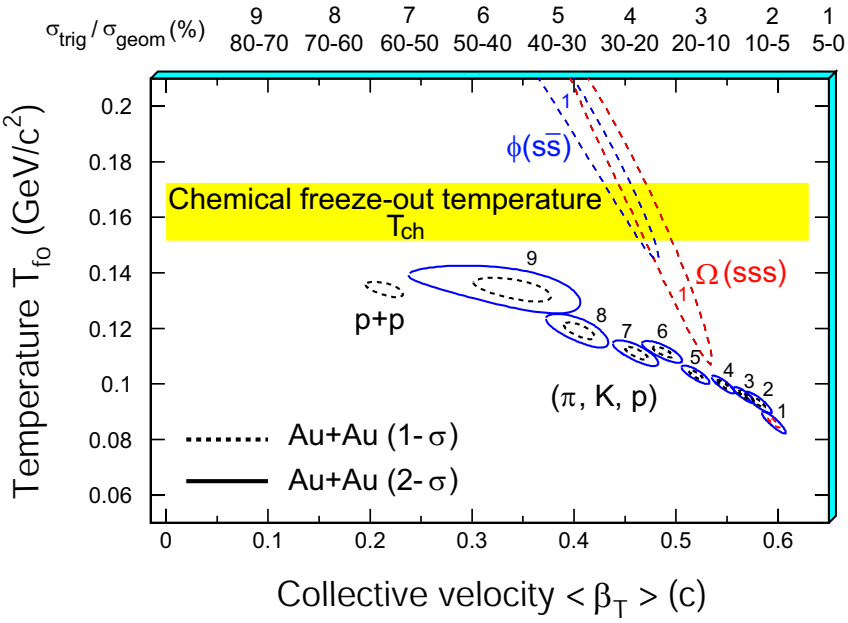

Figure 2.6: Results from blast wave fits on mid-rapidity measured particle spectra for Au+Au $\sqrt{s_{NN}}$ = 200 GeV collisions with various centralities [56, 57]. The y-axis represents the thermal freeze out temperature, and x-axis represents the transverse flow velocity. The contours indicate statistical confidence levels assuming Gaussian uncertainties. $\sigma_{trig}/\sigma_{geom}$ is an alternative term for centrality fractions.

Figure 2.6 shows the results of blast wave calculations for Au+Au collisions with $\sqrt{s_{NN}}$ = 200 GeV. It is clear that as system size increases, larger flow velocities are observed. Such a dependance is often interpreted as more rescattering occurring in larger systems which in turns allows larger collective flow velocities to develop. This is also supported by the drop in the thermal freeze-out temperature with system size which suggests that larger systems are in thermal contact for a longer time period. Interestingly, the Ω and ϕ particles have the highest kinetic freeze-out temperatures, which suggests they thermally decouple from the expanding fireball earliest. How-

ever, for the p+p data in figure 2.6, care should be exercised when interpreting the blast-wave parameters as these collisions are not expected to produce a thermalised medium under collective flow.

As the fireball chemistry by definition does not change after chemical freeze-out, particle abundances can be used to calculate the chemical freeze-out temperature T_{ch} again using Boltzman statistics for a Grand Canonical ensemble. This is known as the *Hadron Gas Model*. Integrating over all momenta, the average particle density per unit volume for a given mass m_i and degeneracy g_i can be given by [58]:

$$n_i = g_i \int \frac{d^3p}{(2\pi)^3} e^{-(E_i-\mu_i)/T_{ch}} \tag{2.8}$$

$$= g_i \frac{m_i^2 T_{ch}}{(2\pi)^2} K_2(m_i/T_{ch}) e^{\mu_i/T_{ch}} \tag{2.9}$$

where μ_i is the chemical potential and K_2 is the modified Bessel function. The chemical potential is used to conserve quantum number from the initial to final state conditions, and can be constructed as $\mu_i = b\mu_b + s\mu_s + c\mu_c$ where b, s, c, denote baryon number, strangeness and isospin for the particle in question, and μ_b, μ_s, μ_c denote the respective potentials. In heavy-ion collisions, as it is possible for net baryon number and net isospin (assuming the ions have more neutrons than protons) to be transfered into the fireball, and as net strangeness must be zero, the extracted values of μ_b, μ_s, μ_c must therefore allow for net baryon/isospin and no net strangeness for yields in the full rapidity range.

Both T_{ch} and μ_b have been extracted for heavy-ion collisions by comparing measured particle ratios. Specific hadronic abundances not often used as the volume is unknown. When ratios are used, this volume cancels as evident in equation 2.9, and reduces the numbers of fit parameters for the extraction. Measurements at the STAR experiment have shown that for Au+Au $\sqrt{s_{NN}}$ = 200 GeV collisions, the chemical freeze-out temperature $T_{ch} = 163 \pm 4$ MeV (also shown in figure 2.6), and

$\mu_b = 24 \pm 4$ MeV [54, 55, 59]. This indicates that some baryon number is indeed transfered to the fireball and on a more elementary level, baryon transportation is also shown by the fact that the measured anti-baryon/baryon ratios are below one. The extracted chemical freeze-out temperature is very close to predicted critical temperature for deconfinement , $T_c = 170$ MeV quoted in section 1.3.2.

Similar models have been used to extract a chemical freeze-out temperature for the elementary p+p and $e^+ + e^-$ collisions with high levels of statistical confidence [60, 61]. Although these systems are not thermal sources, it has been shown that for any process with a finite energy available for particle production, a statistical filling of phase space gives a predicted mass dependance similar to one shown in equation 2.9 [62]. This arises from the fact that there are many more final state configurations with lower mass particles compared to configurations with higher mass particles, with the "effective temperature" controlling the relative weights. More importantly, it points to the fact that although a thermal fit to heavy-ion data may well be successful in terms of probability measures such a $\chi^2/DOF \sim 1$, it cannot to be used to fully justify the fireball has reached thermal equilibrium. This has be qualified with other measures.

2.3 Strange Particle Yields

To consolidate on information given in the introduction, the remainder of this chapter will focus on strange particle yields and their role as a signature of deconfinement at RHIC. There are of course many other experimental signatures which support deconfinement, and indeed that this was reached at lower energies. Examples are the suppression of charmonium production in central Pb+Pb and Au+Au collisions (which is a consequence of Debye screening) [63, 64], the enhancement in low mass di-lepton production [65, 66, 67], and the observed azimuthal flow for hadrons [69, 70, 71]. Azimuthal flow measurements have received widespread interest [68], as

they seem to confirm that theramalisation is achieved in the early stages of the collision. This conclusion is reached when hydrodynamic models are used to reproduce the measured azimuthal flow values: only if a thermalised partonic state occurs at $\tau \sim 0.6$ fm/c after the initial collision (with Lattice QCD describing the equation of state after this time), can the predicted hydrodynamic azimuthal flow values match the measured values. Assuming an initially hadronic state leads to azimuthal flow values being under predicted when the hydrodynamic description is applied [72].

2.3.1 Bulk Strangeness Production

In addressing strangeness production, the most common measures are either comparisons of strange particle yields to non-strange particles yields, or strange particle yields per number of participating nucleons, $\langle N_{part} \rangle$. As kaons are the lightest strange particles and carry most of the strangeness created, and as pions are the most abundant non-strange particles produced, by forming the K/π ratio, the bulk strange matter is compared to the bulk non-strange matter. Figure 2.7 shows the K/π ratios as a function of energy for heavy-ion collisions which indicates a number of trends. Firstly, and perphaps most importantly, nearly all K^+/π^+ ratios in central heavy-ion collisions lie systematically higher than for the elementary collisions; at the RHIC energy of $\sqrt{s_{NN}} = 200$ GeV, the increase has been shown be $\sim 50\%$ by a later measurement [73]. This of course shows that strangeness is more readily produced in central heavy-ion collisions compared to p+p collisions at a given energy. Given that one does not expect a QGP to form in a p+p collision, strangeness enhancement has apparently been confirmed. However, there are other explanations for a higher K/π ratio in central heavy-ion collisions which currently renders such a measurement ambiguous in relation to QGP formation.

The first relates to QCD string formation. In the Lund string fragmentation scheme [9], relative to the light quarks, strange quark formation is suppressed by

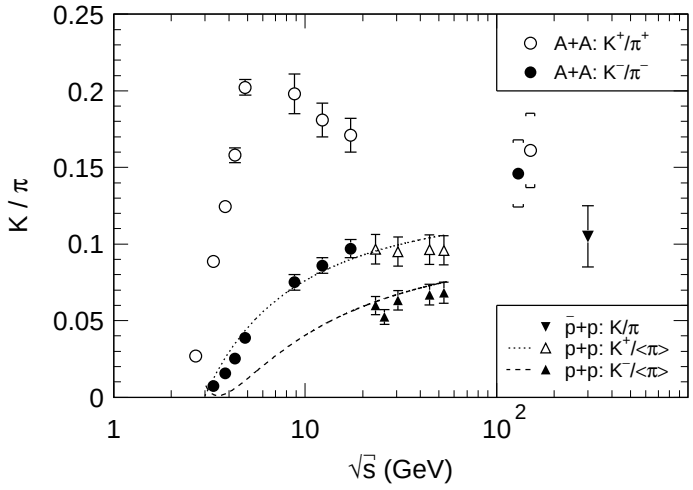

Figure 2.7: Energy dependence of K/π ratios in central Pb+Pb (Au+Au) collisions and the elementary proton-proton collisions [40]. $\langle\pi\rangle$ represents the average chagred pion yield i.e. $(\pi^+ + \pi^-)/2$. The curves are parameterisations of p+p data.

the factor $e^{-(m_s^2 - m_u^2)/k}$ where m represents the quark mass and k is the string constant shown in equation 1.1. It has been conjectured that relative to p+p collisions, the string constant in heavy-ion collisions increases as nucleon-pair strings merge with others to form *colour ropes* [74]. From the suppression factor, it is clear that colour rope formation would lead to higher K/π ratios in heavy-ion collisions. Such a process is implemented in the computational Relativistic Quantum Molecular Dynamics (RQMD) model which describes hadron production through the dynamics of string formation and fragmentation in parton-parton interactions, and allows the formed hadrons to interact inelastically [75]. It known as a *dynamical model* as all the interacting components (strings/partons/hadrons) are traced in space and time and thus differs from thermal models which describe particle production with just a few parameters. e.g. temperature and chemical potential. Heavy-ion collisions are treated as a superposition of p+p collisions with the afore mentioned colour rope formation more likely to occur in the former. Despite deconfinement not being treated in the conventional sense, the RQMD model has been shown to describe the energy dependance of both the heavy-ion and p+p K/π ratios quite well [76].

Using beam energy dependent parameterisations of μ_b and T_{ch}, an extension of Hadron Gas Model also describes the energy dependence of the K/π ratio in heavy-ion collisions quite well [77]. This extension is known as the *Canonical formalism*. In the standard Grand Canonical Hadron Gas Model shown by equation 2.9, for a large ensemble of events, i.e. heavy-ion collisions, the chemical potentials are determined so that the following condition applies [79]:

$$\langle N_s \rangle - \langle N_{\bar{s}} \rangle = 0 \tag{2.10}$$

where N represents the number of strangeness carriers. However, conservation of net strangeness is not strictly met on an event-by-event basis so the standard Hadron Gas Model allows for events where $N_s - N_{\bar{s}} \neq 0$. In the Canonical formalism, conservation laws are implemented locally on an event-by-event basis, and thus only allows for events with zero net strangeness [80]. Relative to Grand Canonical predictions, this reduces the phase space allowed for strangeness carriers and ensures the following event-wise condition is always met:

$$N_s - N_{\bar{s}} = 0 \tag{2.11}$$

For large numbers of predicted strangeness carriers, the Canonical predictions match those of the Grand Canonical formalism which demonstrates that the contribution of events with net strangeness becomes small in large systems. This equivalence is known as the *Grand Canonical* limit. The ratio of Canonical and Grand Canonical yield densities is known as the *Canonical suppression factor* which is one in the Grand Canonical limit. Regarding K/π ratio predictions, the Canonical approach is thus particularly well suited for the AGS energies where the event-wise kaon yields were of the order of a few. As a final note, because the Canonical formalism (as with all thermal models) does not demand deconfinement to have occurred prior to

T_{ch}, its success in describing strangeness yields gives little information on whether deconfinement actually has occurred. One the other hand, if deconfinement leads to strangeness yields reaching thermal expectations prior to hadronisation via the drop in the strange quark mass (in line with original predictions [23]), the success of thermal models in describing final state strangeness yields comes as no surprise if thermal equilibrium is maintained until chemical freeze-out. This is especially true given the equilibrium time scales discussed in section 1.3.3.

In the Canonical Formalism, the higher K/π ratios in central heavy-ion collisions are linked to a volume dependance of strangeness yields per unit volume. As seen in equation 2.9, this is absent for Grand Canonical predictions. The left panel of figure 2.8 contrasts Canonical predictions to kaon yields from two dynamical models which allow for kaon production/annihilation in a pion gas. These models also treat conservation laws strictly ensuring that quantum numbers are conserved in all sub processes. The equivalence between the thermal and dynamical models is clear, and this illustrates the predictive power of thermal models which unlike dynamical models, require just a few macroscopic variables to calculate yield densities. In the dynamical models, an observed increase in kaon annihilation processes lead to the kaon densities decreasing with system size. The right panel of figure 2.8 shows Canonical predictions for (multi) strange baryons from Au+Au $\sqrt{s_{NN}} = 130$ GeV collisions. In this case, yield densities are calculated with the volume $V = V_0\langle N_{part}\rangle/2$ where V_0 is 7 fm^3, the volume of a nucleon. This cancels when the enhancement factor E is formed. Grand Canonical limit predictions for Au+Au $\sqrt{s_{NN}} = 200$ GeV collisions are also shown figure 1.5 by the red and black lines. The main inputs are T_{ch} and u_b which may change with beam energy and these determine the predicted enhancement factor values. E is particularly sensitive to T_{ch}. However, irrespective of the determined values of T_{ch} and u_b values spanning AGS, SPS and RHIC energies, the enhancement factor ordering with respect to the

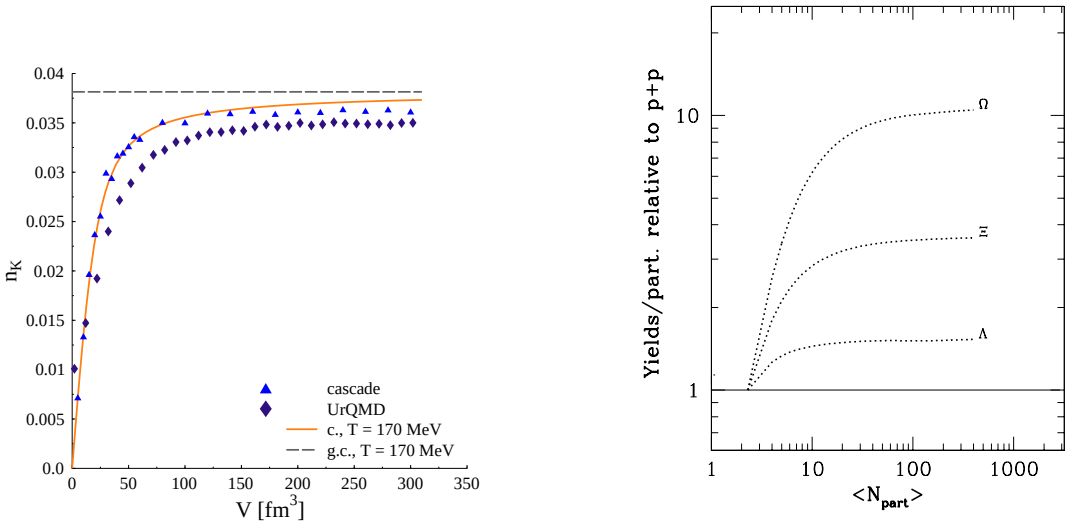

Figure 2.8: The volume dependence of the average number of kaons per unit volume computed from the URQMD and cascade dynamical models, and for the Canonical formalism (yellow lines)[78]. The dashed lines represent the Grand Canonical limit. Right Panel. Canonical enhancement factor (E) predictions for (multi) strange baryons when $T_{ch} = 175$ MeV and $u_b = 51$ MeV [80].

strange quark content observed in figure 1.5 is always maintained [80, 129]. The Canonical formalism therefore reproduces this aspect of the data. However, under the assumption that the strangeness production volume is proportional to $\langle N_{part} \rangle$, the Grand Canonical limit is predicted to occur at $\langle N_{part} \rangle > 100$ independent of beam energy which is clearly not reproduced by the $\Lambda, \bar{\Lambda}, \Xi, \bar{\Xi}$ data at both energies in figure 1.5. Furthermore, even at the largest $\langle N_{part} \rangle$ values, the measured values of E for Λ and $\bar{\Xi}$ do not match the Canonical predictions. Unlike the case for the K/π ratio in Pb+Pb/Au+Au collisions, its appears that a complete thermal model description of strangeness yields per participant has yet to be achieved.

2.3.2 Baryon/Meson Anomalies

The integrated yields in the previous section are dominated by soft QCD processes, and it can be shown that for slope parameters in the hundreds of MeV, $\sim 99\%$ of the mid-rapidity yield in equation 2.6 occurs for $p_T < 2$ GeV/c. The mid-p_T interval typically corresponds to $2 \lesssim p_T \lesssim 5$ GeV/c. Figure 2.9 shows mid-p_T spectra for the Λ and K^0_S particles from Au+Au $\sqrt{s_{NN}} = 200$ GeV collisions. For the central

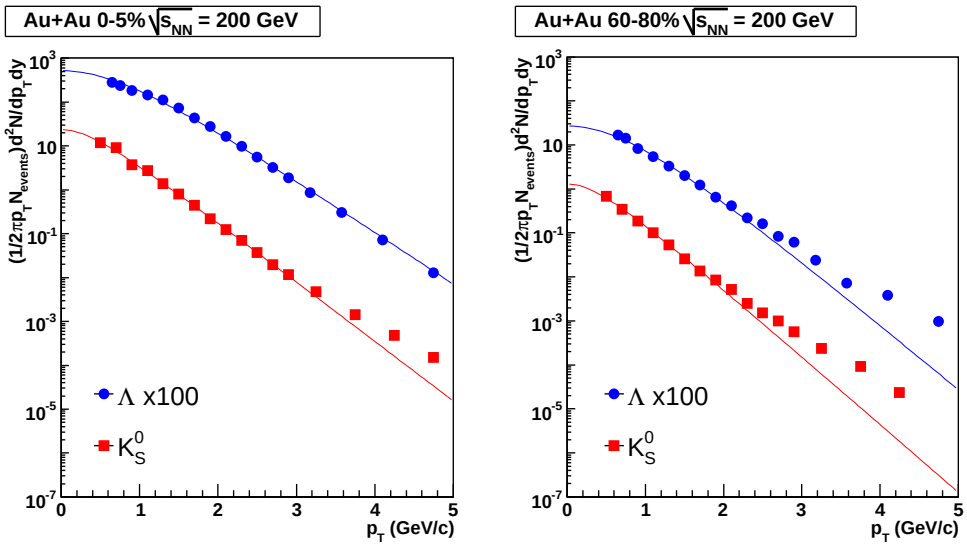

Figure 2.9: Mid-rapidity Λ and K^0_S spectra [51, 84]. The lines are m_T exponential parameterisations. The central and peripheral Λ slope parameters are 358 ± 4 and 290 ± 11 MeV respectively, while the central and peripheral K^0_S slope parameters are 318 ± 5 and 281 ± 7 MeV respectively.

Au+Au K^0_S particles, and peripheral Au+Au Λ and K^0_S particles, the exponential component expends to around 2.5 GeV/c then a tail develops which can be described by a power-law function i.e. $\propto p_T^{-m}$ where m is a positive number. It characterises two possible physical processes [81, 82]:

- Fragmentation from (semi) hard parton scatters
- Temperature/slope parameter fluctuations

As described in section 1.2, jets arise from scattered partons in the initial nucleons which then fragment into hadrons and this process is expected to dominate hadron production at high-p_T. Regarding the second point, when the m_T exponential slope parameter exhibits Gaussian fluctuations around a central value T, the resulting distribution is a Lèvy function [83]. This has a m_T exponential shape at low p_T and power-law shape at high-p_T. Thus the tails observed in figure 2.9 could also be due to transverse flow fluctuations and/or T_{th} fluctuations. The scale of the fluctuations is represented by the Lèvy exponent, n, and when $1/n \to \infty$ the m_T exponential is recovered over the full p_T range. The Lèvy function is as follows:

$$\frac{1}{2\pi p_T}\frac{d^2N}{dydp_T} = \frac{dN}{dy}\frac{(n-1)(n-2)}{2\pi nT[nT + m_0(n-2)]} \times \left(1 + \frac{\sqrt{p_T^2 + m_0^2} - m_0}{nT}\right)^{-n} \tag{2.12}$$

In order to compare and contrast the possible processes behind Λ and K^0_S mid-p_T production, the Λ/K^0_S ratio can be measured as a function of p_T and centrality. This is shown in figure 2.10 for Au+Au $\sqrt{s_{NN}} = 200$ GeV collisions. In the $p_T < 1$ GeV/c range, both centralities exhibit a Λ/K^0_S ratio of 0.3-0.5. In light of the phase space considerations discussed at the end of section 2.2.4, this is not surprising given the respective particle masses: $\Lambda \simeq 1.12$GeV, $K^0_S \simeq 0.50$ GeV. Differences arise for $p_T \gtrsim 1$ GeV/c; the peak of the distribution for central collisions is ~ 1.8, while for peripheral collisions this is ~ 0.8. A similar pattern is observed for p/π ratios in heavy-ion collisions [84, 85], and is commonly attributed to quark coalescence (or recombination) in the QGP transition contributing more to baryon production compared to meson production at mid-p_T. The TEXAS [86] and DUKE [87] coalescence models, which reproduce the shape of the Λ/K^0_S ratio, are shown in figure 2.10. Both models assume that as the QGP freezes out, hadron production can occur via the recombination of co-moving quarks under the influence of collective flow. This leads to the sum of the quark p_T equaling that of the hadron p_T. The underlying

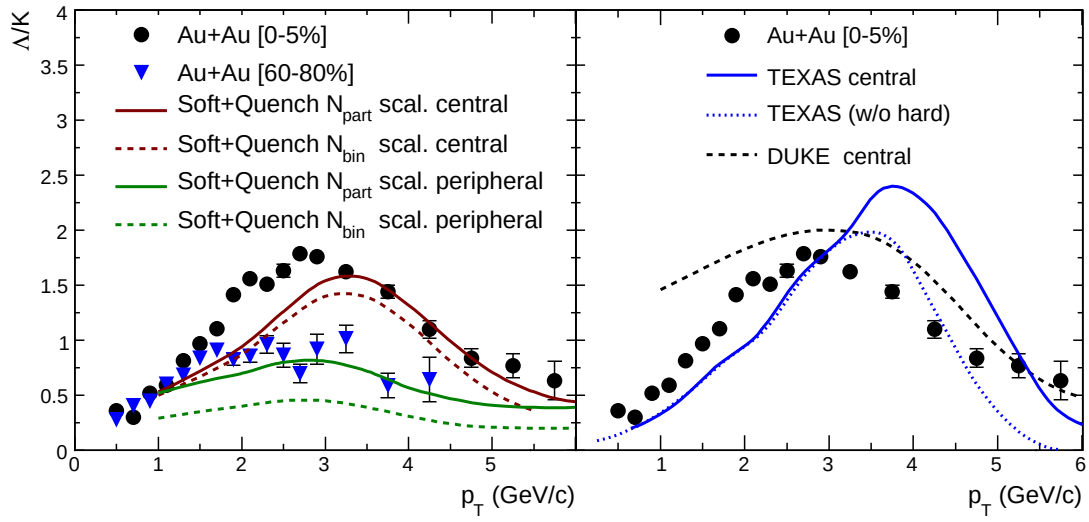

Figure 2.10: The Λ/K^0_S ratio as function of p_T for central and peripheral for Au+Au $\sqrt{s_{NN}} = 200$ GeV collisions [84]. The various models are discussed in the text.

momentum dependance of the parton distribution is thermal in character, and is thus proportional to $e^{-p/T}$ where T is the slope parameter. The result is a preference for baryon production at mid-p_T as there are more lower momentum patrons available to participate in baryon production, compared to the higher momentum patrons required for meson production. This is demonstrated schematically in figure 2.11. The models also allow for hadron production via QGP modified (semi) hard scattered parton fragmentation which dominates production for $p_T \gtrsim 5$ GeV/c. The TEXAS prediction shown by the solid curve, also allows hard scattered partons to coalesce with thermal partons (the dashed prediction does not). The authors of both models calculate that the effect of flow on mid-p_T Λ and K^0_S production is negligible in comparison to coalescence and fragmentation. Finally, it should be noted that coalescence cannot dominate hadron production (i.e. for $p_T \lesssim 2$ GeV/c) as the 2→1 and 3 → 1 processes do not conserve entropy.

In contrast to the TEXAS and DUKE models, the Soft+Quench formalism [88] assumes mid-p_T Λ production has contributions from baryon junction formation and (semi) hard scattered parton fragmentation, while K^0_S production is without the

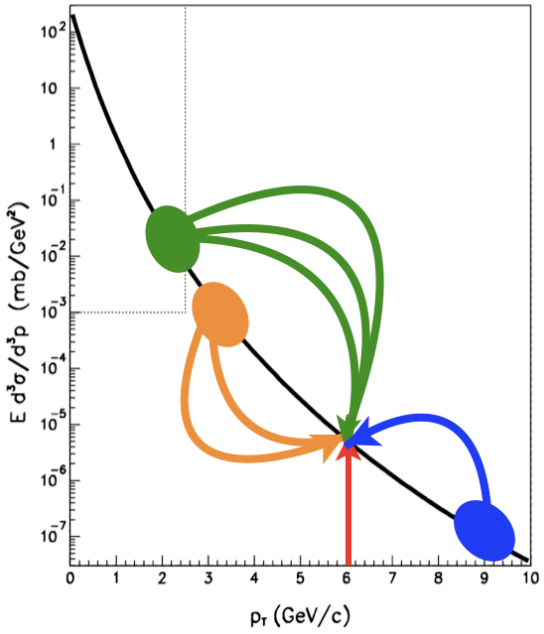

Figure 2.11: Schematic representation of quark recombination [89]. The black line shows the thermal parton spectrum, while the filled circles represent possible parton sources for hadron production.

junction contribution. These models also reproduce the shape of the Λ/K^0_S ratio for both centralities. Baryon junctions, which were originally conceived to describe how baryon number is transfered from beam-rapidity to mid-rapidity, are gluonic field configurations which are able to "carry" baryon number [32]. As baryons junctions do not suffer energy loss in the Soft+Quench model, the increase in the mid-p_T Λ/K^0_S ratio from peripheral to central collisions is due to more serve jet quenching in the latter reducing K^0_S production relative to Λ production. Although collective flow is included in the calculations, like for the coalescence models, the authors found that this does not influence the mid-p_T spectra for baryons and mesons in relation to the other processes. N_{part} scaling assumes that the produced junctions are proportional to the number of participating nucleons, while N_{bin} scaling assumes that the number of junctions are proportional to the number the binary collisions.

Finally, figure 2.12 shows R_{AA} for strange particles which is an alternative measurement to address possible baryon and meson differences. The K^0_S particles appear

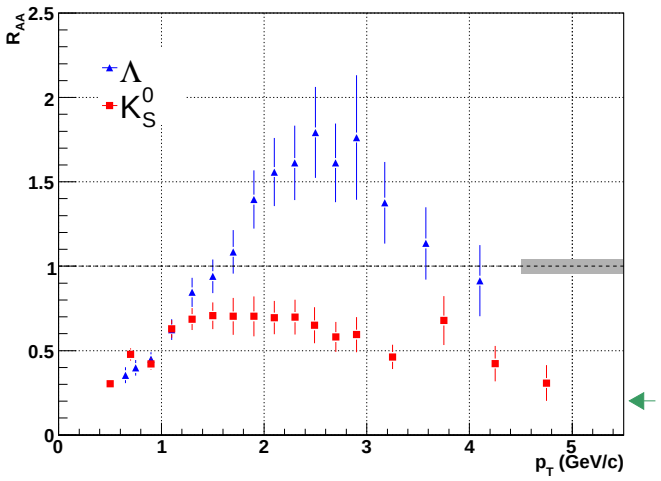

Figure 2.12: R_{AA} of K^0_S and Λ particles for 0-5% central Au+Au $\sqrt{s_{NN}}$ = 200 GeV collisions [51, 61, 84]. The grey box indicates the uncertainty in the number of Au+Au binary collisions, and the green arrow shows the approximate of value of charged hadron R_{AA} beyond 4 GeV/c.

to follow a similar pattern to charged hadrons in the left panel of figure 1.6: R_{AA} at low-p_T is 0.2 which then rises to $\sim$ 0.5 at mid-p_T, and finally falls back down to 0.2 at high-p_T. The Λ pattern is strikingly dissimilar with the largest differences occurring at mid-p_T. Again, similar differences are observed for proton and pions [85]. In this region, the higher values for baryon production is often linked to coalescence providing an extra source of particle production in relation to mesons. In addition, a version of the HIJING (Heavy-Ion Jet INteraction Generator) model which implements baryon junctions and modified jet fragmentation, also predicts $R_{AA} > 1$ for mid-p_T Λ particles [90]. This model includes colour rope formation, and the resulting higher string constants smear baryon production to higher p_T relative to the p+p case. In figure 2.12, at high-p_T the Λ values appear to tend to the K^0_S values implying that modified fragmentation starts to dominates particle production for both the Λ and K^0_S particles.

Chapter 3

THE STAR EXPERIMENT

3.1 The Relativistic Heavy Ion Collider

After its first successful experimental operation in the summer of 2000, the Relativistic Heavy Ion Collider (RHIC) has now been collecting data for 8 years. Within this period, the collisions of gold and copper nuclei in the energy range $\sqrt{s_{NN}} = 9 - 200$ GeV, have been investigated to study the quark gluon plasma. Collisions of polarized and un-polarized protons in the energy range $\sqrt{s_{NN}} = 62.4 - 500$ GeV, address additional aspects of QCD such as the gluon contribution to the proton spin, and provide a crucial baseline for heavy-ion measurements.

Figure 3.1 shows the layout of RHIC. A brief description of the operations is as follows [92]. In heavy-ion mode, negatively charged ions are sourced at the Tandem Van de Graaff where the electrons are stripped. The ions are accelerated to an energy of 1 MeV/c, and then travel towards the Booster. Here ions are stripped and accelerated further, and move towards the Alternating Gradient Synchrotron (AGS) with an energy of 95 MeV/A. In proton mode, the protons are sourced at the Linear Accelerator (LINAC) where they are accelerated to 95 MeV, then injected into the AGS. In the AGS, the ions are fully stripped (heavy-ion mode), then the protons or ions are bunched and accelerated to the RHIC injection energy of 10.8 GeV/A. They are then transferred to RHIC via the AGS-to-RHIC Beam Transfer

Line (ATR).

In the RHIC ring, two counter rotating beams are accelerated using RF (radio frequency) super-conducting magnets. The protons and ion beams can be accelerated to 250 GeV and 100 GeV/A respectively. A given beam will consist of either 60 or 120 bunches, and the RF frequency is 28.15 MHz which is an integer multiple of the bunch rate (number passing a given point in the ring per unit time) for either number of bunches. There are six interaction points, and focusing of the bunches is done via dipole and quadrupole electromagnetic fields at these points. Of the six interaction points, four of them house the STAR, PHENIX, BRAHMS and PHOBOS experiments. BRAHMS and PHOBOS stopped recording data in 2005, while STAR and PHENIX continue to run to date.

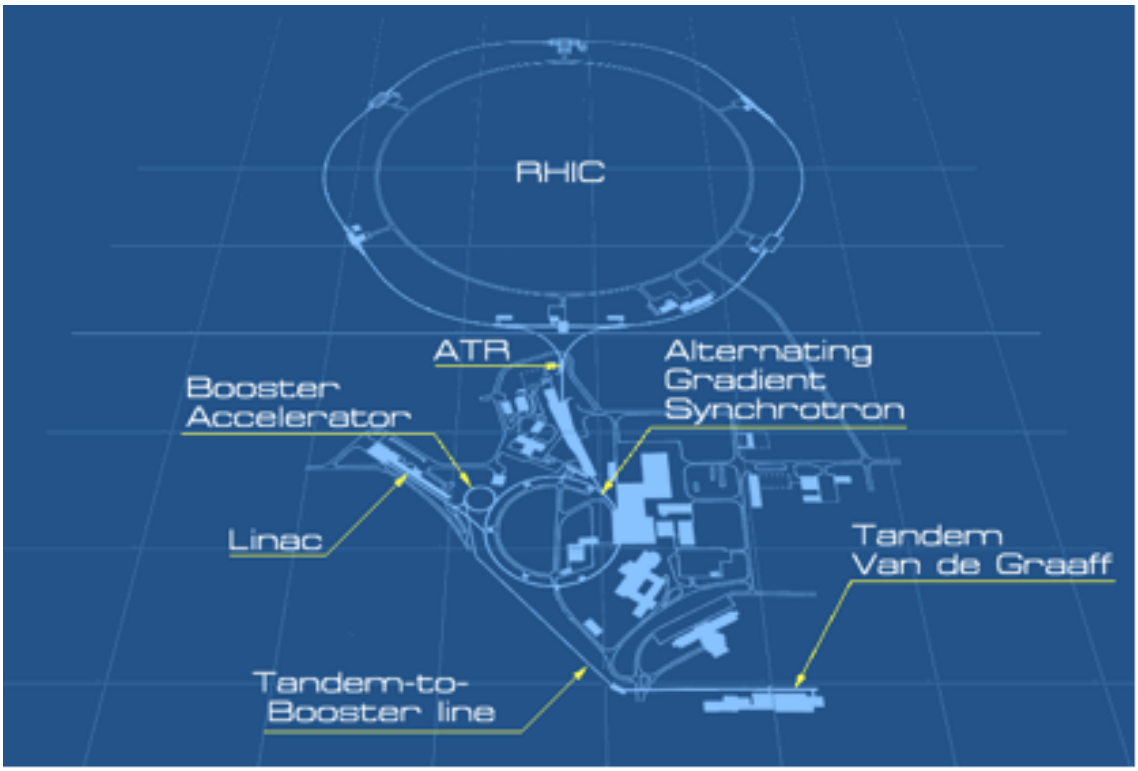

Figure 3.1: An overview of the RHIC complex [93]. The circumference of the ring is 3.8 km.

3.2 Overview of STAR

Figure 3.2 shows the Solenoid Tracker At RHIC (STAR). In the STAR coordinate system, z is along the beam direction, the y direction is vertical, and the x direction is perpendicular to the zy plane. The field from the STAR magnet which is applied in the z direction, bends the trajectories of charged particles enabling momentum measurements. The Central Trigger Barrel (CTB) and Zero Degree Calorimeters (ZDCs) are the main trigger detectors and will be discussed in more detail in the next section. The Time Projection Chamber (TPC), is the main tracking detector and is capable of measuring charged particles with $p_T \gtrsim 0.1$ GeV/c and $|\eta| < 1.8$ [1] with complete azimuthal coverage in the xy plane [94]. The azimuthal angle is denoted by ϕ. Particle identification is also possible via measurements of energy loss per unit lenght (dE/dx) which will be discussed in sections 3.4.2 and 5.2.1.

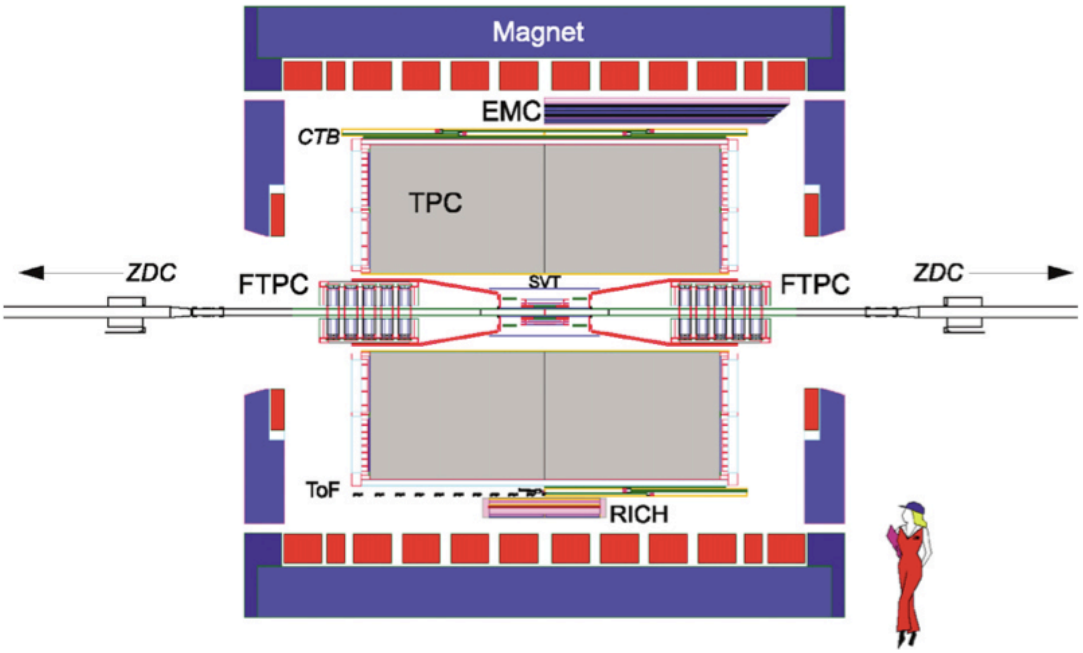

Figure 3.2: An overview of the STAR experiment. The z axis is in the beam direction where z=0 is at the TPC membrane denoted by the central vertical black line [95].

[1] Acceptance is quoted with respect to $x = y = z = 0$ throughout this thesis

Together with the pseudo Vertex Position Detectors (not shown), the Time of Flight (TOF) detectors measure the time it takes for a charged particle to leave the collision vertex and hit a TOF element. Thus with the TPC measurements of momenta and track length, the TOF data offers particle identification via measurements of particle mass with a limited acceptance of $0 < \eta < -1$, $\Delta\phi = \pi/30$. Charged pions and kaons can be identified up to $p_T \sim 1.6$ GeV/c, and (anti) protons can be identified to $p_T \sim 3$ GeV/c [96]. The Silicon Vertex Tracker (SVT) can measure high precision particle hits close to the collision vertex, and thus improves track and vertex resolution when used with the TPC. The Forward Time Projection Chambers (FTPC) measure charged particles at forward rapidities with $2.5 < |\eta| < 4$. Finally, the Electromagnetic Calorimeter (EMC) allows for fast detection of high energy photons and electrons. The calorimeter is divided into two components; the Barrel EMC (partially shown) which has an acceptance of $|\eta| < 1$, and the Endcap EMC (not shown) which covers $1 < \eta < 2$.

3.3 The STAR Trigger

The main trigger detectors are the Zero Degree Calorimeters (ZDCs), the Central Trigger Barrel (CTB)[2], and the Electromagnetic Calorimeter (EMC). The purpose of the STAR trigger is to instruct the slower detectors on when to record data. The criterion for this decision is varied. The trigger can be used to select central A+A collisions, events with a high energy particle with EMC data, or ultra peripheral collisions which involve photon exchanges that excite the nuclei and produce only a few particles. The most commonly used configuration is the minimum bias trigger which selects hadronic events with a range of centralities without a deliberate preference. This configuration was used for Cu+Cu $\sqrt{s_{NN}} = 200$ GeV events in this analysis.

[2]Although removed in 2008, it was used in the data taking for the current analysis.

The two ZDCs are positioned at ±18.25 metres along the beam axis relative to $z = 0$. Their purpose is to determine the energy of the spectator neutrons resulting from a heavy-ion collision. For a minimum bias trigger, a coincidence between the two ZDCs is required with a summed signal greater than $\sim$ 40% of a single neutron signal. Because of the required coincidence, the timing difference allows for an event's z-position to be determined online. An online z cut is often placed to ensure triggered events roughly occur in the middle of the TPC (z=0) where typical detector acceptance is most favourable. The CTB which encircles the TPC has an acceptance of $|\eta| < 1$ and consists of an array of 240 scintillator slats. The signal of each slat is approximately proportional to the number of charged particles that have traversed it. When used with the ZDCs, the centrality of an event can be determined online. Figure 3.3 shows the correlation between the ZDC and CTB signals. Peripheral events (large impact parameters) typically correspond to a high

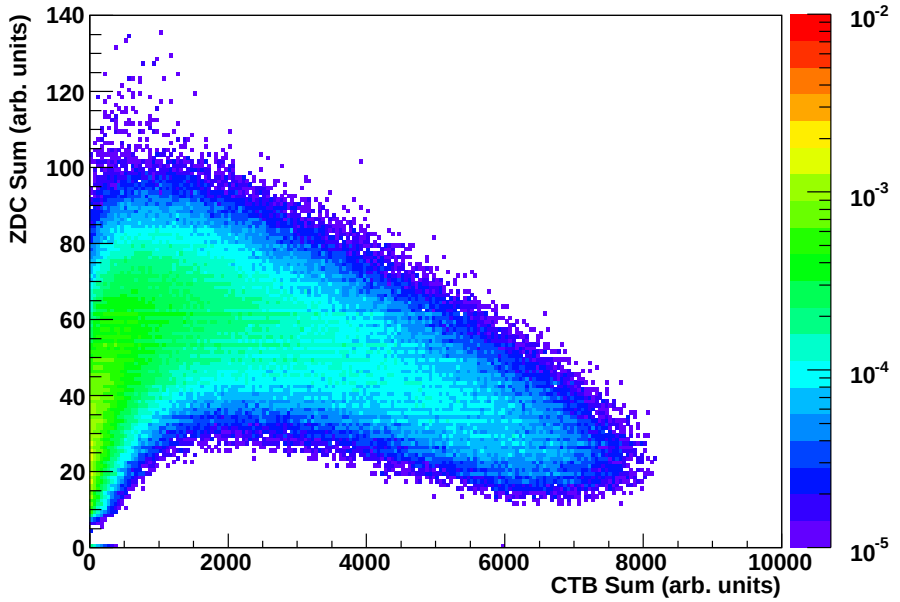

Figure 3.3: A correlation between the ZDC and CTB counts for Cu+Cu $\sqrt{s_{NN}} = 200$ GeV collisions. The density units are fractions of the total integral.

ZDC sum and a low CTB sum. This is simply because the number of spectator neutrons is large, and the number of charged particles produced is small. Conversely,

central collisions will have a high CTB sum and a low ZDC sum because of the high number of charged particles produced, and the low number of spectator neutrons involved. This allows the trigger be to configured in order to select upon centrality. As an example, the year 4 Au+Au $\sqrt{s_{NN}}$ = 200 GeV run had a central trigger which required a CTB sum of above 3500 (arbitrary units) and ZDC Sum below 130 (arbitrary units), and this resulted in the triggered events having a centrality in the 0-12% range with respect to the reference multiplcity (see section 2.2.2 for definition). The Electromagnetic Calorimeters (EMC) can be used to select events with rare probes such as high energy γ and π^0 particles, or electrons from J/ψ and Υ decays.

The algorithm which instructs the slow detectors on whether to record data consists of four levels which have differing timing constraints. The configuration of all four levels depends on the trigger requirement as discussed earlier. Level 0 receives information from the ZDCs, CTB, and the EMC for every bunch crossing, thus has a timing constraint of ∼106 ns (for 120 bunches). The ZDC sum, CTB sum, and the z position are available on this level, as well EMC information on high energy hits. If the interaction passes the event selection, a trigger is issued to the slow detectors. Level 1 and 2 will then carry out further processing, and work with the larger time constraints of 100 μs and 5 ms respectively. Full EMC information is available at level 2. For a minimum bias trigger, both levels are not required for further event selection. However, for the exotic Υ trigger, the invariant mass from pairs of EMC hits can be measured, and if this falls within the Υ mass band, the event is kept. Beyond level 2, the data acquisition (DAQ) system is responsible for the collection of data from all detectors. Before this is transferred to a hard disk and/or data tape, level 3 can be then used for further event selection with information from all the STAR detectors available. It is also used to create an online event display as shown in figure 3.6.

3.4 The Time Projection Chamber

Figure 3.4 shows the Time Projection Chamber (TPC), the main tracking detector at STAR. As mentioned in the overview, its principal objective is to measure the momentum and energy loss of particles emerging from the collision. It is surrounded by a uniform magnetic field in the z direction which can be maintained at either 0, ± 0.25 or $\pm$ 0.5 Tesla. Between the inner and outer field cages, the cathode membrane supplies an electric field of 135 V/cm in the z direction. The potential at the cathode is -28kV and drops to 0 at the end-caps where the sectors are located. The field cages consist of a series of Cu strip resistors which act as equi-potential rings to keep the electric field uniform within the drift volume, which itself contains an P10 argon-methane gas mixture maintained at atmospheric pressure.

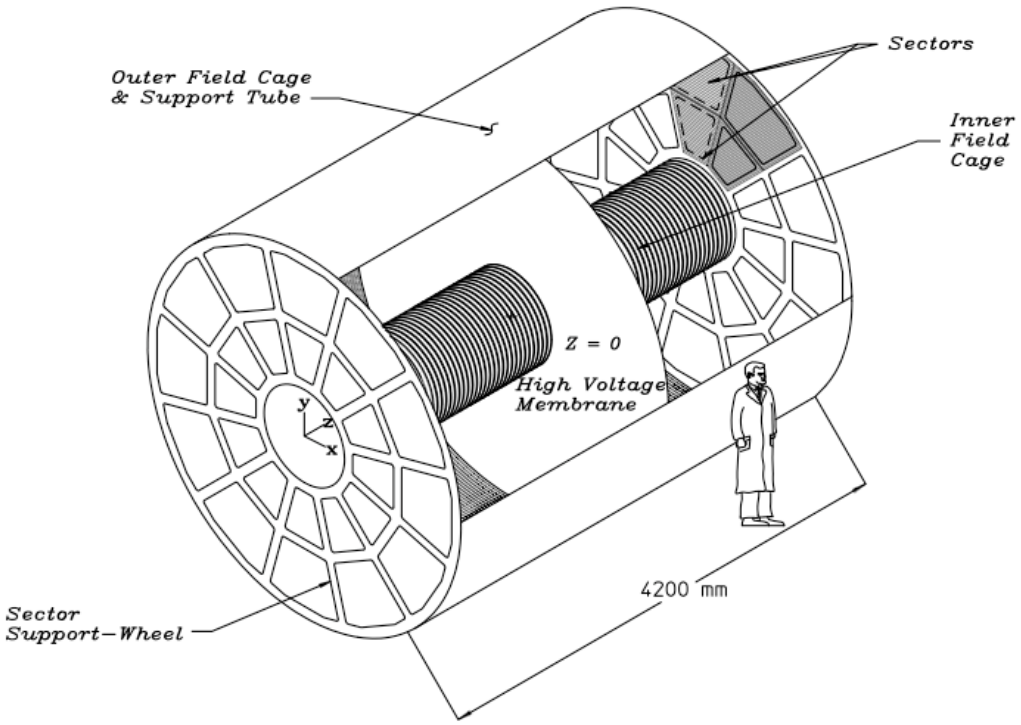

Figure 3.4: The STAR Time Projection Chamber. The length is 4.2m and the radial distance of the inner and outer sectors is 0.5 and 2m respectively [94].

Charged particles traversing the TPC will follow a curved trajectory in the xy

plane due the magnetic field, and subsequently leave a trail of ionised atoms in the active volume. Under the influence of the electric field, the liberated electron clouds drift with an average velocity 5.45 cm/μs towards the readout plane which is divided into the sectors, while positive ions drift towards the membrane. The maximum drift time is $\sim$ 40 μs. At the readout plane, the electrons encounter a gating grid which either lets the electrons pass or stops them. If the trigger permits, the gating grid is opened and the moving electrons will then pass through a shielding grid which marks the start of the proportional region. The inner and outer sectors in this region contain anode grids maintained at 1.1 kV and 1.39 kV respectively, which serve to amplify the drift electrons by accelerating them and creating an avalanche of electrons via secondary ionisation. The number of avalanche electrons is proportional to the number of drift electrons, where the ratio is referred to as the gain, and for the inner and outer sectors this is approximately 3770 and 1230 respectively [94].

The positive ions created in this process then induce an image charge on cathodes pads. The charged is digitized to give an ADC value for every pad. Each endcap is arranged into 12 sectors with each sector containing 45 rows which indicate the x, y position of the elements of a track. A sector is divided into an inner and outer sector as shown in figure 3.5. The pad density is higher for the inner sector due to the higher track densities there. The pad dimensions are chosen so that a drifting element will deposit charge over 3 pads in a row, and this configuration leads to optimal position resolution. If a Gaussian is used to determine the centroid, the uncertainty represented by the Gaussian width is typically 20% narrower than the pad width. The x, y position of the cluster is thus determined by the radial distance of the pad row and the centroid from the Gaussian fit. The arrival time of the drifting element is used to deduce the z position, as the drift velocity and the time of the collision (via the trigger) are recorded. For a triggered collision, each pad

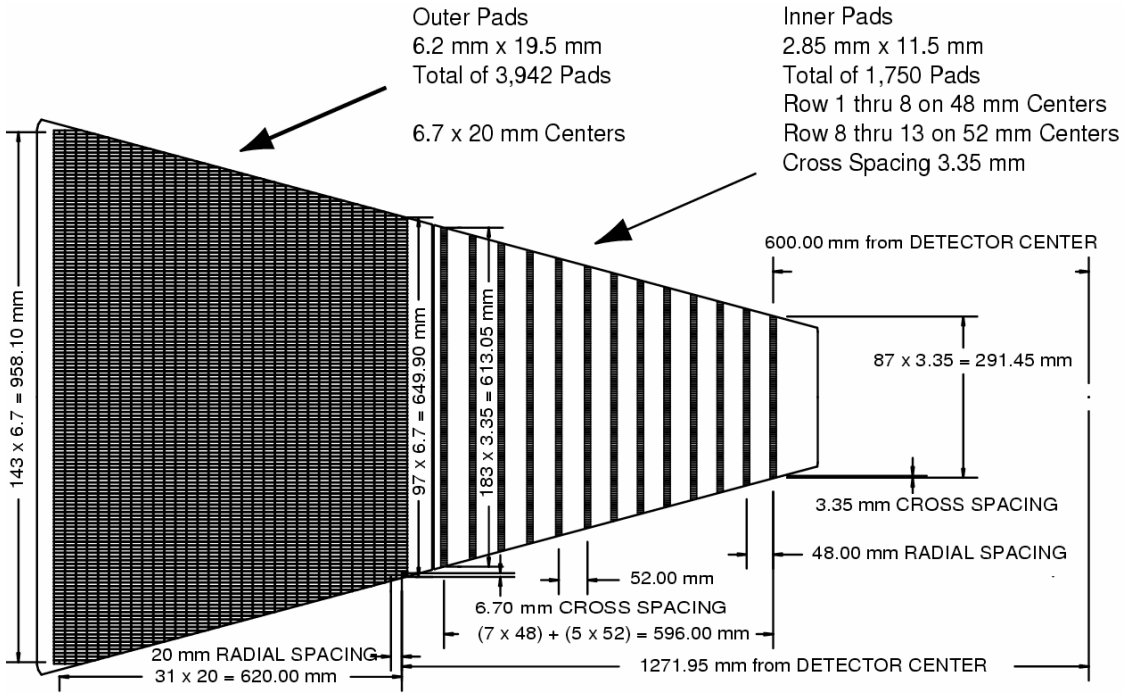

Figure 3.5: The anode pad plane of one full sector. The inner sector is on the right and it has small pads arranged in widely spaced rows. The outer sector is on the left and it is densely packed with larger pads [94].

is read 512 times (i.e. there will 512 ADC values per pad) which leads to a time interval of $\sim$ 100 ns. As the signal from a drifting element of charge will often cover several time intervals due to diffusion, a weighted average is taken (weights will depend on signal strength in time interval), and the extracted mean is used to determine the z position of the element. The recorded x, y, z position is thus known as a hit. In total, around $\sim$ 70 million pixels are available in order to take a 3D picture of the charged particles emerging from an event.

Finally, corrections have to be applied to the hit positions before track reconstruction takes place. This is because the apparent x, y, z position is not quite the true position due to factors distorting the motion of the drifting element. Principally, these are slight non-uniformities in the electric and magnetic field which arise from [97]:

- Field misalignment: There is a small but finite $E \times B$ term, and the TPC z direction is not exactly parallel to both the E and B fields.

- Space charge distortion: The liberated ions can perturb the E and B fields in the drift volume. This is most severe for the inner sectors where track density is highest.

- Grid leak: A thin sheet of avalanche electrons enters the drift volume from a region between the inner and outer sectors which again perturbs the E and B fields.

All items are corrected for by mapping the fields with further measurements and applying the necessary corrections to the trajectories of drift electrons. Another process which can affect the motion of the drift electrons is natural diffusion due to interactions with the gas. However, as this is a random process, no systematic correction can be applied and it thus serves only to limit the position resolution.

3.4.1 Track Reconstruction

In track reconstruction, hits are connected to construct the 3D trajectory of the charged tracks. The maximum number of TPC hits a track may have is 45 as this corresponds to the number of pad rows. Tracking starts at the outermost pad row where the hit density is lowest. Firstly, a set of 3 hits close in space is identified. These are fitted with a straight line, and the inward extrapolation is used to find additional hits. If located, a helix is associated with all the hits, and collectively this is known as a segment. The hits associated with the segment are then removed from the hit pool, and the process is repeated until all possible segments are found. Starting with the largest segments, the helix is projected inwards and outwards in order to find additional hits which were not removed from the pool previously. Segments are then merged if they result from split tracks. After this, the segments

are simply known as the tracks. The curvature of the track helix can then be used to determine the transverse momentum using the expression:

$$p_T = 0.3BRq \text{ (GeV/c)} \tag{3.1}$$

where B is the magnitude of the magnetic field (T), R the radius of curvature (m), and q is the charge of the particle (units of electron charge). Using the track azimuthal and dip angles (relative to the beam), all three momentum components can then be calculated. The finite spatial resolution and track length leads to a finite momentum resolution. In order to provide a better estimate of track momentum, a Kalman Filter was used for the year 5 Cu+Cu $\sqrt{s_{NN}} = 200$ GeV run [98]. This replaces the helix fit with a more realistic parameterisation that takes into account multiple scattering and energy loss in the beam pipe, inner trackers, inner field cage, and TPC gas. Finally, as regards the performance of the TPC, track multiplicities in excess of 3000 per collision with momenta above ∼100 MeV/c can be reconstructed [94]. Figure 3.6 shows tracks reconstructed from a central Au+Au event.

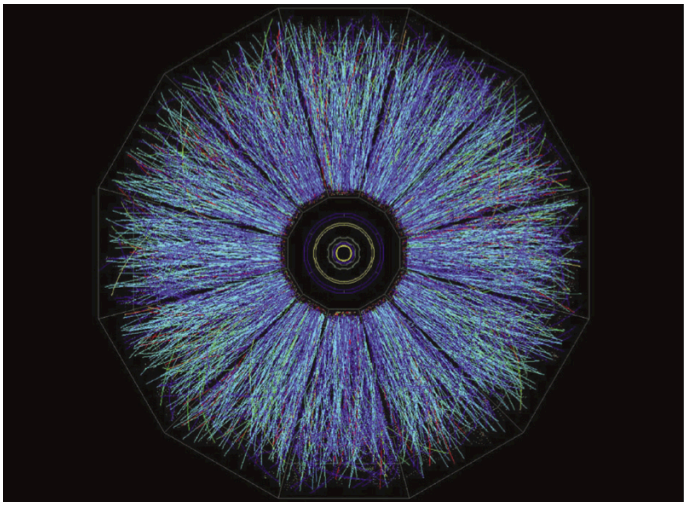

Figure 3.6: TPC tracks from a central Au+Au event [95].

3.4.2 Energy Loss

As a charged particle ionises the TPC gas, it will lose energy which is transfered to the liberated electrons. For a given cluster, the energy loss per unit length (dE/dx) is measured by associating the sum of the drift electrons with the energy loss, and dividing this by the track pathlength across the sensitive pad length. Hits with charge clusters that overlap other hit clusters are not used due to possible contamination of the summed electron value [99]. For a given a track, the spread of dE/dx points follows the Bichsel function [100]. The top 30% dE/dx points are excluded to determine the truncated mean which approximates the most probable Bichsel function dE/dx value. For a given track momentum and particle mass, the most probable Bichsel values can be predicted using the following which is an extension of the Bethe-Bloch formula [101]:

$$-\frac{dE}{dx} = Kz^2\frac{Z}{A}\frac{1}{\beta^2}\left[\frac{1}{2}\ln\left(\frac{2m_e c^2\beta^2\gamma^2 T_{max}}{I}\right) - \beta^2 - \frac{\delta^2}{2}\right] \tag{3.2}$$

where z is the integer charge of the particle, K is a constant, Z is the atomic number of the absorber, A is the atomic mass of the absorber, m_e the electron mass, c the vacuum speed of light, I is the average ionisation energy of the material, T_{max} is the maximum knetic energy that can be given to a free electron in an interaction, δ is a correction based on the electron density, and $\beta\gamma = p/mc$ where p is the momentum and m is the mass of the charged particle. Comparing measured and predicted dE/dx values thus enables particle identification. Figure 3.7 shows Bichsel predictions against measured dE/dx values for positive and negative particles detected with the TPC. It is clear than kaons (blue lines) can be distinguished up to ~ 0.5 GeV/c and (anti) protons (red lines) up ~ 0.8 GeV/c. The pions, protons, kaons merge into a single band beyond this. On the left panel, the band to the right of the protons corresponds to deuterons. The typical number of dE/dx points

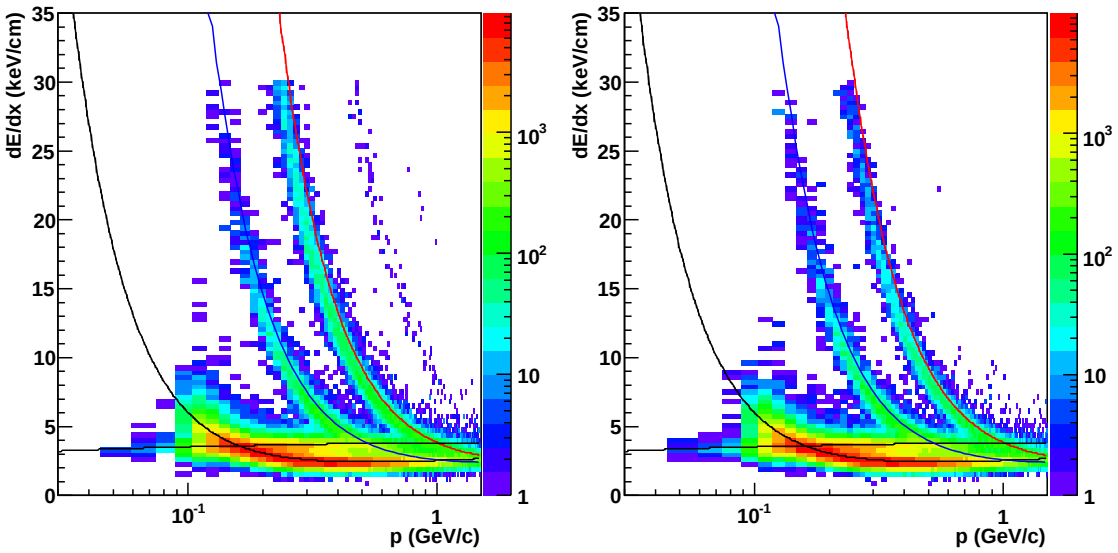

Figure 3.7: Energy loss for positive and negative tracks as a function of total momentum. The curves represent Bichsel predictions: black is for electrons, green is for pions, blue is for kaons, and red is for protons.

used is not quite sufficient to smooth out the effect of statistical fluctuations on the truncated mean, and this manifests itself via the spread of measured dE/dx values for a predicted value.

3.5 Information Storage

The event-wise pad ADC values are stored in a format known as a DAQ file, while event-wise track information is stored in a MuDst file which has a compressed file format [99]. The MuDst file will also contain information from other detectors such as the ZDC, CTB, and the TOF and is the most widely accessed file type in the STAR collaboration. For Cu+Cu $\sqrt{s_{NN}}$ = 200 GeV collisions, each event takes up $\sim$ 0.15 MB when stored in a MuDst, and the corresponding files are placed on distributed disks at the RHIC Computing Facility (RCF) [102]. Approximately 80 million collisions were recorded during the 2005 Cu+Cu $\sqrt{s_{NN}}$ = 200 GeV run, which gives a required disk space of $\sim$12 TB for MuDst storage.

Chapter 4

VERTEX FINDING AND CENTRALITY

Once the global tracks are reconstructed for a given event, the primary vertex (where the triggered event occurred) needs to be found. This enables primary tracks to be distinguished from sources of background. For Cu+Cu $\sqrt{s_{NN}} = 200$ GeV collisions, event multiplicities can range from a few charged particles, to in excess of 800 charged particles. Effective primary vertex finding needs to cope well with both extremes in order for meaningful physics to be carried out across the range of centralities. Due to an increase in beam luminosity, the Cu+Cu $\sqrt{s_{NN}} = 200$ GeV 2005 run was the first heavy-ion programme in STAR to suffer from pile-up. Methods of pile-up identification and rejection will be described, as well a method used to determine the vertex finding efficiency, which helped gauge the effectiveness of the rejection.

A method of centrality determination, which relied on simulating the multiplicity distribution for Cu+Cu 200 GeV collisions will also be shown. This used the N_{part} and N_{bin} output from a Monte Carlo Glauber calculation, then under a simple scaling hypothesis, both variables were mapped to multiplicity. Consequently, for a set of event-wise multiplicity cuts, the $\langle N_{part} \rangle$ and $\langle N_{bin} \rangle$ values can be extracted which are crucial for interpreting strange particle yields.

4.1 The MINUIT Vertex Finder

The primary vertex finding algorithm works firstly by scanning windows in z for vertex candidates as demonstrated in figure 4.1. The x, y position of the scan corresponds to 0,0 as this is the nominal beam line. If more than 5 tracks point within a 6 cm window in the z direction, this set is deemed a vertex candidate. Once a vertex candidate is identified, the position is determined by the MINUT minimization routine [103], which finds the x, y, z point with the smallest mean distance of closest approach (DCA).

Track fitting is then rerun with the vertex position as a fit constraint. After the tracking and reconstruction processes have finished, there will be a set of tracks with two copies. The copies that contain information prior to the re-fit are known as *global tracks*. Tracks with the vertex constraint are known as *primary tracks* as they originate from the vertex. As the position uncertainty in the vertex hit is typically less than a TPC hit and due to their larger length, the re-fit leads to a primary track having an improved p_T resolution compared to its global counterpart. As figure 4.1 demonstrates, there can be more than one vertex candidate in a triggered event. This is due to *pile-up*.

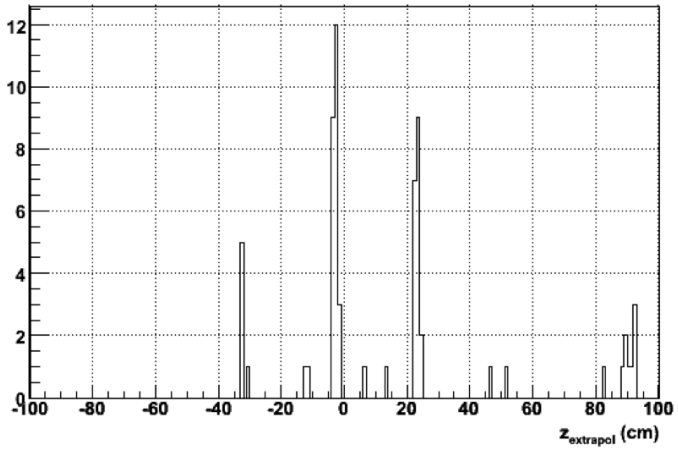

Figure 4.1: Number of tracks as function of extrapolated z position for a single Cu+Cu $\sqrt{s_{NN}} = 200$ GeV event [104].

4.1.1 Pile-up in the TPC

The Cu+Cu $\sqrt{s_{NN}}$ = 200 GeV run was the first heavy-ion program at STAR to suffer from significant pile-up. Pile-up occurs when the collision rate starts to become comparable with the drift time. This leads to events from previous/later bunch crossings being recorded with the event from the triggered bunch crossing. Figure 4.2 shows how pile-up tracks from an un-triggered event can result in additional vertices. The top two panels show the case when an pile-up event occurs before the

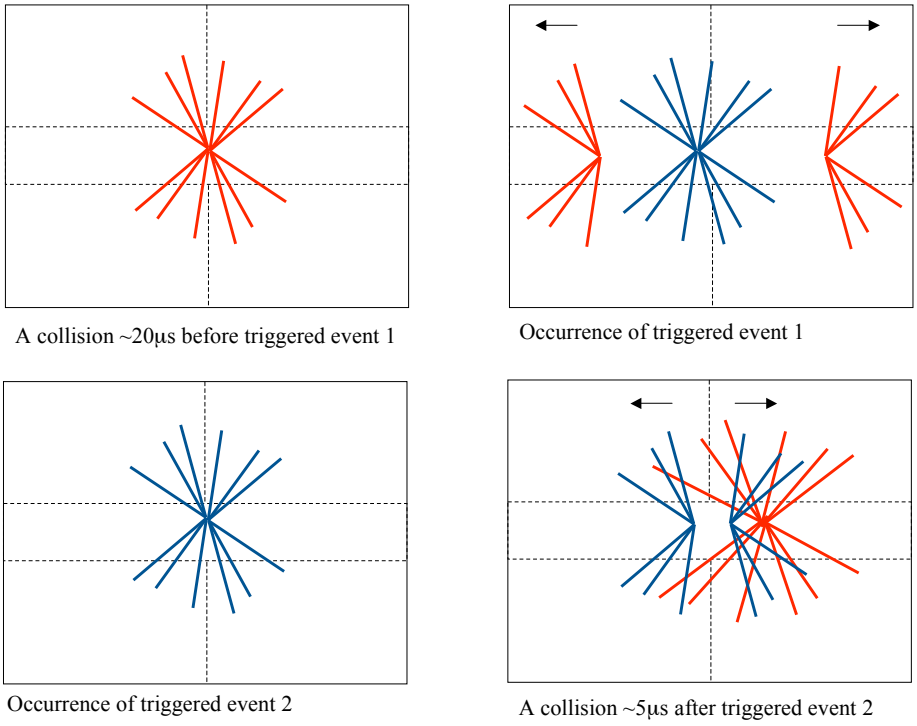

Figure 4.2: Illustration of pile-up in the STAR TPC. The top two panels show the result of a pile-up event occurring before the trigger, the bottom two shows this for after. The blue lines correspond to the triggered event tracks, the red lines correspond to pile-up event tracks. The horizontal dotted lines represent the inner field cage, and the horizontal solid lines represent the outer field cage. The vertical dotted line is the membrane, and the solid vertical lines are the endcaps.

triggered event. For the east ($z < 0$) and west ($z > 0$) sides of the TPC, a pile-up track's original position is shifted by $-\Delta t v_d$ and $+\Delta t v_d$ respectively, where Δt is

the time between the pile-up event and the triggered event, and v_d is the TPC drift velocity. Relative to the original track position, this leads to the apparent position in z being shifted towards the nearest endcap. The bottom two panels show the case where the pile-up event occurs after the trigger. For this instance, in the east ($z < 0$) and west ($z > 0$) sides of the TPC, a pile-up track's original position is shifted by $+\Delta t v_d$ and $-\Delta t v_d$ respectively. This leads to the apparent position being shifted away from the nearest endcap. Pile-up tracks that cross the membrane are thus split into two segments at $z = 0$, with the shifts corresponding to the afore mentioned relations. Two sets of split tracks lead to the possibility of two reconstructed vertices from the pile-up event. To test the description illustrated by figure 4.2, figure 4.3

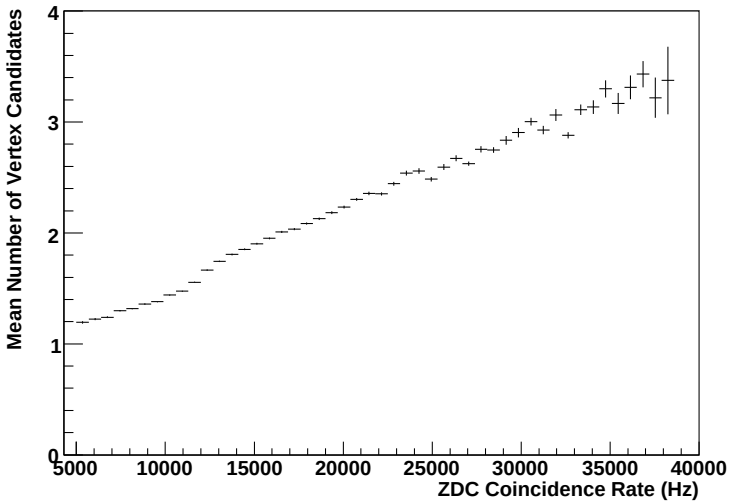

Figure 4.3: Mean number of vertex candidates as a function of ZDC coincidence rate. The uncertainties are statistical.

shows the mean number of vertex candidates as a function of ZDC coincidence rate, which is a measure of the collision rate. For a given trigger, the gating grid is opened for 40 μs which is the drift time from the membrane to the endcap. As figure 4.2 suggests, a pile-up event can happen $\sim 40\mu$s before the trigger, and ~ 40 μs after leading to a 80 μs window. A collision rate of 25000 Hz leads to a mean of 2 events per 80μs which gives an expected mean of 3 vertex candidates (one from trigger,

the other two from splitting) per trigger. This is slightly higher than the value of ~ 2.5 on figure 4.3, and is probably due to a partial vertex finding efficiency which will be discussed in section 4.3.

4.1.2 The Rank System

In order to ascertain which vertex candidate corresponds to the triggered event, i.e. the primary vertex, each candidate is assigned a *rank* [104]. The ranking has three numerical components based on the following:

- $\langle\eta\rangle$: The mean pseudo-rapidity of TPC vertex tracks
- n_b: Number of TPC vertex tracks which are matched to Barrel Electromagnetic Calorimeter (BEMC) hits
- n_m: Number of TPC vertex tracks which cross the membrane

For a given vertex, the components are summed to give the rank. The components are constructed so the higher the rank, the more probable the vertex corresponds to the triggered event. Therefore, for a set of vertices, the one with the highest rank is assigned the status of the triggered event. Regarding the determination of each of component, figure 4.4 shows each quantity for events with just one vertex candidate. The one vertex candidate will either correspond to the triggered event, or an event with one pile-up vertex as the triggered event's vertex has not been reconstructed. This event selection was used to determine the ranking components. As illustrated in figure 4.2, pile-up vertices are expected to point in a single direction with respect to z thus the magnitude of $\langle\eta\rangle$ is expected larger for split vertices. In the left panel of figure of 4.4, the pile-up vertices correspond to the two offshoots observed at the upper left of and bottom right of plot.

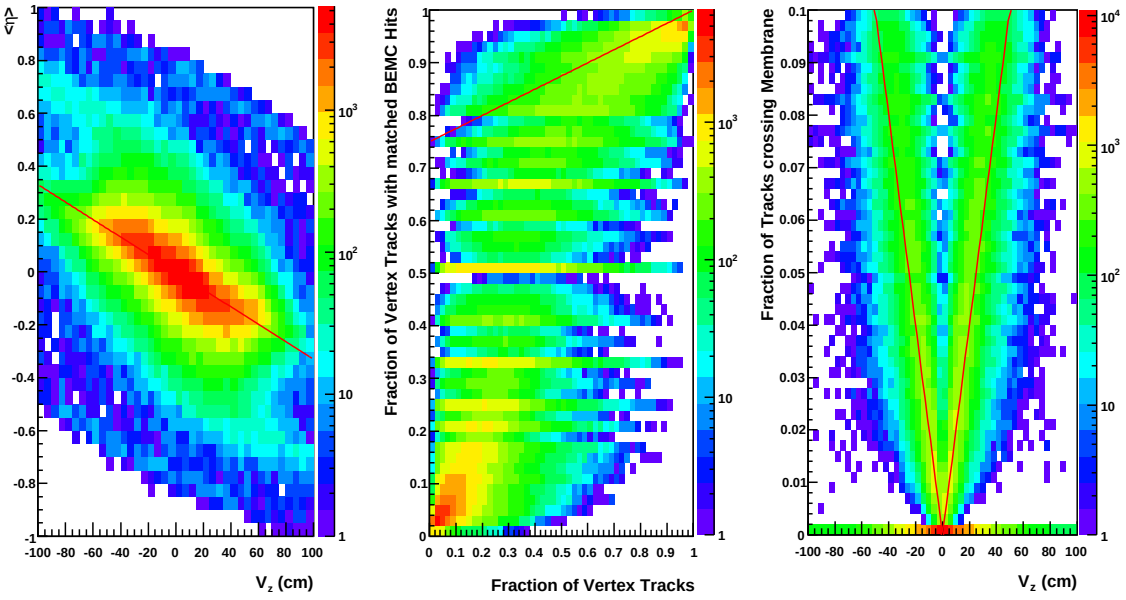

Figure 4.4: Left Panel: Mean pseudo-rapidity ($\langle\eta\rangle$) as a function of z position (cm). Middle Panel: The x-axis represents the number of vertex tracks for a candidate divided by the total number of vertex tracks used for all candidates. The y-axis represents the number of matched BEMC hits to vertex tracks for the given candidate divided by the total number of BEMC hit matched tracks for all vertex candidates. Right Panel: Fraction of vertex tracks that cross the membrane as a function of z position (cm).

The first component thus is constructed as:

$$C_1 = 1 - \frac{|\langle\eta\rangle - \langle\eta_e(V_z)\rangle|}{0.67}\sqrt{n_v} \tag{4.1}$$

where n_v is the number of primary tracks associated with the vertex. The $\langle\eta_e(V_z)\rangle$ factor is the expected mean pseudo-rapidity as a function of z position, and is shown by the red line in the left panel of 4.4. The magnitude of the difference between $\langle\eta\rangle$ and the expected value of $\langle\eta\rangle$, is divided by the standard deviation of $\langle\eta\rangle$ $(0.67/\sqrt{n_v})$. Therefore, C_1 becomes strongly negative if the magnitude of $\langle\eta\rangle$ and n_v are relatively large.

The second component is constructed as:

$$C_2 = \frac{n_b - \langle n_b \rangle}{0.5\sqrt{\langle n_b \rangle}} + 0.5 \tag{4.2}$$

where n_b is the number of BEMC hits matched to the vertex tracks. $\langle n_b \rangle$ is the expected number shown by the red line on the middle panel of figure 4.4. As demonstrated, this will depend on the fraction of tracks that belong to the vertex. The denominator is the standard deviation from the measured data. As the BEMC is a fast detector (its response time is smaller than the time between bunches), a pile-up track is not expected to have a matched BEMC hit. Thus if a pile-up vertex has $n_b \simeq 0$, C_2 will become negative. The value 0.5 ensures C_2 has a similar mean to the other components.

The third component is constructed as follows;

$$C_3 = \frac{n_c - \langle n_c(V_z) \rangle}{1.1\sqrt{\langle n_c(V_z) \rangle}} \tag{4.3}$$

where n_c is number of vertex tracks which cross the membrane, and $\langle n_c(V_z) \rangle$ is the expected number shown by the red line on the right panel of figure 4.4. Again, the denominator is the standard deviation from the measured data thus C_3 is expressed in units of standard deviation. As mentioned in the previous sub section, tracks from a pile-up event will appear not to cross the membrane, and this will typically lead to C_3 becoming negative for a pile-up vertex as $n_c \simeq 0$. This is apparent in the horizontal band in the right panel of figure 4.4. Finally, the minimum and maximum for a given component is set to -5 and 1 respectively as this ensures it does not get too much weight.

4.2 Pile-up Characterisation using the CTB

After the rank based vertex finding has been run, further tests were done to ensure that the vertex with the highest rank corresponded to the triggered event. As the CTB is another fast detector, and has an acceptance ($|\eta| < 1$) that overlaps with tracks which satisfy the reference multiplicity (Refmult) definition ($|\eta| < 0.5$)[1], there should be a strong correlation between CTB sum and the Refmult of events where the triggered vertex is identified correctly. Figure 4.5 confirms that most events

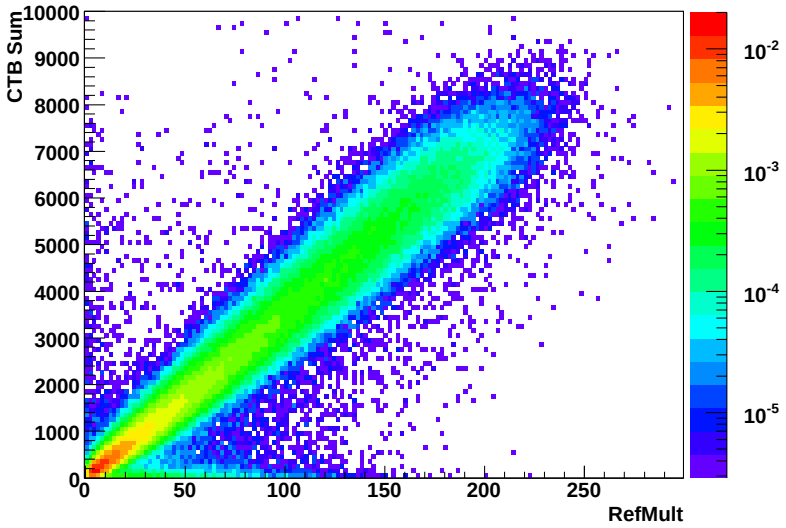

Figure 4.5: CTB sum as a function of reference multiplicity for Cu+Cu $\sqrt{s_{NN}} = 200$ GeV collisions. The event-wise reference multiplicity is determined from the vertex with the highest rank.

indeed exhibit a strong correlation for these two variables. However, there is an offshoot with low CTB sum and relatively high Refmult, which merges with the main distribution at Refmult ~ 20. To investigate this further, $\langle\eta\rangle$ is shown as a function of CTB sum in the left panel of figure 4.6. Three populations are observed; two with low CTB Sum and large $|\langle\eta\rangle|$, and one with large CTB sum and $\langle\eta\rangle \sim 0$. The vertices with low CTB sum appear to correspond to a pile-up vertex falsely identified as the triggered vertex. To seek further confirmation, figure 4.7 shows

[1]Tracking for the RefMult determination in this thesis used TPC hits only.

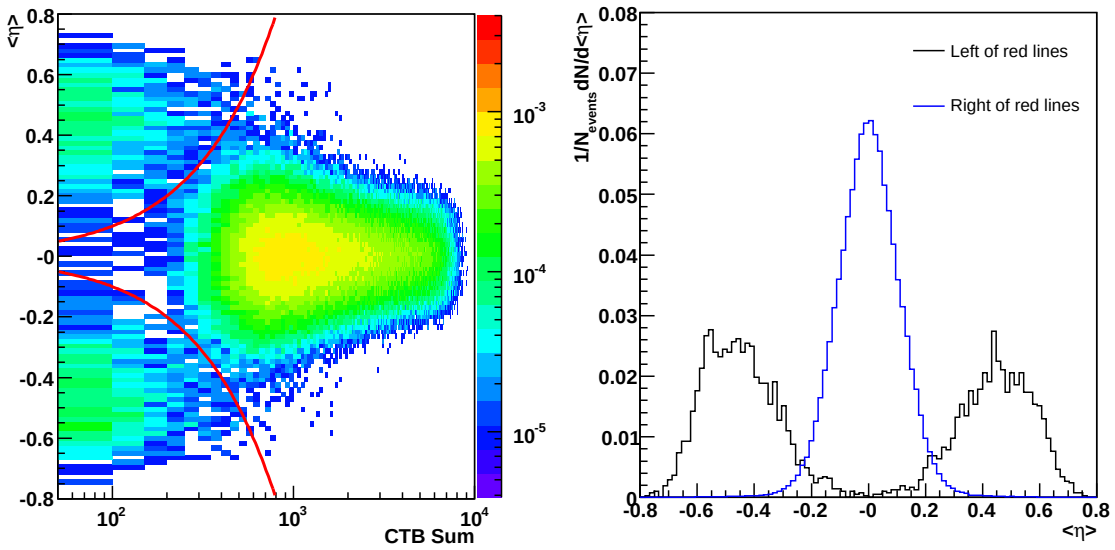

Figure 4.6: Left Panel: CTB sum as a function of mean pseudo-rapidity for primary vertices with RefMult ≥ 17. The parameterisations (red lines) are $y = (\pm 0.8/800)x$. Right Panel: Projections of the mean pseudo-rapidity with respect to CTB sum. Each projection is normalised by the number of events specific to the projection.

the rank and Refmult distributions for vertices to the left and right of the red lines in the left panel of figure 4.6. As expected, the pile-up vertices have roughly half the mean number of tracks and a lower mean rank. They contribute roughly 2% of events with reference multiplicity (RefMult) ≥ 17, and can easily be removed by placing a 2D CTB sum-$\langle\eta\rangle$ cut corresponding to the parameterisations in figure 4.6.

The low CTB sum for these pile-up vertices imply that corresponding triggered events have a low multiplicity. The misidentification can either be due the triggered vertex not being reconstructed (and the pile-up vertex with the highest rank is labeled the triggered vertex), or fluctuations in rank leading to a pile-up vertex gaining a higher rank than the triggered vertex. Pile-up identification is more difficult at Refmult < 17 as the three distributions in the left panel of figure 4.6 merge.

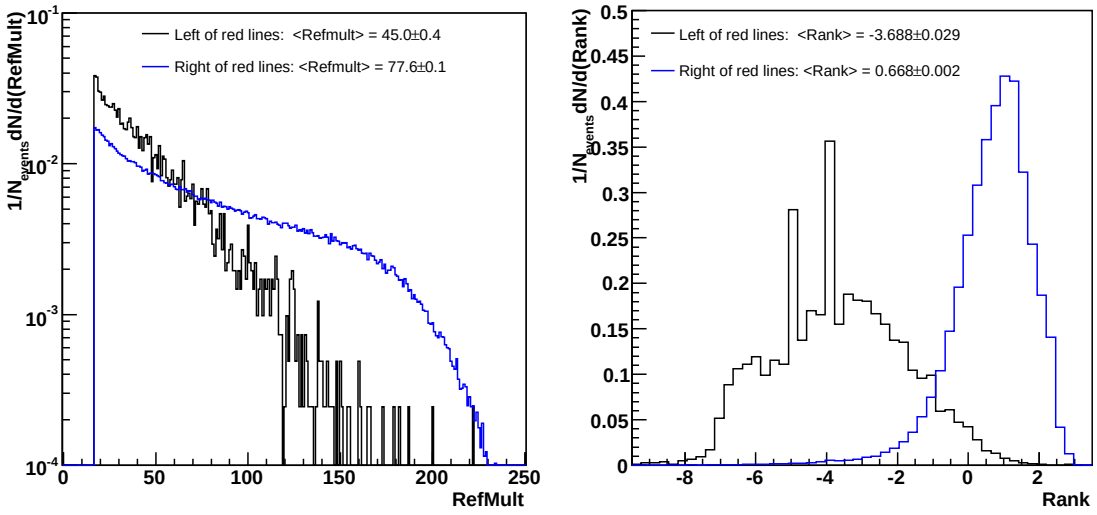

Figure 4.7: Left Panel: RefMult distributions of real and pile-up vertices with RefMult $\geq$ 17. Right Panel: Rank distributions of real and pile-up vertices with RefMult $\geq$ 17. Both legends refer to the parameterisations in the left panel of figure 4.6 and uncertainties associated with the mean values are statistical.

4.3 The Vertex Finding Efficiency

There are events where the vertex is not located as the result of a partial vertex finding efficiency, $\epsilon_V < 1$. This is simply defined as the ratio of vertices found to triggered events. Determining ϵ_V helps gauge the effectiveness of any pile-up rejection cuts as for the case where the triggered vertex is not found, a pile-up vertex will be labelled as the triggered vertex artificially inflating the efficiency. Therefore, if the vertex finding efficiency increases with ZDC coincidence rate, the pile-up cuts are not effective. As the main Cu+Cu $\sqrt{s_{NN}} = 200$ GeV trigger has an online z vertex cut $|V_z| < 50$ cm, this leads to a multiplicity bias at the z values near the cut due to the z resolution (from the ZDC) depending on multiplicity. An offline vertex z $|V_z| < 30$ cm is required to remove the bias [105], and also ensures uniform acceptance for TPC tracks within $\eta \lesssim 0.5$. For both these reasons, ϵ_V will be determined within $|V_z| < 30$ cm as this cut applies to the current analysis.

Before calculating ϵ_V for Cu+Cu collisions, it is important establish where the

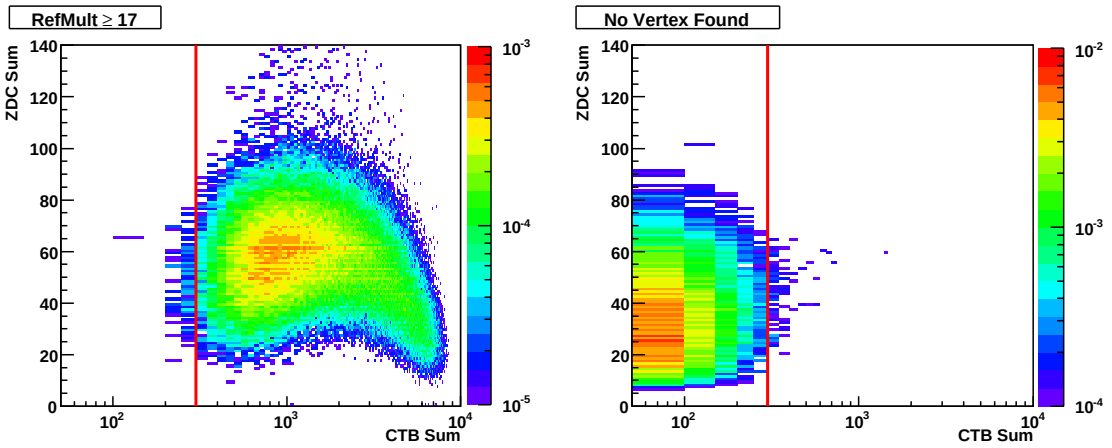

Figure 4.8: Left Panel: ZDC sum as function of CTB sum for triggered vertices with Refmult $\geq$ 17. Right Panel: Ditto for the case where no vertex is found. For each panel, the red lines are positioned at a CTB sum of 300.

vertex finding inefficiency applies to the RefMult distribution as this variable is used to define centrality. Previous studies have shown ϵ_V is $\sim$ 1 when an event creates over $\sim$50 TPC tracks, and then drops below one for fewer tracks [106]. Figure 4.8 shows the CTB sum - ZDC sum correlation for events with RefMult $\geq$ 17 within $|V_z| < 30$cm, and for events where no vertex is found (therefore V_z is unknown). For the RefMult $\geq$ 17 case, events with pile-up vertices identified as the triggered vertex have been removed using the CTB sum - $\langle\eta\rangle$ cut. As observed in figure 4.6, this cut only removes events with CTB sum < 300 for $|\langle\eta\rangle| > 0.3$ which contribute little to the main distribution. It is clear that there is very little overlap between the two distributions in figure 4.8 which indicates that triggered events with RefMult $\geq$ 17 always have their vertex identified. If this were not the case, the distribution in the right panel would show significant occupancies to the right of the red line.

Determining ϵ_V within a V_z range requires knowledge of V_z for events where the vertices are found and not found. The former can just use the z position reported from the vertex finder assuming the correct vertex is found, however it is clear that the later needs to utilise information from the ZDCs.

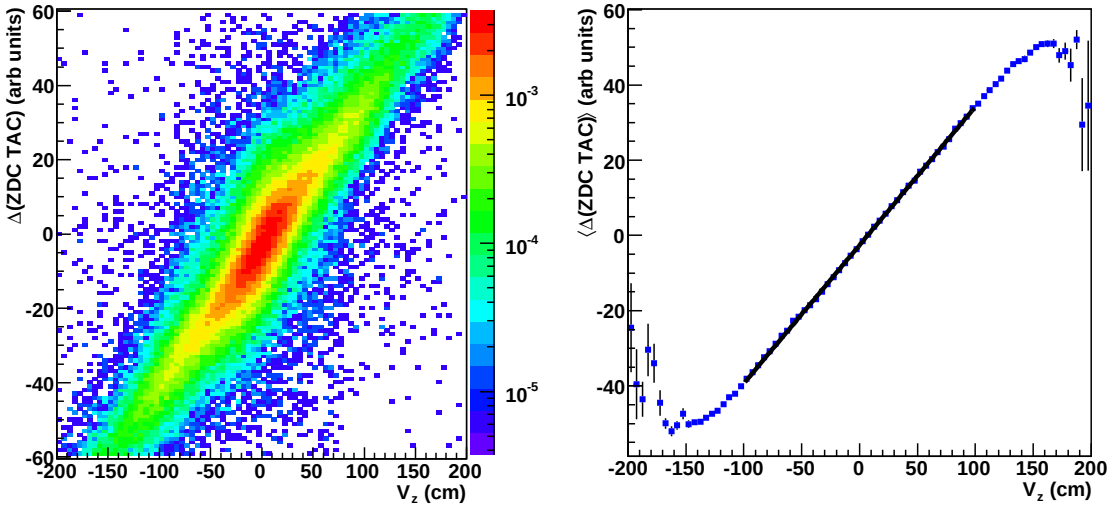

Figure 4.9: Left Panel: Difference in east and west ZDC TAC (Time to Amplitude Converter) values as a function of vertex V_z position for vertices with RefMult < 17 and rank > -1. Right Panel: Mean difference in east and west ZDC TAC values as a function of vertex V_z position for the same vertices. For V_z of -30 and 30 cm, the parameterisation gives $\langle\Delta(\text{ZDC TAC})\rangle$ values of -13 and 8 respectively. The uncertainties shown are statistical.

Figure 4.9 shows the ZDC time difference as a function of V_z position for found vertices. The mean time difference is proportional to the V_z position with the linear parameterisation in the right panel relating the two. As demonstrated in figure 4.7, rank >-1 ensures that nearly all the vertices correspond to the trigger, which prevents any mismatches between the TPC reconstructed and ZDC based vertex position. The vertex finding efficiency can now be defined as:

$$\epsilon_V = \frac{N_V(|TPC_{PV}| < 30cm)}{N_V(|TPC_{PV}| < 30cm) + N_{NV}(|ZDC_{PV}| < 30cm)} \tag{4.4}$$

where N_V corresponds to the number of vertices found within $|V_z| < 30$ cm using the based TPC information, and N_{NV} corresponds to the number of vertices not found within $|V_z| < 30$ cm using the TPC-ZDC parameterisation in the right panel of figure 4.9.

The black points in figure 4.10 show the vertex finding efficiency for events where

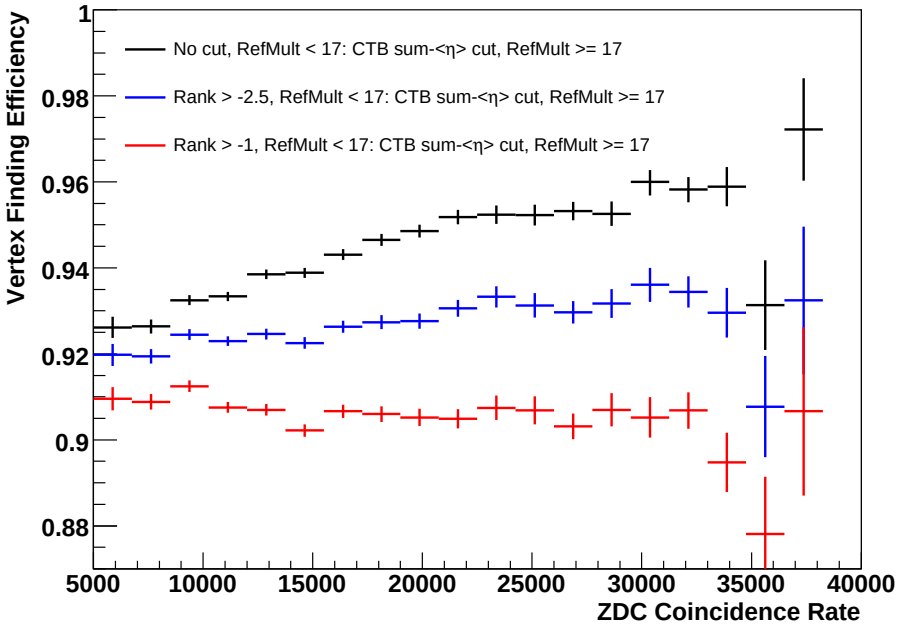

Figure 4.10: The vertex finding efficiency as a function of ZDC coincidence rate. The uncertainties are statistical.

the CTB sum-$\langle\eta\rangle$ cut is placed on events with RefMult ≥ 17. The vertices rejected by the cut are deemed to correspond to the case where the vertex is not found. The TPC-ZDC parameterisation is used to determined how many of these events actually occurred within $|V_z| < 30$ cm. However, there is a clear dependence on the ZDC coincidence rate, which indicates that for events with RefMult < 17, where the low multiplicity triggered events are not found, pile-up vertices are assume this role.

In an attempt to remove this dependence, a rank cut was placed on events with RefMult < 17 to remove pile-up vertices, then the vertex finding efficiency was recalculated. Again, rejected events were assumed to correspond to the case where vertex finding had failed, and the TPC-ZDC parameterisation was used to determine the triggered event's z position. The blue line shows events with a rank cut above -2.5. Naturally, the further event rejection serves to lower ϵ_V. However, there is little dependance on the ZDC coincidence rate indicating that the pile-up

cuts are now effective. A tighter rank cut of -1 again lowers ϵ_V, and there is little dependence on the ZDC coincidence rate. It was found that a lower rank cut of below -2.5 reintroduced the dependence, thus the cut of above -2.5 should be used to reject pile-up if events with RefMult < 17 are needed for analysis.

4.4 Centrality Determination

In this section, the centrality classes will be determined for Cu+Cu along with $\langle N_{part} \rangle$ and $\langle N_{bin} \rangle$ values for a particular class. The procedure involves simulating the Cu+Cu multiplicity distribution from N_{part} and N_{bin} calculated using the Monte Carlo Glauber method. The multiplicity distribution is simulated for centrality determination because of distortions in the measured multiplicity distribution due to the vertex inefficiency (shown in the previous section), and a possible trigger inefficiency affecting both the N_{Tot} and dN_{events}/dM terms in equation 2.3. The Monte Carlo Glauber calculation utilised previously written software [44] for Au+Au with the necessary adjustments for Cu+Cu. As described in section 2.2.2, the nucleons are sampled with a Woods-Saxon density profile for each nucleus which is given by:

$$\rho(r) = \frac{\rho_0}{1 + \exp\left[(r - c)/z\right]} \tag{4.5}$$

where r is the radial distance from the center of the nucleus, c is the half-density radius, and z is the skin depth. The density constant ρ_0 is chosen so $\rho(r)$ integrates to one over all possible values of r. For ^{63}Cu, c is taken to be 4.195 fm which is the sum of the measured proton value, and a Hartree-Fock prediction of the difference between neutron and proton values. z is taken to be 0.585 fm and this is calculated in a similar way [107]. After both nuclei have been filled, the collision is modelled by sampling an impact parameter, b, uniformly between 0 and b_{max}. The variable b_{max} is $2r_{max}$ where the maximum value of $r^2\rho(r)$ is factor of 10^4

higher than $r_{max}^2\rho(r_{max})$. Assuming all nucleons travel in straight lines, for the given impact parameter inelastic collisions are registered if two nucleons are separated by a distance smaller than:

$$r < \sqrt{\frac{\sigma_{NN}}{\pi}} \tag{4.6}$$

where σ_{NN} is the inelastic nucleon-nucleon cross section which is assumed equal to the p+p inelastic cross section at the same collision energy. At $\sqrt{s_{NN}} = 200$ GeV, σ_{NN} is taken to be 41.7 mb [110]. The whole process is then repeated until adequate statistics are achieved. Figure 4.11 shows the resulting N_{part} and N_{bin} distributions.

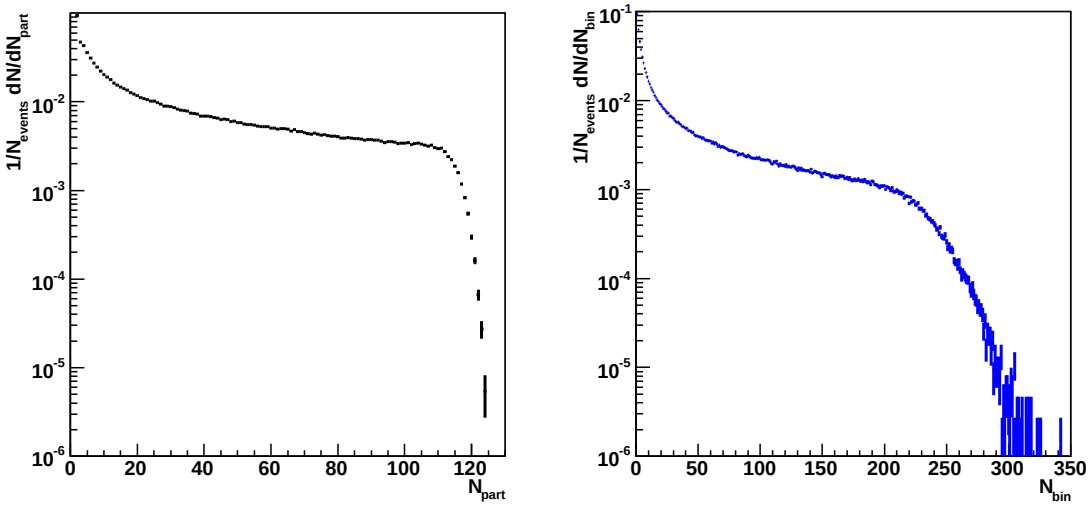

Figure 4.11: Left Panel: N_{part} distribution for 1 million Cu+Cu $\sqrt{s_{NN}} = 200$ GeV collisions. Right Panel: Ditto for N_{bin}. The uncertainties are statistical in both cases.

Both the Wood-Saxon parameters and σ_{NN} carry experimental uncertainties, and the effect of these on the extracted $\langle N_{part}\rangle$ and $\langle N_{bin}\rangle$ values will be investigated later. In section 1.3.3, it was stated that charged hadrons approximately scale with $\langle N_{part}\rangle$ which is characteristic of soft particle production [108]. However, at high collisional energies there may a hard component which scales with $\langle N_{bin}\rangle$ (such as mini-jets) that make a non negligible contribution to bulk particle production [109].

To allow for this, using the N_{part}, N_{bin} output, the Cu+Cu multiplicity distribution was simulated by invoking the Kharzeev-Nardi relation for a given MC Glauber event [109]. This has previously described the multiplicities in Au+Au $\sqrt{s_{NN}} = 200$ GeV collisions well [111, 112], and is given by:

$$\frac{dN}{d\eta} = (1-x)n_{pp}\frac{N_{part}}{2} + xn_{pp}N_{bin} \tag{4.7}$$

where $dN/d\eta$ corresponds to the simulated number of charged tracks in the RefMult rapidity range ($\eta < 0.5$), and n_{pp} is the measured p+p yield for the charged tracks in the same rapidity region. In Kharzeev-Nardi framework, it is assumed that particle production from soft process scales with N_{part}, and particle production from hard processes scales with N_{bin}. This relation is also observed for the widely used HIJING event generator [113] which is similar to the previously mentioned RQMD model as it computes hadron production via QCD string phenomenology. The relative weight of each contribution is characterised by x which will be a free parameter when the simulated distribution is fitted to the measured distribution. Prior to this fit, the measured distribution has to be corrected for TPC track reconstruction efficiency.

4.4.1 Correction Procedure for Measured Multiplicity Distribution

The aim of the correction is to remove any distortions due to a multiplicity dependent efficiency on the uncorrected RefMult distribution. In line with the observation in [107], the functional of form of the TPC track reconstruction efficiency is assumed as:

$$\epsilon(M_u) = \epsilon_0(1 - aM_u) \tag{4.8}$$

where M_u is the uncorrected multiplicity, ϵ_0 is the efficiency when $M_u \to 0$ and a is the drop in $\epsilon(M_u)$ per unit increase in multiplicity. The drop with increasing multi-

plicity merely reflects the fact that track reconstruction becomes more difficult with increasing TPC occupancy [106, 114, 115]. The correction procedure then utilises the fact that the uncorrected multiplicity distribution is the result (or convolution) of the corrected multiplicity distribution subject to a binomial process. For a given corrected multiplicity, M_c, and efficiency ($\epsilon(M_c)$), the probability distribution of M_u is:

$$p(M_u, M_c, \epsilon) = \binom{M_c}{M_u} \epsilon^{M_u} (1-\epsilon)^{M_c - M_u} \tag{4.9}$$

A corrected multiplicity distribution is postulated, and for each event with a given multiplicity M_c, the uncorrected multiplicity M_u is sampled from equation 4.9. All uncorrected multiplicities are summed to give an uncorrected distribution, and if this matches the measured uncorrected distribution, the corrected distribution is assumed the solution. In order to minimise CPU time, the event-wise corrected multiplicity values were postulated from low to high with equation 4.9 being sampled each time. A dummy histogram was filled with the uncorrected multiplicity (from the sample) providing the corresponding bin occupancy (after the fill), did not exceed that of the uncorrected measured distribution. If this condition was satisfied, a corrected multiplicity histogram was filled with the originally postulated value. The iteration terminated when the dummy uncorrected distribution matched that of the measured. In order to further check the validity of the solution, the corrected multiplicity distribution was sampled with equation 4.9 and this was found to give an uncorrected multiplicity distribution consistent with the original measured multiplicity distribution (which was uncorrected).

Figure 4.12 shows the corrected multiplicity distribution. The multiplicity distribution is plotted in two formats with the first aiding comparisons at high multiplicities (RefMult $\gtrsim 100$), and as first noted in [45] the second helps at low multiplicities (RefMult $\lesssim 100$, RefMult$^{1/4}$ $\lesssim 3.2$). The parameters used in equation 4.8 were determined retrospectively so the corrected $dN/d\eta|_{\eta<0.5}$ as a function of $\langle N_{part} \rangle$ cal-

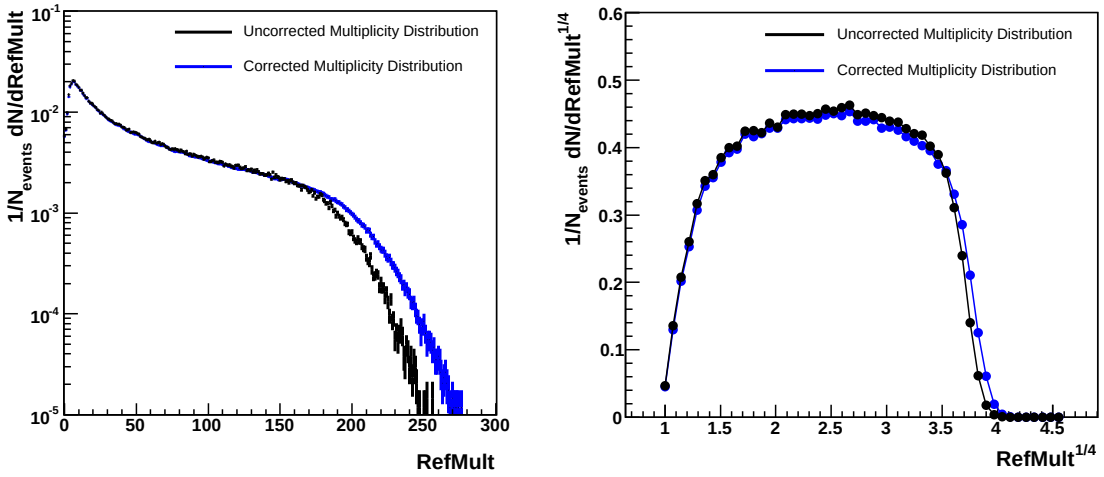

Figure 4.12: Comparison of uncorrected and corrected RefMult ($dN/d\eta|_{\eta<0.5}$) distributions for Cu+Cu $\sqrt{s_{NN}}$ = 200 GeV collisions. The uncorrected multiplcity distribution is subject to a rank cut of above -2.5 for events with RefMult < 17 and the previously used CTB sum-$\langle\eta\rangle$ cut for events with RefMult ≥ 17 in order to reject pile-up.

culated in the next section was consistent with the PHOBOS measurements [116]. In this case, $\epsilon_0 = 0.98$ and $a = 0.00025$, which gives efficiencies of $0.98 \rightarrow 0.91$ in the Cu+Cu multiplicity range.

4.4.2 The Simulated Multiplicity Distribution

In order to simulate the multiplicity distribution subject to the relation shown in equation 4.7, a negative binomial distribution was sampled in order to model fluctuations in multiplicity. This described the p+$\bar{\text{p}}$ $\sqrt{s_{NN}}$ = 200 GeV multiplicity distribution well [117] and is defined as follows:

$$p(n, \bar{n}, k) = \binom{n+k-1}{k-1} \left(\frac{\bar{n}/k}{1+\bar{n}/k}\right)^n \left(\frac{1}{1+\bar{n}/k}\right)^k \tag{4.10}$$

where $\bar{n}$ is the mean value of n, and k is related to the variance $\sigma^2 = \bar{n}(1+\bar{n}/k)$. For a given Monte Carlo Glauber event, equation 4.10 is sampled N_{part} times with

$\bar{n} = 0.5(1-x)n_{pp}$ and $k = 0.5(1-x)k_{pp}$, then sampled N_{bin} times with $\bar{n} = xn_{pp}$ and $k = xk_{pp}$ where n_{pp} and k_{pp} are the values obtained from a fit to the p+p multiplicity distribution. The sum of n from each sample is the event multiplicity, and the afore relations ensure that for a event ensemble with $N_{part} = 2$ and $N_{bin} = 1$ (limiting case) the p+p multiplicity distribution is reproduced. For p+$\bar{\text{p}}$ collisions at $\sqrt{s_{NN}} = 200$ GeV, the UA5 experiment reported $n_{pp} = 2.48 \pm 0.06$ and $k_{pp} = 2.3 \pm 0.02$ for the $\eta < 0.5$ region [117].

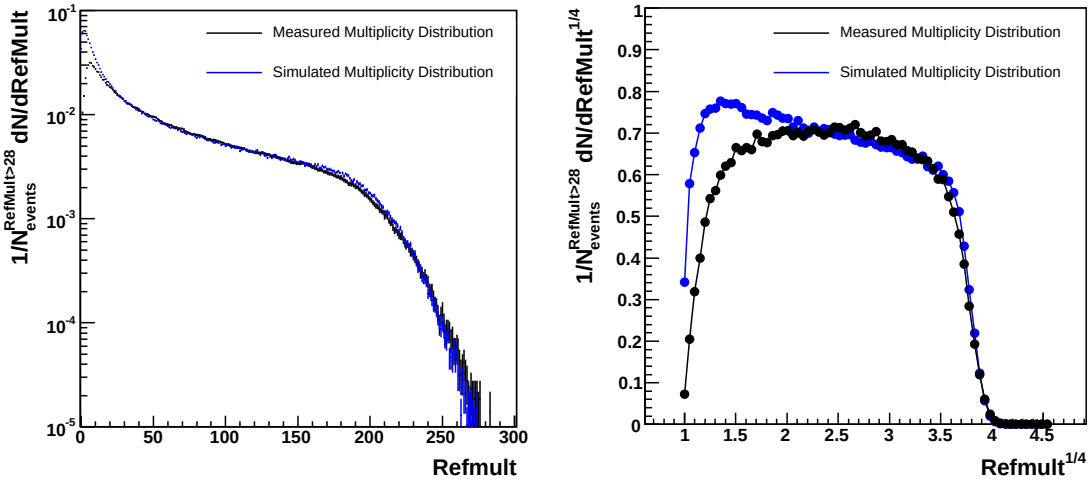

Figure 4.13: Comparison of measured and simulated distributions for Cu+Cu $\sqrt{s_{NN}} = 200$ GeV collisions. Both distributions are normalised by the total number of events with a RefMult > 28. The input parameters for the simulated distribution are $n_{pp} = 2.5$, $x = 0.143$, and $k_{pp} = 2.3$.

Figure 4.13 shows the simulated distribution fitted to the measured distribution with χ^2/DOF being minimised in the RefMult > 28 range. The fit range and normalisation term (see caption) were chosen as the vertex finding efficiency is expected to distort the measured distribution for the lower multiplicities as shown in figure 4.8. For the fitting routine, k_{pp} was fixed at 2.3, n_{pp} was allowed to vary within the experimental uncertainty, and x was a free parameter. The χ^2/DOF reported for the values in figure 4.13 was 1.3 demonstrating that the simulation adequately describes the measured distribution for the range in question. The departure occurs at

RefMult$\sim$16, RefMult$^{1/4} \sim 2$ which is exactly where section 4.3 reported the vertex finding inefficiency to be significant. The ratio of integrals gives a combined vertex finding and trigger efficiency of 0.834. As also shown in section 4.3, the vertex finding efficiency for the pile-up cuts used (see figure 4.12) is 0.924 which in turn implies a trigger efficiency of 0.90 for Cu+Cu $\sqrt{s_{NN}} = 200$ GeV collisions with the ZDC based trigger setup used. The set-up required both ZDCs to register a coincidence with a valid timing signal without an online z cut.

4.4.3 Centrality Definitions

Using the simulated distribution shown in the previous sub section (normalised by the total number of MC Glauber events), table 4.1 shows the centrality definitions calculated using equation 2.3.

Centrality	Reference Multiplicity
0-10%	>=139
0-20%	>=98
0-30%	>=67
0-40%	>=46
0-50%	>=30
0-60%	>=19

Table 4.1: Reference multiplicity (uncorrected) definitions for Cu+Cu $\sqrt{s_{NN}} = 200$ GeV collisions. The efficiency corrected definitions were initially obtained, and then equation 4.8 was used to determine the uncorrected values shown above.

In principle, centrality definitions beyond 0-60% could be calculated. For example, the 0-70% bin corresponds to an uncorrected RefMult $\geq$11. However, as showed in the previous sections, although pile-up can be dealt with effectively for events with RefMult $\lesssim$ 17, the vertex/trigger inefficiencies lead to the measured event sample becoming biased towards events with RefMult $\rightarrow$ 17 relative to the simulated distribution. This in turn makes analysis with these events problematic without additional corrections.

4.4.4 $\langle N_{part} \rangle$ and $\langle N_{bin} \rangle$ Systematic Uncertainties

For the cuts calculated in previous section and shown in table 4.1, the mean values of N_{part} and N_{bin} from the simulated multiplicity distribution in section 4.4.2 are shown in table 4.2. For this given Refmult cut set, systematic variations in $\langle N_{part} \rangle$ and $\langle N_{bin} \rangle$ may arise from:

- Variation of Monte Carlo Glauber parameters c, z, and σ_{NN} within experimental uncertainties
- Variation of n_{pp} within experimental uncertainty
- Variation of negative binomial k_{pp}

To investigate the first point, the Monte Carlo Glauber calculation was rerun with two other profiles. The dilute profile corresponded to $c = 4.195 + 0.085$ fm, $z = 0.581 + 0.031$ fm, and $\sigma_{NN} = 41.7 - 1.1$ mb, and thus delivered the lowest N_{part} and N_{bin} values possible within the range of impact parameters sampled. The dense profile corresponded to the exact the opposite where $c = 4.195 - 0.085$ fm, $z = 0.581 - 0.031$ fm, and $\sigma_{NN} = 41.7 + 1.1$ mb. For each profile, a refit was performed to the measured distribution with n_{pp} being fixed to 2.5, and k_{pp} fixed to 2.3. The dilute and dense profiles lead to the χ^2/DOF being ~ 1.3 for each case with Kharzeev-Nardi x being 0.158 and 0.118 respectively. The dilute profile gave $\langle N_{part} \rangle$ values $\sim 1\%$ lower (all centralities), and $\langle N_{bin} \rangle$ values $\sim 4\% - 7\%$ lower (peripheral $\rightarrow$ central). The converse was found to be true for the dense profile. Regarding the second point, for the simulated distribution in section 4.4.2 the fit reported a negative correlation between x and n_{pp}. n_{pp}=2.48-0.06 gave an x of 0.155 and $n_{pp} = 2.48 + 0.06$ gave an $x = 0.135$ with χ^2/DOF being again 1.3 for each case. The former set gave $\langle N_{part} \rangle$ values $\sim 2\% - 0.5\%$ (peripheral $\rightarrow$ central) higher, and $\langle N_{bin} \rangle$ values $\sim 2.5\% - 0.5\%$ (peripheral $\rightarrow$ central) higher, while the latter set

gave $\langle N_{part} \rangle$ values $\sim 0.5\% - 0\%$ (peripheral $\rightarrow$ central) lower and $\langle N_{bin} \rangle$ values $\sim 0.5\% - 0\%$ (peripheral $\rightarrow$ central) lower.

Finally, the third point was investigated by fixing n_{pp} to 2.5 and x=0.143, then varying k_{pp} by unity. Although fixing k via $k_{pp} = 2.3$ gave a successful starting point in section 4.4.2, the variation in k_{pp} was not constrained to the experimental uncertainties. This is because the Kharzeev-Nardi framework does not specify whether k should be close to the measured value for the p+p multiplicity distribution when using the negative binomial to model multiplicity fluctuation. $k_{pp} = 2.3 - 1$ gave $\langle N_{part} \rangle$ values $\sim 0.9 - 0.2\%$ (peripheral $\rightarrow$ central) higher, and $\langle N_{bin} \rangle$ values $\sim 1.8\% - 0.2\%$ (peripheral $\rightarrow$ central) higher with a χ^2/DOF of ~ 0.8. $k_{pp} = 2.3 + 1$ gave $\langle N_{part} \rangle$ values $\sim 0.2\%$ (all centralities) lower, and $\langle N_{bin} \rangle$ values $\sim 0.4\%$ (all centralities) lower with a χ^2/DOF of ~ 2. Although varying k_{pp} by unity may seem somewhat arbitrary, increases beyond unity led to higher χ^2/DOF values in both cases, and it should be also noted that the variations in $\langle N_{part} \rangle$ and $\langle N_{bin} \rangle$ were smaller compared to varying the Monte Carlo Glauber parameters or varying n_{pp}. Table 4.2 shows the result of adding all the differences in quadrature to give the total systematic uncertainties.

Centrality	$\langle N_{part} \rangle$	$\langle N_{bin} \rangle$
0-10%	$99.00 \pm^{1.47}_{1.22} (\pm^{1.48}_{1.23})$	$188.75 \pm^{15.40}_{13.40} (\pm^{8.16}_{7.10})$
10-20%	$74.55 \pm^{1.26}_{1.04} (\pm^{1.68}_{1.39})$	$123.63 \pm^{9.40}_{8.28} (\pm^{7.60}_{6.70})$
20-30%	$53.67 \pm^{0.99}_{0.68} (\pm^{1.84}_{1.26})$	$77.64 \pm^{5.44}_{4.72} (\pm^{7.01}_{6.08})$
30-40%	$37.75 \pm^{0.66}_{0.54} (\pm^{1.75}_{1.43})$	$47.66 \pm^{2.84}_{2.66} (\pm^{5.96}_{5.59})$
40-50%	$26.24 \pm^{0.54}_{0.35} (\pm^{2.06}_{1.34})$	$29.15 \pm^{1.64}_{1.44} (\pm^{5.63}_{4.93})$
50-60%	$17.23 \pm^{0.41}_{0.20} (\pm^{2.38}_{1.15})$	$16.82 \pm^{0.86}_{0.69} (\pm^{5.14}_{4.13})$

Table 4.2: $\langle N_{part} \rangle$ and $\langle N_{bin} \rangle$ as a function of centrality in Cu+Cu $\sqrt{s_{NN}} = 200$ GeV collisions. Numbers in brackets are the percentile uncertainties.

Chapter 5

V0 ANALYSIS

A V0 is characterised by an electrically neutral particle decaying into two oppositely charged particles, which will bend in opposite directions in the presence of a magnetic field. Unlike the charge neutral parent, the charged daughters may be detected with the TPC. The Λ, $\bar{\Lambda}$, and K^0_S V0s relevant to this analysis, most commonly weak decay via the following modes (percentages denote the branching ratios) [7]:

$$\Lambda \rightarrow p^+ + \pi^-(62.4\%) \tag{5.1}$$

$$\bar{\Lambda} \rightarrow p^- + \pi^+(62.4\%) \tag{5.2}$$

$$K^0_S \rightarrow \pi^+ + \pi^-(69.2\%) \tag{5.3}$$

This chapter will outline the methods used to extracted Λ, $\bar{\Lambda}$, and K^0_S yields as a function of p_T and centrality from Cu+Cu $\sqrt{s_{NN}} = 200$ GeV collisions. Firstly, background reduction and raw signal extraction will be described, and this will be followed by the methods used to correct the raw yields for V0 detection inefficiencies. For the Λ, $\bar{\Lambda}$ particles, the secondary yield contribution from Ξ weak decays will then be determined, and the chapter will finish with systematic uncertainty determination[1].

[1]Tracking for the V0s in this thesis used TPC hits only.

5.1 V0 Finding

For a given event, V0 finding starts with identification of all possible pairs of oppositely charged global tracks[2]. Prior to this information being written into the MuDst data file, default cuts are imposed on various topologies in order to reduce background from random track crossings. Figure 5.1 shows the topology of a V0, and the corresponding default cuts are in table 5.1. These will be explained as follows. Firstly, as most primary track crossings occur close to the primary vertex, the decay

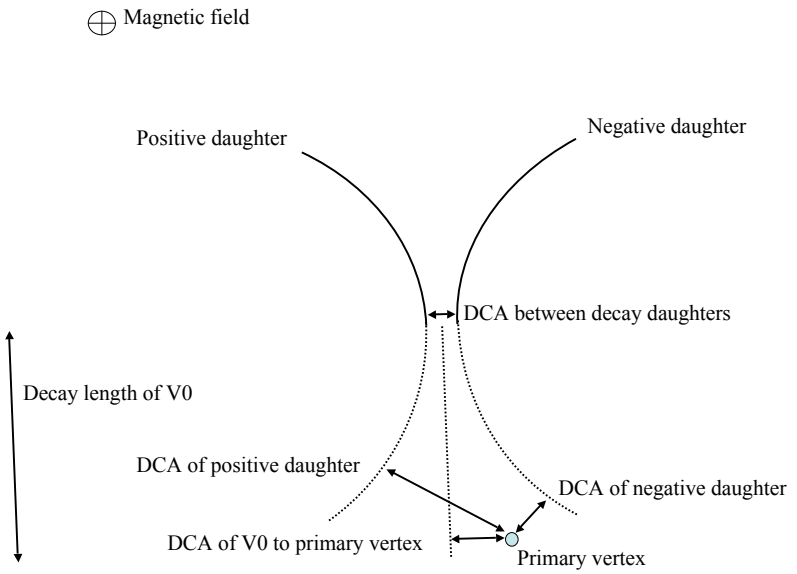

Figure 5.1: The decay topology of a V0. DCA is an acronym for distance of closest approach.

length cut of 2 cm will reject these. The cuts on the distance of closest approach of the V0 daughters, and the distance of closest approach of the V0 to the primary vertex, reflect the fact that background V0s are expected to have larger values of both

[2]V0 finding uses the standard STAR software [99]

variables compared real V0s. In principle, both these cuts should be zero, however the finite TPC spatial resolution leads to the requirement of a finite cut. Finally, as illustrated in figure 5.1, the decay kinematics result in the V0 daughters typically pointing away from the vertex. As this will be in contrast to primary tracks, cuts on the distance of closest approach of the daughters to the primary vertex should again reject random track crossings. At higher p_T, theses cuts are loosened as the V0 tracks are more straight which in turn leads to them pointing more towards the vertex.

Topology	V0 $p_T < 3.5$ GeV/c	V0 $p_T \geq 3.5$ GeV/c
Decay Length	> 2 cm	> 2 cm
DCA of V0 Daughters	< 0.8 cm	< 0.8 cm
DCA of V0 to PV	< 0.8 cm	< 0.8 cm
DCA of Pos Daug to PV	> 0.45 cm	> 0 cm
DCA of Neg Daug to PV	> 0.45 cm	> 0 cm

Table 5.1: Default cuts used in V0 finding for Cu+Cu $\sqrt{s_{NN}} = 200$ GeV collisions. p_T refers to that of the V0. Pos is an abbreviation for Positive, Neg is Negative, Daug is Daughter, PV is Primary Vertex, and DCA is Distance of Closest Approach. The conditions apply to V0 the candidates retained.

To enable particle identification, the Λ, $\bar{\Lambda}$, and K^0_S invariant mass hypotheses can be applied to each V0 candidate. The calculation of the Λ invariant mass is shown in the following equation:

$$M_\Lambda = M_p + M_\pi + 2(E_p E_\pi - \vec{p_p} \cdot \vec{p_\pi}) \tag{5.4}$$

where M is the particle rest mass, E is the particle energy and p is the particle momentum vector. The momentum terms are the measured values for the positive and negative track, the energy terms are calculated assuming the positive track is a proton and the negative track is a pion. The equation arises out of the assumption of momentum and energy conservation. Similar calculations are made for the $\bar{\Lambda}$, and K^0_S invariant mass hypotheses. Figure 5.2 shows each invariant mass for a set

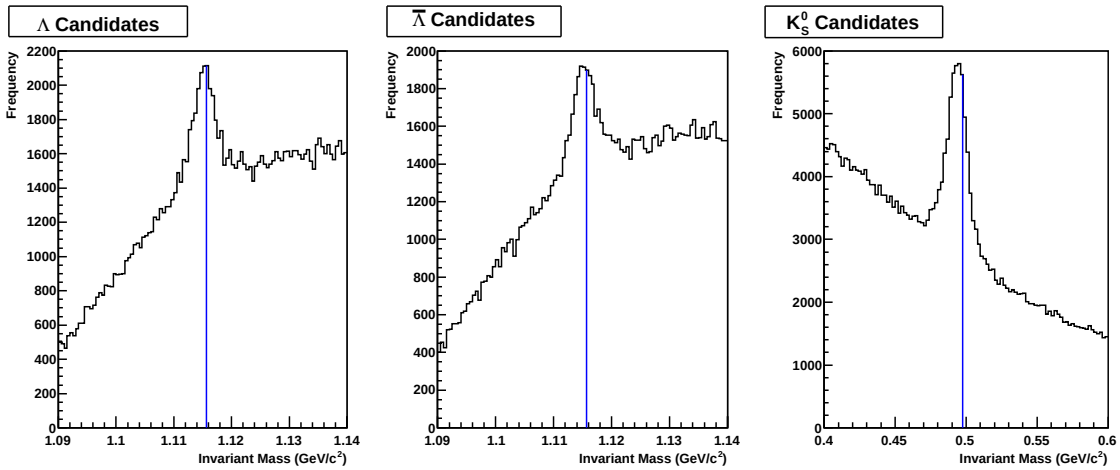

Figure 5.2: Invariant mass distributions for Λ, $\bar{\Lambda}$, and K^0_S candidates from Cu+Cu $\sqrt{s_{NN}} = 200$ GeV collisions.

of V0 candidates subject to the default cuts. In each case, there is clear signal around the expected mass of each particle. The width of the peak is due to the finite momentum resolution of the TPC (natural width is of the order keV). The apparent left shift of the peak relative to the expected mass is due to energy loss of the daughter tracks lowering their respective momentum and energy as they interact with the detector. This in turn lowers the calculated invariant mass as energy and momentum conversation are not quite met when just considering the V0 decay products. Particularly for the Λ and $\bar{\Lambda}$ candidates, the signal to background ratios are still quite low, thus the background needs to be reduced further. Details of the methods used will be described in the following section.

5.2 Background Rejection

Broadly speaking, the aims of further background rejection are three fold. Firstly, high signal to background ratios ensure that the systematic uncertainty with respect to the background is minimal. When the signal is deemed large, this task will take priority so the limiting uncertainty is solely due to the small statistical uncertainty of the signal. Secondly, background reduction can enhance the statistical significance of the signal as the B term in the statistical uncertainty $\sqrt{S+B}$ reduces (S is signal counts and B background counts). When the signal is small, this task will take priority as the dominant uncertainty on the net yield will from the signal strength. Thirdly, where possible, one would like to make the background linear ($y = mx + c$) in the regions adjacent to the peak as this allows a simple parameterisation to describe it.

5.2.1 Energy Loss Cuts

As described in section 3.4.2, the energy loss per unit length, dE/dx, can be used for particle identification. This in turn can be utilised to ensure the daughters of Λ, $\bar{\Lambda}$, and K^0_S candidates correspond to the decay products shown in the chapter introduction. For a given particle p (proton or pion for V0s) set, the following variable transformation gives a Gaussian distribution in z_p centered at zero [118]:

$$z_p = \ln \left[\frac{dE/dx_{(measured)}}{dE/dx_{(expected)}} \right] \tag{5.5}$$

The resolution σ_m of the measured energy loss $dE/dx_{(measured)}$ can be related to $dE/dx_{(measured)}$ by:

$$\frac{\sigma_m}{dE/dx_{(measured)}} = \frac{A}{\sqrt{N}} \tag{5.6}$$

where A is known as fractional resolution for tracks with a single dE/dx point, and N is the number of dE/dx points [119]. The width of the Gaussian z_p can be calculated using $\delta z = \delta x/x$ for $z = \ln(x/u)$ which gives $A/\sqrt{N}$. Dividing a particular value of z_p by the respective Gaussian width of the z_p distribution gives the following relation:

$$N_\sigma = \ln\left[\frac{dE/dx_{(measured)}}{dE/dx_{(expected)}}\right]\frac{\sqrt{N}}{A} \tag{5.7}$$

For a sample of pions, the distribution of N_σ is Gaussian where the area between $\pm 1N_\sigma$ corresponds to 68.3% of the total integral, $\pm 2N_\sigma$ corresponds to 95.4% etc for a pion hypothesis. This same will be true for a proton sample with a proton hypothesis, a kaon sample with a kaon hypothesis etc. If an incorrect particle hypothesis is made (e.g. pion hypothesis for a proton), the magnitude of N_σ will be large providing there is a large difference in the measured and (wrongly) expected dE/dx values. The variable can thus be used to reject background for V0 candidates when the N_σ distributions are well separated for protons, pions, and kaons. Figure 5.3 shows the V0 candidates in figure 5.2 after a $\pm 3N_\sigma$ (99.7%) dE/dx cut on the respective daughters. N_σ for the Λ positive daughter is calculated with the proton hypothesis, the Λ negative daughter is calculated with the pion hypothesis etc.

It is clear that this cut removes a large amount of background with a negligible loss of signal. Pions are the most abundant particles created which leads to random pion crossings dominating the background, therefore the dE/dx cut is most effective for the Λ and $\bar{\Lambda}$ particles as the positive and negative daughters are protons and anti-protons respectively. As indicated in figure 3.7, the main beneficiaries of the dE/dx cuts will be low-p_T V0s as the dE/dx values for pions, kaons and protons merge for higher momentum tracks.

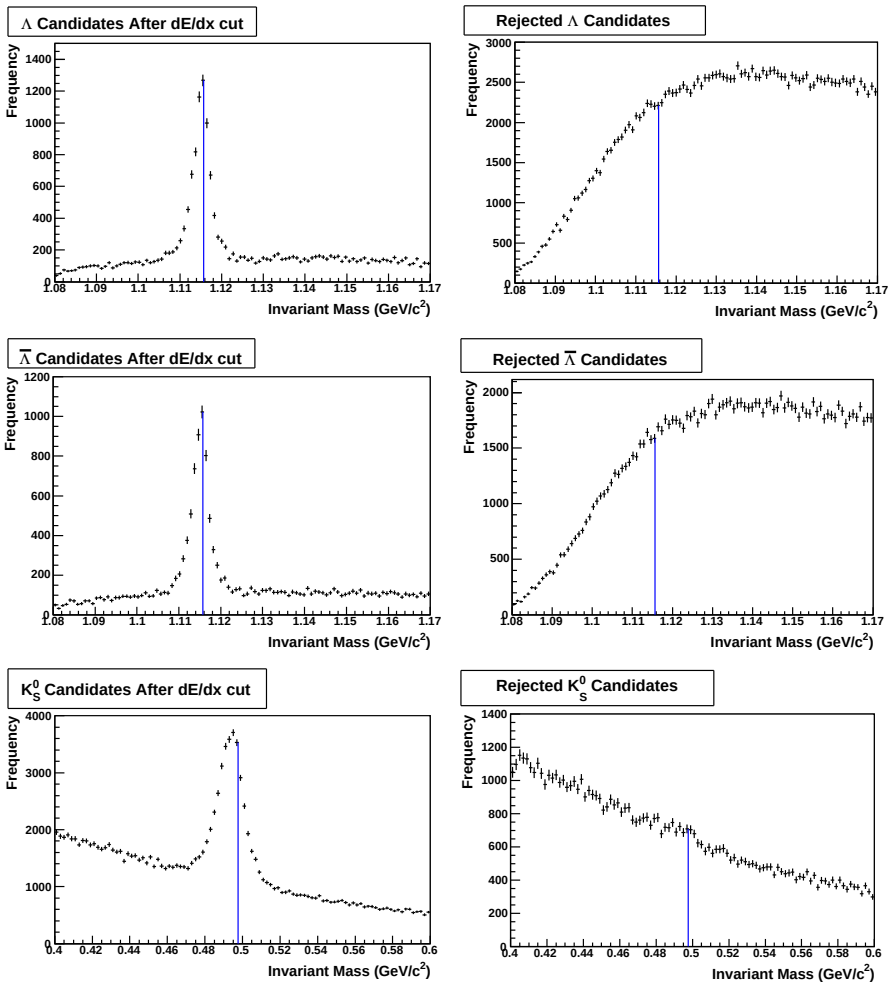

Figure 5.3: The left panels show Λ, $\bar{\Lambda}$, and K^0_S candidates after $3N_\sigma$ dE/dx cuts on their respective daughters. The right panels show rejected candidates. The uncertainties are statistical.

5.2.2 Topological Cuts

For a given topological (e.g. decay length) variable, the V0 signal and background with respect to this variable can be distinguished by plotting the invariant mass against the variable in question. This in turn allows for more precise cuts tuning. Figure 5.4 shows these measurements for Λ candidates after the dE/dx cuts described in the previous sub section have been applied. The top row shows decay length as a function of invariant mass. For all three momentum ranges, the main signal and background regions appear well separated. Furthermore, the signal region

appears to move away from the background with increasing p_T. This is expected as most random crossings will be close to the vertex where the track density is highest, and the mean Λ decay length has a momentum, p, dependance given by $\langle l \rangle = (p/m_0)\tau$ where m_0 is the rest mass of the decaying particle, and τ is the mean lifetime in the particle's rest frame. For the two lowest momentum ranges, a decay length cut of above 5 cm was to chosen to reject the majority of the background in order to optimise the signal to background ratio. For the highest momentum range, the decay length cut was increased to 10 cm so as to optimise statistical significance as the signal starts to become rare at higher p_T.

The second row of panels shows the distance of closest approach of the V0 daughters as a function of invariant mass after the respective decay length cuts. Unlike the decay length correlation, for all three momentum ranges the signal and background regions do not appear well separated so this cut variable was not tightened to remove further background. The third row shows distance of closest approach of the V0 to the primary vertex as a function of invariant mass (after the decay length cut). Again this variable does not provide good separation between the signal and background. However, a finite cut is required to prevent V0s from other pile-up vertices entering the data sample.

Topology	$p_T < 1$ GeV/c	$1 \leq p_T < 4$ GeV/c	$p_T \geq 4$ GeV/c
Decay Length	>5,5,4 cm	>5,5,4 cm	>10,10,9 cm
DCA Daughters	<0.8 cm	<0.8 cm	<0.8 cm
DCA of V0 PV	<0.8 cm	<0.8 cm	<0.8 cm
DCA Pos Daug PV	>1,2.5,2 cm	>0.9,1.1,1 cm	>0.2,0.4,0.3 cm
DCA Neg Daug PV	>2.5,1,2 cm	>1.1,0.9,1 cm	>0.4,0.2,0.3 cm

Table 5.2: Analysis cuts applied to V0s. p_T refers to that of the V0. Black represents all V0s, green Λ, blue $\bar{\Lambda}$, and red K^0_S. Pos is an abbreviation for Positive, Neg is Negative, Daug is Daughter, PV is Primary Vertex, and DCA is Distance of Closest Approach. The conditions apply to V0 the candidates retained.

The fourth row shows the distance of closest approach of the positive daughter to

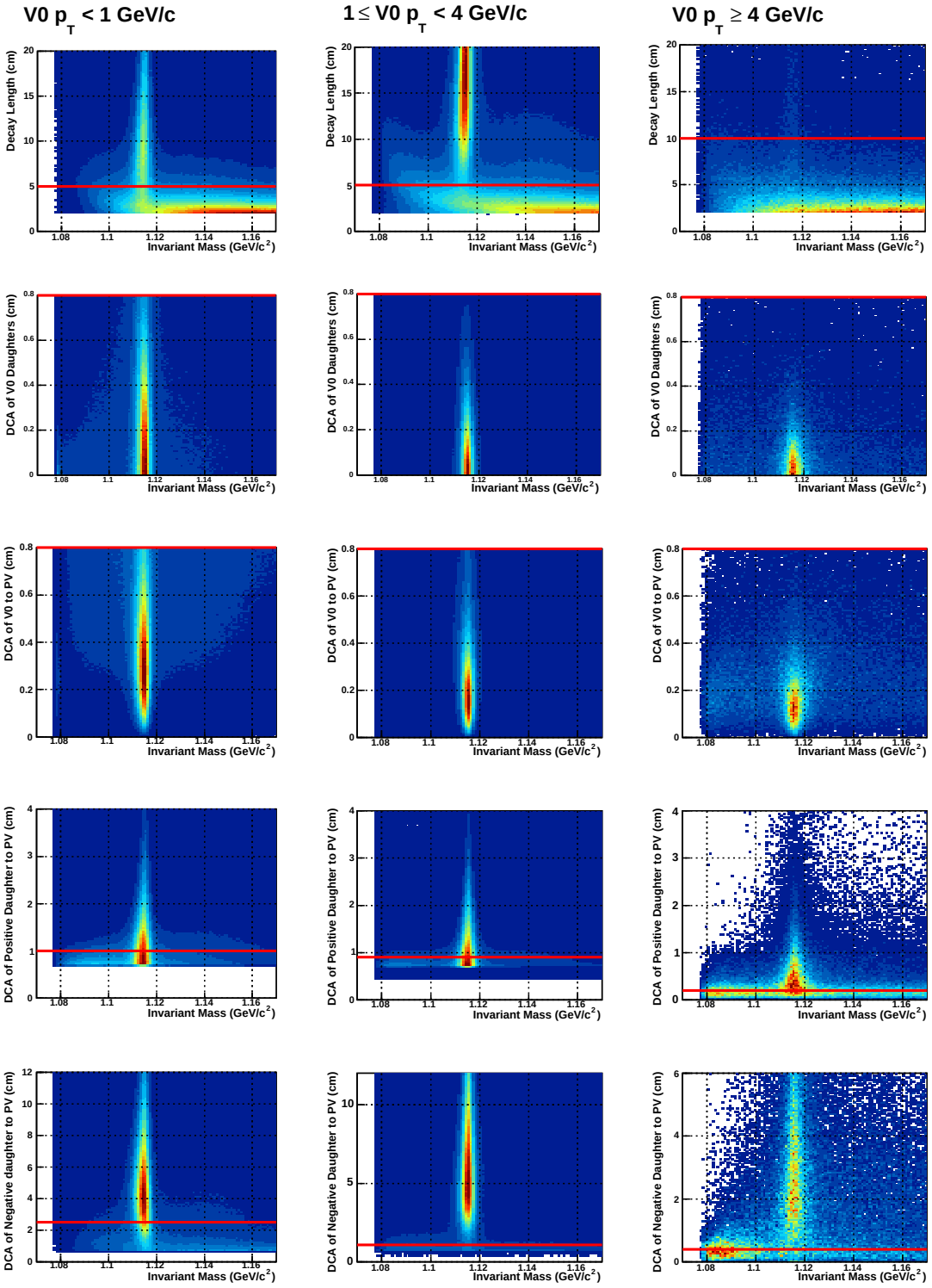

Figure 5.4: Topologies as a function of invariant mass for Λ candidates in three p_T ranges. dE/dx cuts have been applied to both daughters, and lines show the topological cuts in table 5.2. The candidates in a given row are subject to the topological cuts in the preceding row(s).

the primary vertex as a function of invariant mass (after all previous cuts). For all cases, the background appears as a band close to the invariant mass axis so the cut serves to remove these. At higher p_T, the positive daughter tends to point closer to the primary vertex which is the reason for the looser cut. Finally, the fifth row shows the distance of closest approach of the negative daughter to primary vertex as a function of invariant mass (after all previous cuts). Like for the previous row, similar background bands are observed and the chosen cuts reject these. This procedure was repeated for the $\bar{\Lambda}$ and K^0_S candidates, and the final cuts are summarised in table 5.2. The $\bar{\Lambda}$ cuts reflect the fact that the topologies are identical to the Λ topologies upon a swap of the positive and negative daughters. Differences in the K^0_S cuts reflect the fact that the particle has a smaller mean decay length for a given momentum, and the decay is more symmetric with respect to the momentum transfer to the daughters. This gives very similar distance of closest approach of the positive/negative daughter to the primary vertex distributions.

5.2.3 Kinematic Cuts

The two key variables of interest to this sub section are the momentum asymmetry of the V0 daughters, and the rapidity of V0 candidates. The former is given by:

$$\alpha = \frac{p^+_\parallel - p^-_\parallel}{p^+_\parallel + p^-_\parallel} \tag{5.8}$$

where $p_\parallel$ is the parallel momentum component of the daughter with respect to the direction of the parent, and sign indicates the electrical charge of the daughter. The momentum is measured in the lab frame. The magnitude of the momentum component perpendicular to the direction of the parent is known as $p_\perp$, and this is the same for each daughter due to momentum conservation. Together, these are known as the Armenteros-Podolanski variables [120]. The left panel in figure 5.5

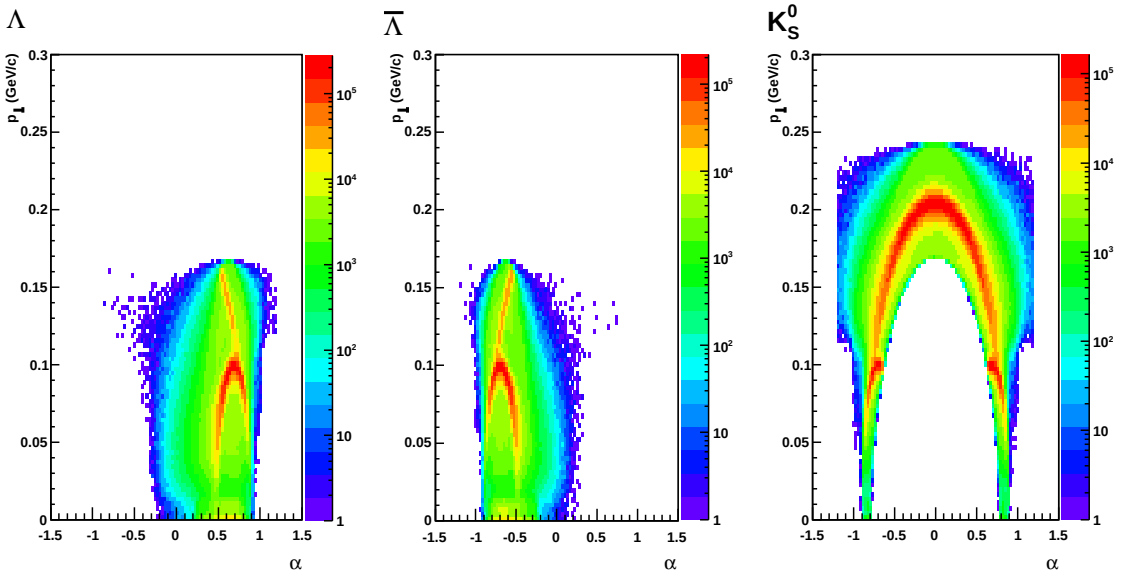

Figure 5.5: Armenteros-Podolanski plot for Λ, $\bar{\Lambda}$, and K^0_S candidates after dE/dx and topological cuts have been applied. Invariant mass cuts of $1.07 < M_\Lambda < 1.17$ GeV/c^2, $1.07 < M_{\bar{\Lambda}} < 1.17$ GeV/c^2, and $0.44 < M_{K^0_S} < 0.56$ GeV/c^2 are applied respectively.

shows $p_\perp$ as a function of α for Λ candidates. The proton typically carries most of the momentum of the parent, thus the Λ signal corresponds to the parabola for $\alpha > 0$. For the $\bar{\Lambda}$ particles in the middle panel, the anti-proton carries most of the momentum leading to the parabola residing at $\alpha < 0$. The right panel shows K^0_S candidates. In this case, both the positive and negative pion usually share an equal portion of the parent momenta, and this leads to the parabola centered at $\alpha \sim 0$.

It is clear that K^0_S particles contribute to the Λ and $\bar{\Lambda}$ candidates, and Λ and $\bar{\Lambda}$ particles contribute to the K^0_S candidates. Tighter topological cuts might not necessarily remove the contaminating V0s as this background is likely to have similar topologies as the signal. Instead, the unwanted V0s can be removed by making an invariant mass cut in the mass range of the contaminating particle. Table 5.3 shows which cuts were applied in this respect. It was found that the Λ, $\bar{\Lambda}$ rejection carried out on the K^0_S candidates improved the signal to background ratio and made the background appear more linear over the full p_T range. As for K^0_S exclusion from the

Λ and $\bar{\Lambda}$ candidates, this was also found to improve the signal to background ratio in all p_T ranges for both sets of candidates. However, the background appeared less linear after the rejection, thus this cut was not carried out as the signal to background ratios were already quite high (as will be shown in figure 5.7).

Kinematic	$p_T < 1$ GeV/c	$1 \leq p_T < 4$ GeV/c	$p_T \geq 4$ GeV/c
Invariant Mass Rejection	None, None, $\Lambda\bar{\Lambda}$	None, None, $\Lambda\bar{\Lambda}$	None, None, $\Lambda\bar{\Lambda}$
$\|y\|$	< 0.5	< 0.5	< 0.5

Table 5.3: Kinematic restrictions placed on V0 candidates. y is rapidity. Black represents all V0s, green Λ, blue $\bar{\Lambda}$, and red K^0_S. The Λ and $\bar{\Lambda}$ invariant mass region rejected is $1.1 \rightarrow 1.14$ GeV/c^2. The conditions apply to V0 candidates retained.

Figure 5.6 shows the rapidity as a function of invariant mass for the Λ, $\bar{\Lambda}$, and K^0_S candidates. Although not specfically aimed at reducing background, a rapidity cut was placed in region where the V0 yield was approximately constant; in this case $|y| < 0.5$ for all particles. Furthermore, this cut was also placed on the corrected p+p and Au+Au $\sqrt{s_{NN}} = 200$ GeV mid-rapidity V0 yields [28, 30]. PHOBOS have shown that charged hadron production per pseudo rapidity unit is constant in the $-2 < \eta < 2$ range for Cu+Cu $\sqrt{s_{NN}} = 200$ GeV collisions [116]. Assuming this also applies to strange hadrons with respect to rapidity, the reduction in yields beyond the $|y| > 0.5$ region is probably due to declining detector acceptance.

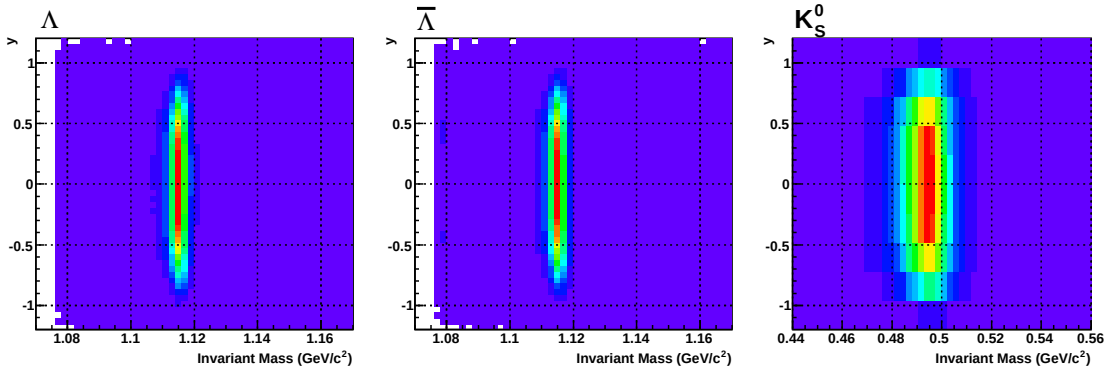

Figure 5.6: Rapidity of Λ, $\bar{\Lambda}$, and K^0_S candidates after dE/dx and topological cuts have been applied.

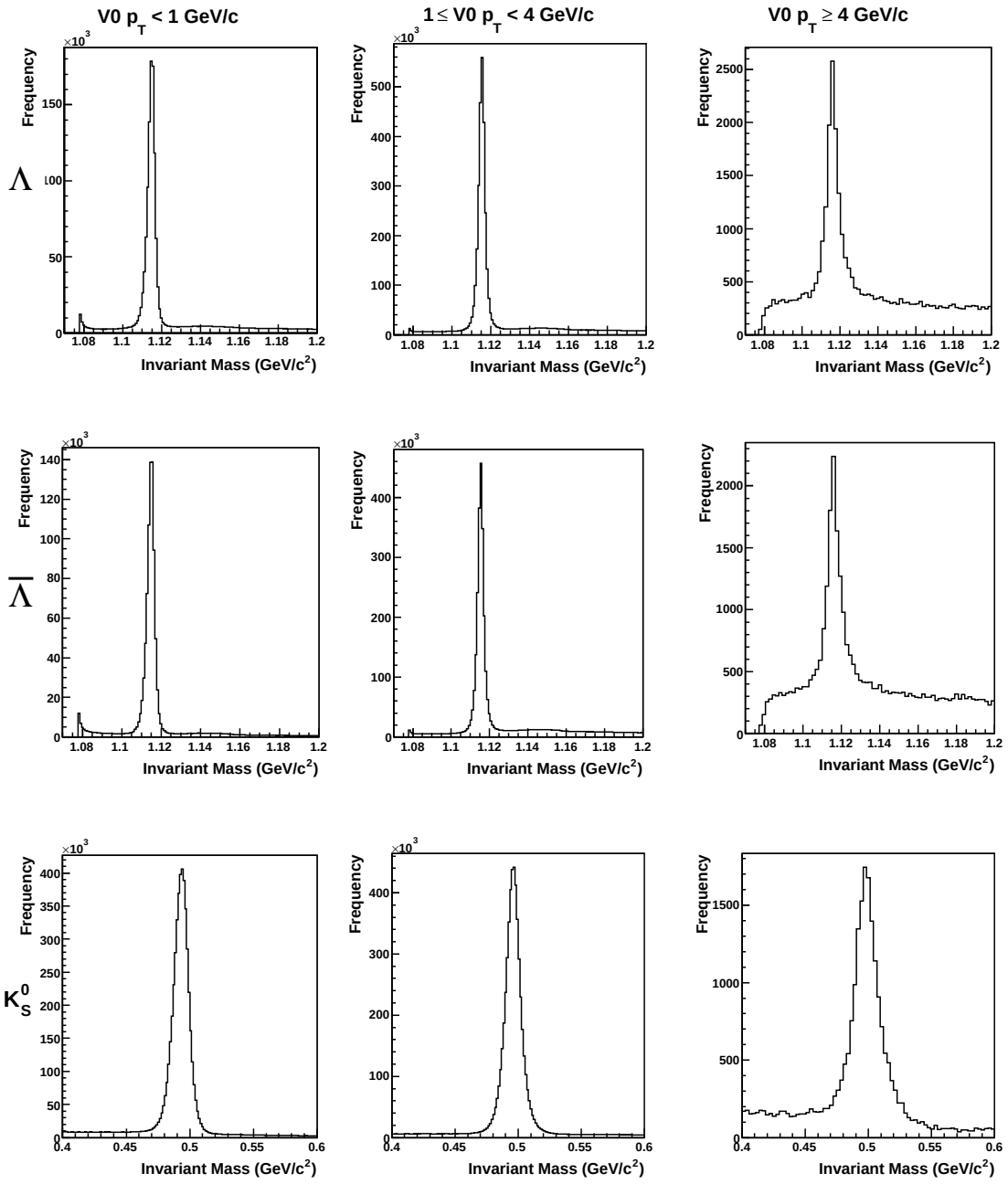

Figure 5.7: Invariant mass distributions for Λ, $\bar{\Lambda}$, and K^0_S candidates after all cuts for Cu+Cu $\sqrt{s_{NN}} = 200$ GeV 0-60% central collisions.

5.2.4 V0 Candidates after all cuts

Figure 5.7 shows the mass peaks after a dE/dx $N_\sigma < 3$ cut is applied on each daughter, and the cuts in tables 5.2 and 5.3 are applied. In addition to those cuts, each daughter is required to have > 15 TPC hits. Previous studies have shown that tracks with smaller numbers of hits often arise from splitting (one charged particle gives two tracks) therefore this cut prevents double counting for the V0s [121, 122]. The event-wise cuts include pile-up rejection and a $|V_z| < 30$ cm cut for the reasons outlined in chapter 4. As with the TPC hit cuts, these cuts were already in place for the V0 candidates shown in the previous section. For V0s within $0 < p_T < 4$ GeV/c range in figure 5.7, the signal completely dominates with the background adjacent to the peaks appearing linear. For the $p_T > 4$ GeV/c range, the signal to background ratios are lower, and this is in part due to looser cuts being placed to preserve the signal. The next section discusses the methods used to calculate the background under the peak region in order to extract the net signal.

5.3 Signal Extraction

They are two ways to determine the background beneath the peak. Firstly, a bin counting method can be employed which involves using the bins adjacent to peak to determine the background. The left panels in figure 5.8 demonstrate this technique on Λ and K^0_S candidates. The invariant mass width of a single red region corresponds to half the width of the blue region, thus this technique is appropriate if the background is linear. The second uses a polynomial fit to the regions adjacent to the peak to determine the background, with the peak region being excluded in the fit[3]. This is shown on the right panels of figure 5.8. Both methods have their advantages and disadvantages. The bin counting method can be used for invariant

[3]All fits performed in this thesis use the CERN MINUIT routine to minimise χ^2 [103]

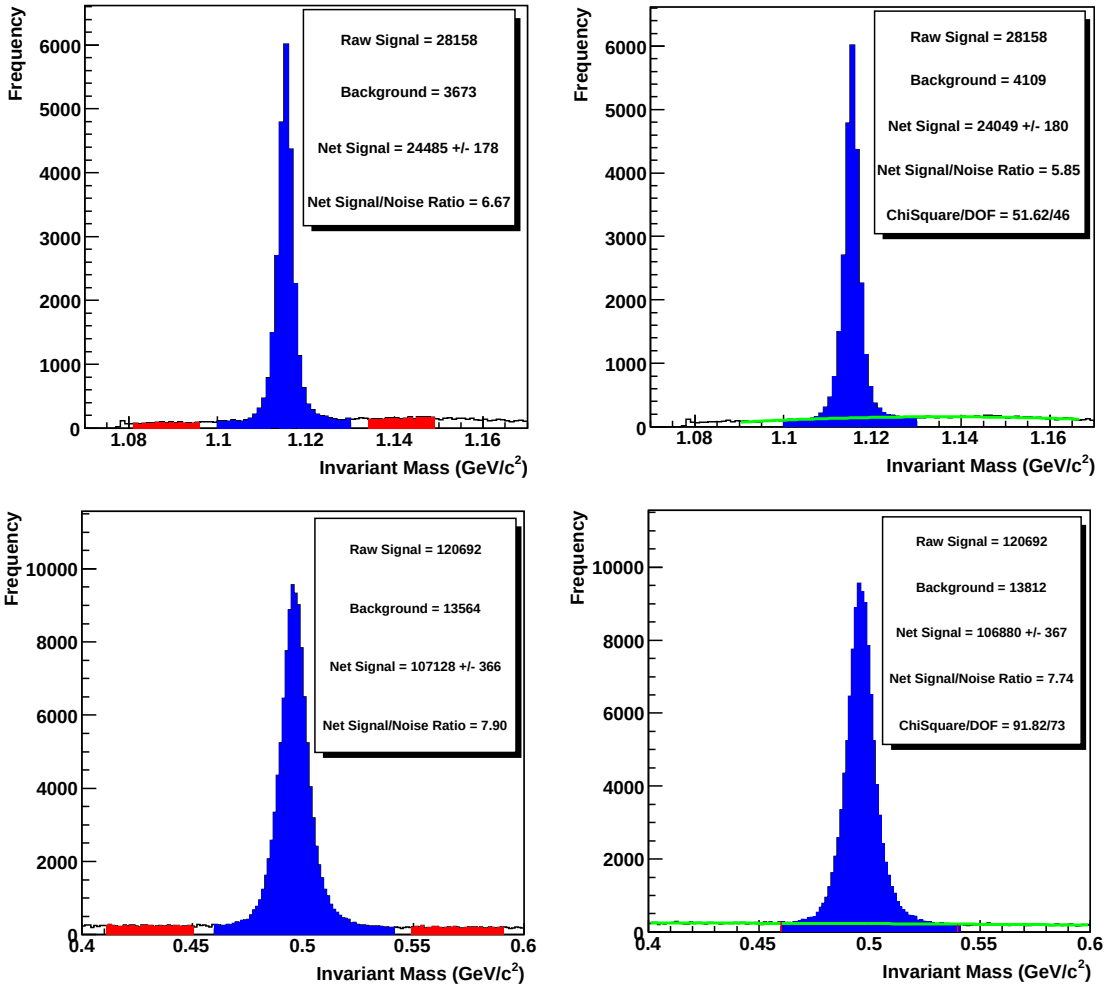

Figure 5.8: A demonstration of bin counting (left panels) and a 2$^{\text{nd}}$ order polynomial fit (right panels) being used to determine the background (thus net signal) for Λ (top panels) and K^0_S (bottom panels) candidates after all cuts.

mass peaks where the statistics are small; polynomial fits will often fail or become unreliable for this case. For this reason, bin counting is the preferred option if the background is deemed linear. However, when this is not the case, the polynomial fit has the advantage of being able to accommodate many non-linear backgrounds. The left panel of figure 5.9 compares both methods for Λ, $\bar{\Lambda}$, and K^0_S candidates. Central collisions (0-10%) were chosen as the signal to background ratio for a given p_T is lowest, i.e is the worst case scenario.

For the $p_T < 1$ GeV/c range, there is a small difference ($\sim 0.5\%$) for the K^0_S

yields which implies the background is (or is very close to being) linear. The bin counting method will thus be chosen to determine the raw yields. Regarding the Λ, $\bar{\Lambda}$ particles, this is not the case for the lowest bin, and is the result of background rising prior to the peak and flattening off afterwards. The polynomial fit follows suit, and thus offers a more precise determination of the background. For the $1 \leq$

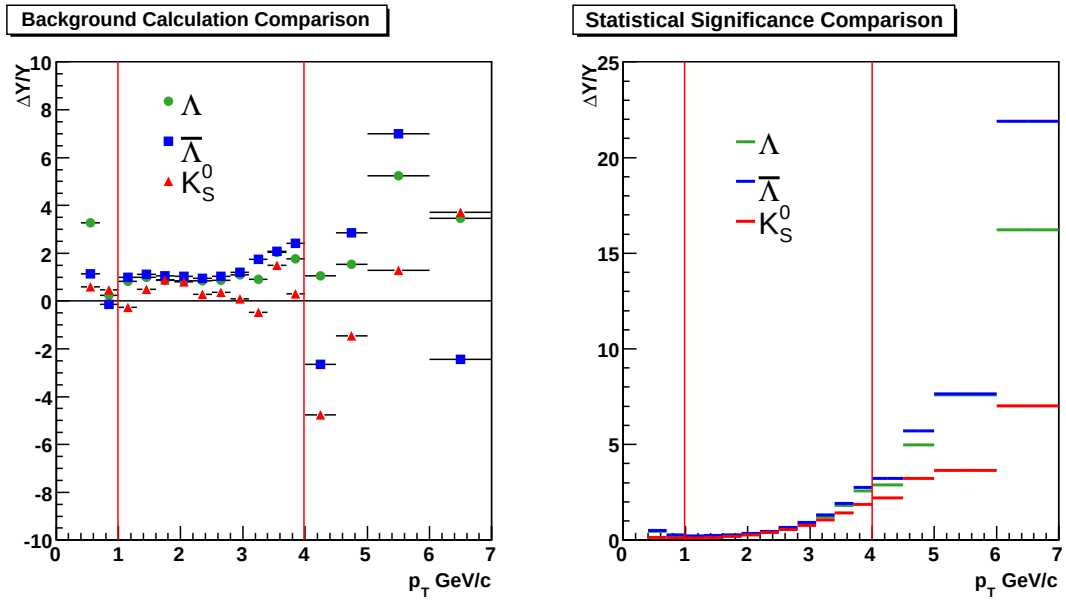

Figure 5.9: Left Panel: The p_T dependance of net yield differences, ΔY, between when the bin counting and a 2$^{\text{nd}}$ order polynomial fit techniques are employed. Y is the mean yield from methods. Right Panel: Fractional statistical uncertainty as a function of p_T where the bin counting method is used to extract the raw yield. For both panels, the red lines show where the topological cuts change.

$p_T < 4$ GeV/c range, again the fluctuating differences for K^0_S the yields are 0.5% $\rightarrow$ 1%, thus the bin counting method will be used. The situation is slightly different for Λ, $\bar{\Lambda}$ candidates; the bin counting method always gives higher yields than the polynomial fit especially near $p_T \sim 4$ GeV/c. Again, this is due to the rising and flattening background, thus the polynomial fit will be used. Finally, for the $p_T \geq 4$ GeV/c range, the differences in yield start to become volatile for all particles. The lower signal to noise ratios (illustrated in right panels of figure 5.7), and decreasing statistical significance shown in the right panel of figure 5.9, lead to the background

fits becoming unreliable. However, when a linear fit is carried out in the bin counting region on the distributions in the right panels of figure 5.7, the χ^2/DOF for the all particles varies from 0.6-1.5, which suggests that a linear function is a good approximation. Thus the bin counting method is used to determine raw yields for all particles. Compared to the previous p_T range, the topological cuts are looser for this range, and this illustrates how the shape of the background is affected by these for the Λ and $\bar{\Lambda}$ candidates.

5.4 Corrections to Raw Spectra

In each p_T bin, the raw V0 yields calculated in the previous section does not represent a total count of all the particles created in the rapidity range ($|y| < 0.5$) chosen. This is due to a partial V0 detection efficiency which depends on two things:

- Probability of a V0 entering detector acceptance
- Reconstruction efficiency of a V0 within detector acceptance

Regarding the first point, as mentioned in section 3.4, tracks below a certain momentum (which depends on the magnetic field magnitude) will not enter the active TPC region. In case of V0s, one or both daughters may fail to reach the TPC. The acceptance is also limited by the spaces between sectors; some of the straight high-p_T tracks will travel parallel to these thereby avoiding detection. The second point arises from the finite track reconstruction efficiency, and the cuts placed on V0 candidates. These will include the topological and kinematic cuts described previously. Examples of signal loss due to these cuts can be viewed in various panels in figure 5.4 which show that Λ signal is also rejected when the cut is applied, and figure 5.5 demonstrates that K^0_S signal will be lost when Λ and $\bar{\Lambda}$ particles are rejected from K^0_S candidates.

In order to determine the V0 detection efficiency, a calculation was performed which embeds simulated V0s into a real event [99, 121]. The process starts by the creation of Monte Carlo V0s using the GENTX program [122], which takes the vertex position and event multiplicity as inputs, and gives V0 momentum vectors as an output. The p_T and rapidity range covers that which is applicable to the measured raw yields. The number of Monte Carlo V0s does not exceed 5% of the event multiplicity so as not to perturb the original event. With the given particle momentum, the propagation of the Monte Carlo V0s (and subsequent daughters) is modelled by the GEANT program which simulates interactions with detector material for the STAR detector setup [123]. This then outputs the resulting number of ionisations created in the TPC along with ionisation x, y, z positions and number of electrons liberated for each ionisation.

The TPC Response Simulator is then used to model the drift of the ionised electrons, charge deposition on the pads via the electron amplification process, and the response of the electronics [124]. The outputs are the ADC values from the Monte Carlo V0 daughters tracks. To ease the complexity, the distortions in drift caused by the items listed in section 3.4 are not reproduced. The number of ionised electrons (thus dE/dx) produced by GEANT is typically lower for embedded tracks compared to real tracks, thus the generated ADC counts are adjusted to match what is typically seen in the real data [125]. These are embedded into the event's real ADC values, then the full hit and track reconstruction (including V0 finding) process is carried out modulo the distortion corrections applied to the hits. After track reconstruction, in order to determine which tracks correspond to the generated Monte Carlo tracks, the following association conditions have to be met:

- A reconstructed hit is associated to a GEANT hit if the distance between them is below 5 mm. These are known as *common hits*. The finite distance is due to the simulated diffusion of the drifting element.

- A reconstructed track is associated to the Monte Carlo track if the number of common hits is above 3.
- V0 association requires both daughters to be associated with the respective Monte Carlo V0

Finally, the whole process is repeated for many different events as the V0 detection efficiency may vary as a function of varying TPC occupancy. Previous studies have shown that this drops by a factor of 2 from peripheral to central Au+Au events where V0 reconstruction becomes more challenging [84, 126]. Figure 5.10 shows generated and reconstructed Monte Carlo V0s for central Cu+Cu collisions as a function of p_T. The jumps in the number of reconstructed V0s demonstrate the effect of looser topological cuts. The correction is defined as follows:

$$C(p_T, y, M) = \frac{N_R(p_T, y, M)}{N_G(p_T, y, M)} \times BR \tag{5.9}$$

where N_R is the number of reconstructed Monte Carlo V0s subject to the analysis topological/kinematic cuts, N_G is the number of generated V0s, and M is the reference multiplicity. BR is the particle (Λ, $\bar{\Lambda}$ or K^0_S) branching ratio; as the daughter particles from only one decay channel are generated, this factor enables the total particle yield to be presented when the raw yields are divided by the correction. Prior to this calculation, one more thing has to be considered. N_G is flat as a function of p_T in figure 5.10 and this is in contrast to the rising/falling corrected particle yields typically observed in the data. The next section describes how this is accounted for.

5.4.1 Re-weighting Procedure

There are two ways in which the physical p_T distribution should influence the derived correction shown in equation 5.9. The first effect arises from a finite p_T *resolution*.

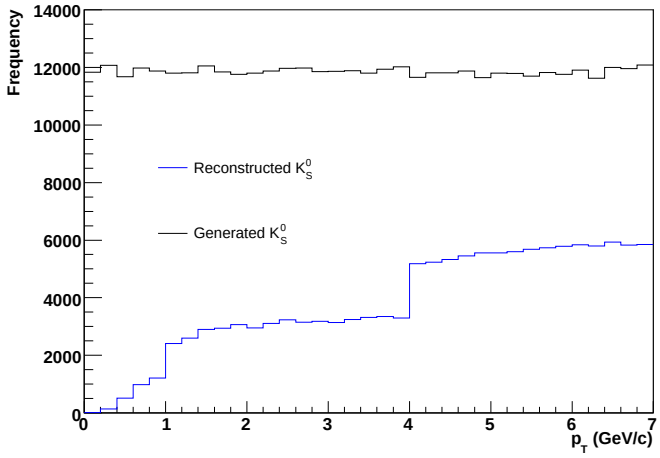

Figure 5.10: Generated and reconstructed Monte Carlo K^0_S particles as a function of p_T for central Cu+Cu $\sqrt{s_{NN}} = 200$ GeV collisions. The reconstructed K^0_S particles are subject to the analysis cuts in section 5.2 bar the dE/dx cut.

For a particular raw yield bin, there will be a number of V0s counted whose actual p_T is outside the bin range due to resolution effects on the reconstructed p_T. Conversely, there will be other V0s whose actual p_T is within the raw bin's range, however the reconstructed p_T is outside. Such behaviour may be different when the underlying p_T is physical (rising/falling) compared to flat therefore the correction needs to mimic the later case. The second effect arises from a *finite bin width* in the context of changing correction across the bin range. If the underlying physical p_T distribution and underlying correction change significantly within the bin range, the correction needs to be biased towards the region in p_T with the most V0s, which may not happen in the flat case. To further complicate things, these two effects may not be exclusive, and thus have to be accounted for by a *re-weighting correction* which will modify the correction in equation 5.9 accordingly.

Firstly, this requires the determination of the physical p_T distribution, which can be approximated by applying corrections to the raw yields prior to the re-weighting adjustment. This is approach is valid providing the adjustments in the correction due to the re-weighting are much smaller than the magnitude of the

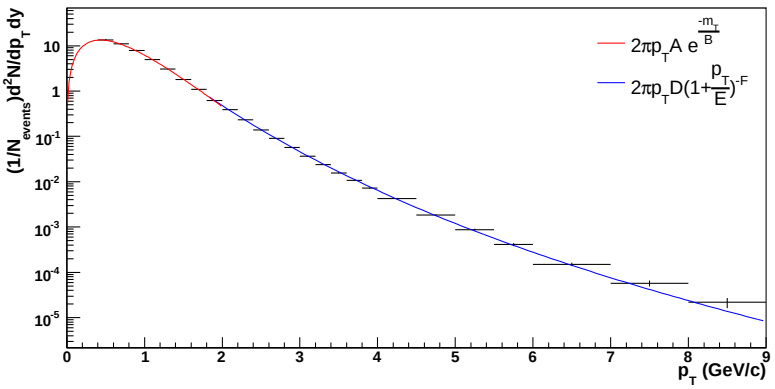

Figure 5.11: Efficiency corrected K^0_S yields from 0-10% central Cu+Cu collisions prior to the re-weighting correction. The red line is an m_T exponential, and the blue line a power-law function. Both parameterisations are fitted to the spectra via a χ^2 minimisation.

correction. For K^0_S particles from central Cu+Cu collisions, the initially corrected yields are shown in figure 5.11. As will become evident later, the parameterisations shown in figure 5.11 are required for the re-weighting procedure, and are physically motivated with the m_T exponential being described in section 2.2.4. The power-law function approximates an m_T exponential at low p_T and becomes $\propto p_T^{-F+1}$ at high p_T which is the expected p_T dependence of particle production when jet fragmentation dominates [81]. As the power-law function did not describe all particles equally well over the whole p_T range ($\chi^2/DOF >> 1$), an m_T exponential is used at very low-p_T as the fits were good ($\chi^2/DOF \sim 1$) for this p_T region. Now the physical p_T distribution has been established, the re-weighting procedure can begin. This starts by creating a 2D histogram for reconstructed Monte Carlo particles of reconstructed p_T, $p_T[reco]$, against generated p_T, $p_T[gen]$. Both $p_T[reco]$ (index denoted by j) and $p_T[gen]$ (index denoted by i) have 100 MeV/c bins which are smaller than raw yield bins that range from 200 to 1000 MeV/c. The histogram format can be viewed in the bottom panels of figure 5.12. For a given $p_T[reco]$ bin, a projection of the $p_T[gen]$ distribution is made. The occupancy of the each $p_T[gen]$ bin, n, is then multiplied

by a corresponding weight, w, which is calculated as follows:

$$w = \frac{f(p_T[gen])}{f(p_T[reco])} \tag{5.10}$$

where $f(p_T)$ is the parameterised p_T distribution appropriate for the $p_T[reco]$ and $p_T[gen]$ values. As observed in figure 5.10, the ratio of the number of generated Monte Carlo particles for $p_T[reco]$ and $p_T[gen]$ bins is ~ 1. However, if the flat p_T distribution was to be replaced by the physical p_T distribution, this ratio would be w. Thus by multiplying n of the $p_T[gen]$ bin by w, the relative occupancies mimic those of the physical p_T distribution. Only $p_T[gen]$ bins within 3 standard deviations with respect to the mean have their occupancies adjusted. For the typically falling p_T distribution, this prevents single occupancy bins with $p_T[gen] \ll p_T[reco]$ gaining abnormally large weights. An example is shown in the top panel of figure 5.12 for four different $p_T[reco]$ bins. The increasing width of the $p_T[gen]$ distribution with increasing $p_T[reco]$, is due to the worsening nominal p_T resolution ($p_T \cdot (\delta p_T/p_T)$). Further inspection shows that for all the $p_T[reco]$ bins, the p_T distribution is falling which leads to $w > 1$ when $p_T[gen] < p_T[reco]$, and $w < 1$ when $p_T[gen] > p_T[reco]$, and this is seen by the blue histograms lying above the red histograms for $p_T[gen] > p_T[reco]$, and vice versa. This can also be viewed in the bottom panels of figure 5.12. The correction for the bin $p_T[reco]$ bin, j, is therefore calculated as follows:

$$c_j = \frac{\sum_i w_i n_i}{n[gen]} \times BR \tag{5.11}$$

where $n[gen]$ is the total number of the Monte Carlo particles generated in the p_T range particular to j, and the sum spans all $p_T[gen]$ bins. To account for the described finite bin width effect, the correction applied to the raw yield bin is calculated

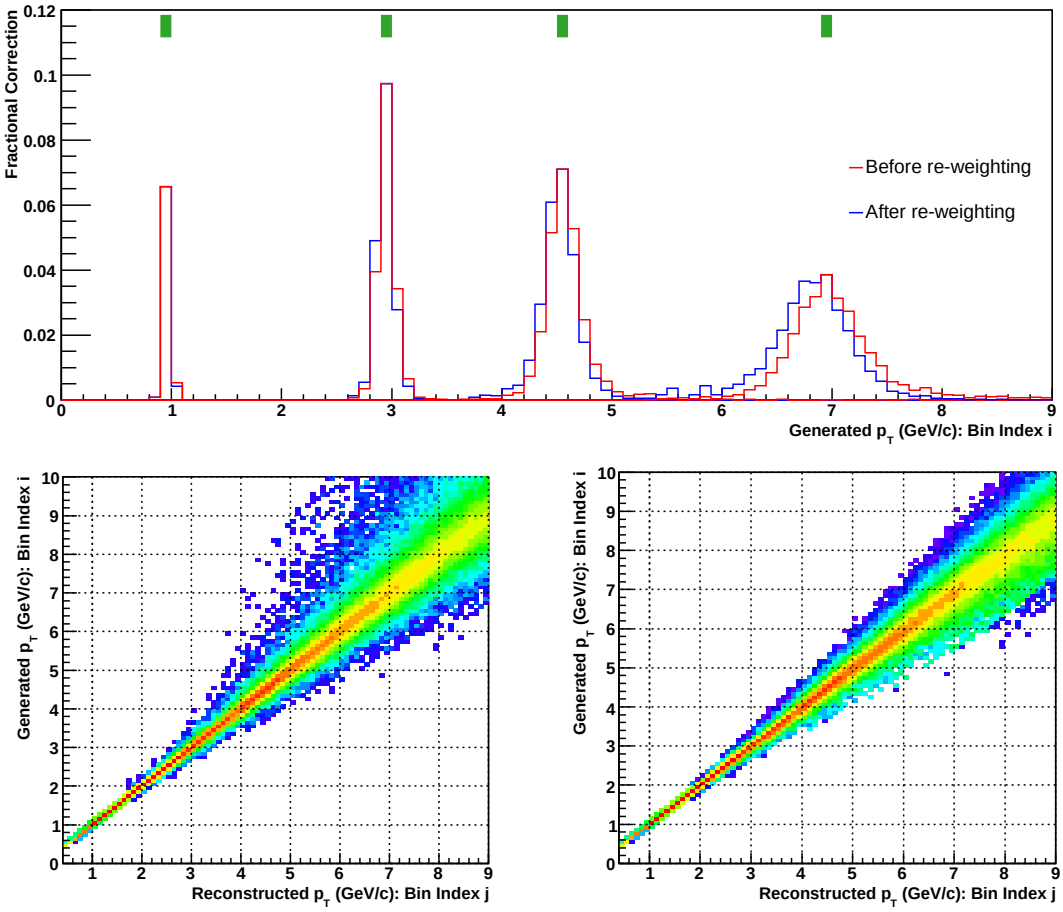

Figure 5.12: Top Panel: Projections of $p_T[gen]$ for four different $p_T[reco]$ bins whose ranges are shown by the green markers, before and after the adjustments determined in equation 5.10. Bottom Panels: Distribution of all $p_T[gen]$ and $p_T[reco]$ bins before (left) and after (right) the re-weighting adjustments determined by equation 5.10.

as a weighted average given by:

$$C_T = \frac{\sum_j w_j c_j}{\sum_j w_j} \tag{5.12}$$

where $w_j = f(p_T)$ which is the parameterised p_T distribution taken at the j bin center. The range of j spans that applicable to the raw yield bin. Again, where the p_T distribution is falling, the weighted average ensures that the corrections with lower j values take precedent. Figure 5.13 shows the effect of the re-weighting correction as a function of p_T. Bar the final bin, the adjustment to the final correction is small.

In the $0 < p_T < 4$ GeV/c range, the ratio decreases and this is accompanied by the nominal values of both corrections flattening. The re-weighting procedure thus appears to have the desired effect. The falling p_T distribution shown in figure 5.11 within context of a rising detection probability leads to the corrections being lowered relative to a flat p_T distribution; this is most severe where corrections rise the most rapidly. For the $4 < p_T < 7$ GeV/c range where the bins widen and the cuts are loosened, the ratios stay above one again in the context of a rising correction. Above 7 GeV/c, the ratio drops below one. This occurs in the context of a falling

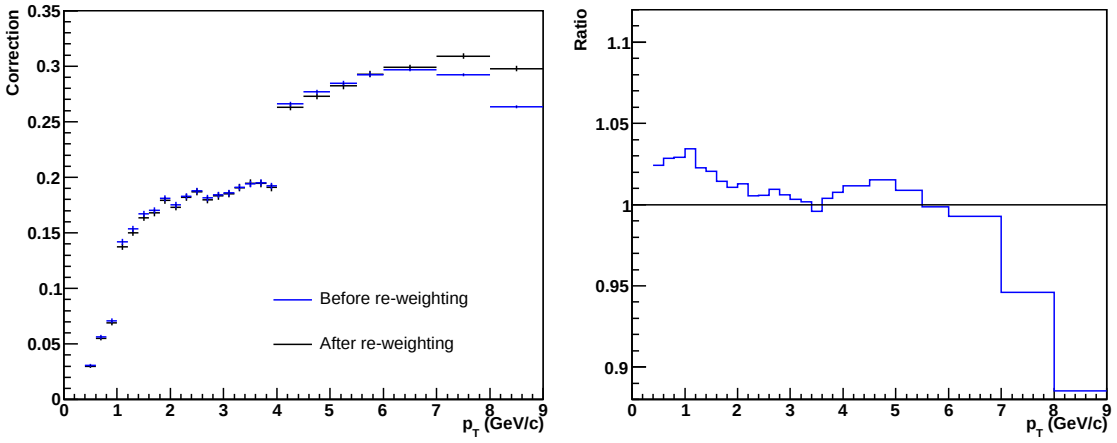

Figure 5.13: Left Panel: Corrections before and after the re-weighting procedure for K^0_S from Cu+Cu 0-10% central collisions. Right Panel: Ratio of both corrections (before/after).

initial correction thereby reversing the role of re-weighting; the bias towards lower p_T particles due to the re-weighting procedure leads to higher corrections. Finally, after the re-weighted corrections are applied to spectra, the parameterisations can be refitted. When the re-weighting procedure was carried out with new fits, there were negligible differences between re-weighted corrections derived in the first and second iteration. Thus only one iteration was deemed required for the corrections shown in the following sub section.

5.4.2 V0 Corrections

Figure 5.14 shows the corrections applied to the Λ, $\bar{\Lambda}$, and K^0_S yields as a function p_T and centrality. These are calculated for the final analysis cuts described in the previous section. Raw yields are divided by the correction values in order to produced corrected yields. The identical behaviour of the Λ and $\bar{\Lambda}$ corrections is due to the reflected daughter topological cuts and distributions. Unlike the case for Au+Au collisions, the Cu+Cu corrections show little centrality dependance. This is due to the smaller differences in multiplicities between peripheral and central Cu+Cu collisions; the corrected yield ($\eta < 0.5$) of charged hadrons varies from ~ 40 to $\sim$ 180 for Cu+Cu 40-60% and Cu+Cu 0-10% collisions respectively, while for Au+Au 60-80% and Au+Au 0-5% collisions, the charged hadron yield varies from ~ 34 to ~ 691 respectively [114].

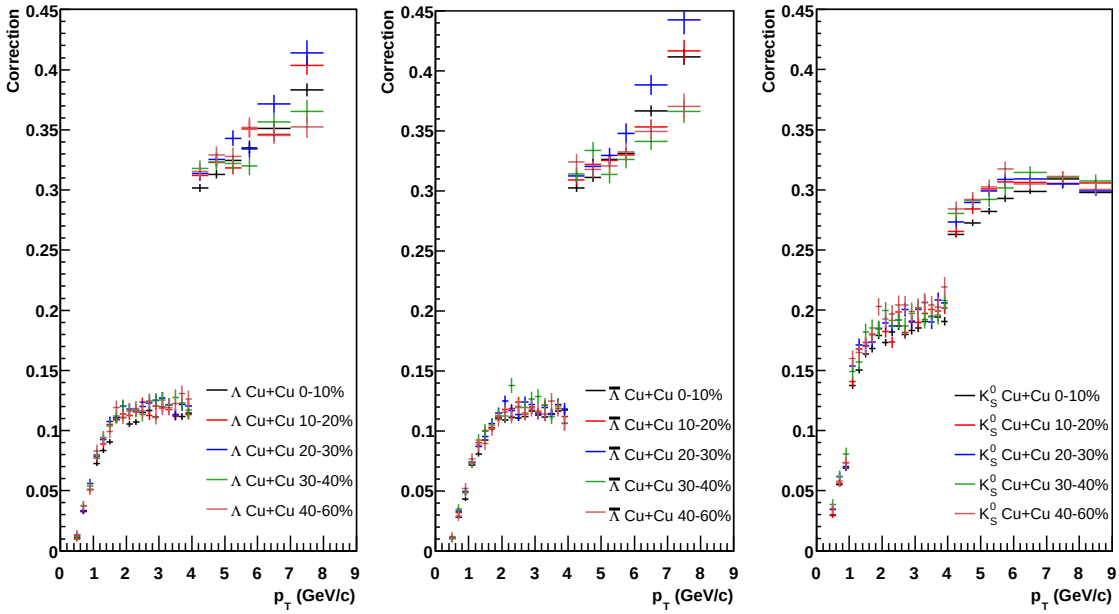

Figure 5.14: V0 corrections for Cu+Cu $\sqrt{s_{NN}}$ = 200 GeV collisions for the cuts described in section 5.2.

In contrast to the centrality dependance, the p_T dependance of the corrections is very pronounced. With increasing p_T, this is due to the increasing probability of acceptance [126], the higher probability of track reconstruction [94], the V0 topological/kinematic distributions changing with p_T (this will be shown in section 5.6), and the topological cuts being successively loosened at 1 and 4 GeV/c. In order to estimate the V0 signal loss due to the topological/kinematic cuts, corrections (acceptance and reconstruction) applied to single tracks can be compared to the V0 corrections. Above $p_T \sim 1$ GeV/c, the single track pion correction at mid-rapidity is constant with a value of ~ 0.8 for Au+Au $\sqrt{s_{NN}} = 200$ GeV collisions with similar multiplicities as Cu+Cu collisions [114]. For the K^0_S particles with their momentum symmetric decay, the square of this multiplied by the branching ratio ($0.8^2 \times 0.69$), corresponds to the expected V0 correction without topological/kinematic cuts which is ~ 0.45 for $p_T \gtrsim 2$ GeV/c. Thus for K^0_S particles with $2 \lesssim p_T < 4$ GeV/c the signal loss due to the cuts is $\sim 55\%$, and for $p_T \geq 4$ GeV/c the signal loss drops to $\sim 34\%$.

5.5 Feed-Down Contribution

The Λ and $\bar{\Lambda}$ raw yields can be divided into two contributions; a primary contribution produced directly from the event vertex region, and a secondary contribution from Ξ and Ω weak decays away from the event vertex region. The later is known as *feed-down*. These secondary contributions were calculated (and subsequently subtracted) for the Au+Au $\sqrt{s_{NN}} = 200$ GeV Λ and $\bar{\Lambda}$ particle yields [51], therefore this analysis will follow suit. The main channels are as follows [7]:

$$\Xi^- \rightarrow \Lambda + \pi^-(99.9\%) \tag{5.13}$$

$$\Xi^0 \rightarrow \Lambda + \pi^0(99.5\%) \tag{5.14}$$

$$\Omega^- \rightarrow \Lambda + K^-(67.8\%) \tag{5.15}$$

$$\bar{\Xi}^+ \rightarrow \bar{\Lambda} + \pi^+(99.9\%) \tag{5.16}$$

$$\bar{\Xi}^0 \rightarrow \bar{\Lambda} + \pi^0(99.5\%) \tag{5.17}$$

$$\bar{\Omega}^+ \rightarrow \bar{\Lambda} + K^+(67.8\%) \tag{5.18}$$

In order to calculate the p_T dependence of the above contributions to the raw Λ and $\bar{\Lambda}$ spectra, firstly, corrected Ξ^- and $\bar{\Xi}^+$ yields are measured for the V0 (from the decay) rapidity region $|y| < 0.5$ which corresponds to that of the raw spectra. Raw Ξ^- and $\bar{\Xi}^+$ candidates are identified by the cascade finder which searches for V0s whose extrapolated path prior to decay is crossed by a charged track known as the *bachelor*. As with the V0s in the previous sections, for a given particle hypothesis the invariant mass is calculated from the bachelor and V0 momenta, topological and kinematic cuts are placed, and the raw signal is extracted as a function of V0 p_T. The raw spectra are corrected using the a Monte Carlo simulation as described in section 5.4. The corrected Ξ^- and $\bar{\Xi}^+$ spectra are shown in figure 5.15, and the details of the cuts, the cascade decay topology, and yield extraction can be found in

appendix A. The secondary Λ and $\bar{\Lambda}$ contribution from the respective Ξ^- and $\bar{\Xi}^+$

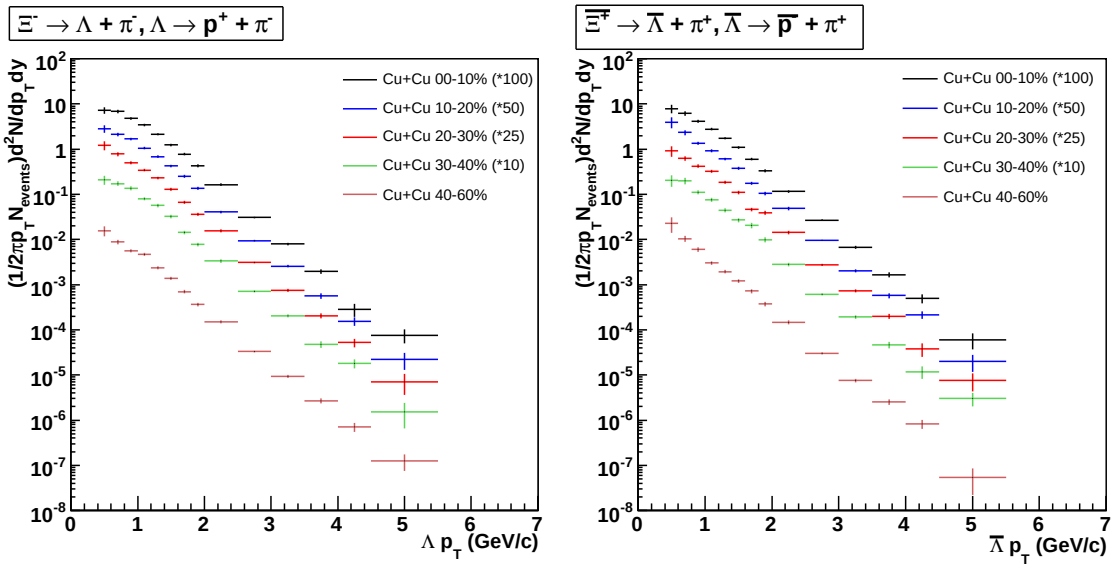

Figure 5.15: Corrected Ξ^- and $\bar{\Xi}^+$ yields as a function of V0 p_T for the V0 rapidity interval $|y| < 0.5$.

decays can now be calculated using the following relation:

$$N_r = \epsilon_s N_c \tag{5.19}$$

where N_r is the number of raw counts per event of secondary Λ or $\bar{\Lambda}$ particles for a particular p_T bin and rapidity bin, ϵ_s is the secondary V0 efficiency, and N_c is the corrected number of Ξ^- or $\bar{\Xi}^+$ particles which yield V0s in the same p_T bin and rapidity bin as N_r. The secondary V0 efficiency is calculated in exactly the same way as the V0 corrections described in section 5.4 with the only differences being that the Monte Carlo V0s originate from the Ξ^- and $\bar{\Xi}^+$ decay vertices rather than the primary vertex, and the respective V0 branching ratios are not applied. The latter is due to the Ξ^- and $\bar{\Xi}^+$ corrected yields only representing the channels shown in figure 5.15, and the subtraction being on the raw yields which is applied in the next chapter. Modulo differences due to the branching ratio, the secondary V0 efficiencies and V0s

corrections may have different values (at a given p_T) due to different topologies (such as V0 decay length) arising from the V0 origins with respect to the primary vertex. As the Ξ^0 and $\bar{\Xi}^0$ particles cannot be reconstructed in the same way, the corrected yields are assumed the same as the Ξ^- and $\bar{\Xi}^+$ particles respectively due to the very similar masses and identical strangeness content. Regarding the secondary V0 efficiency from the Ξ^0 and $\bar{\Xi}^0$ particles, these are also assumed the same as those from the Ξ^- and $\bar{\Xi}^+$ particles respectively, in line with previous observations [61, 126]. This means that the right hand term in equation 5.19 is doubled to determine total the secondary contribution from the charged and neutral Ξ (anti) particles.

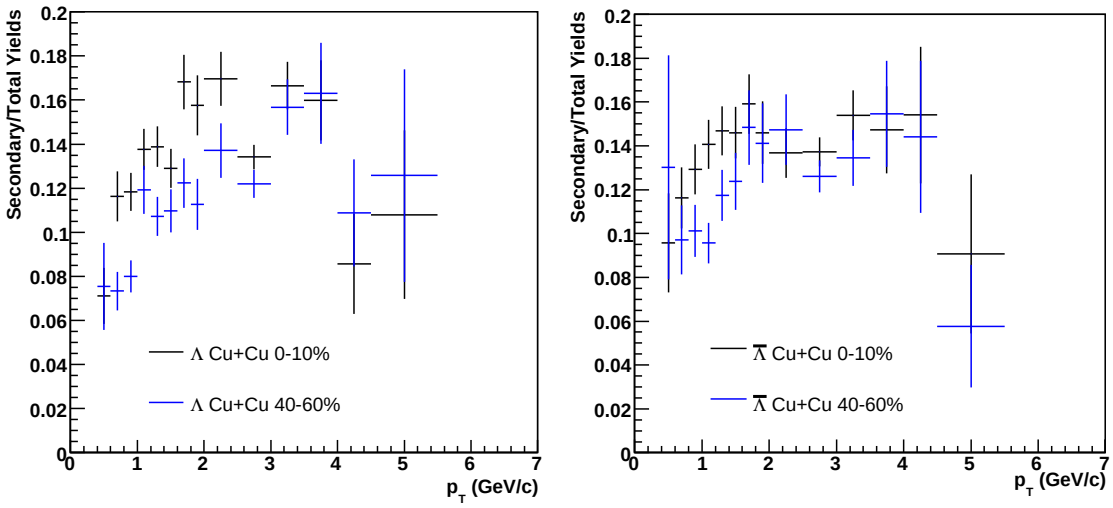

Figure 5.16: Ratio of secondary to total raw Λ and $\bar{\Lambda}$ particles as a function of p_T. Secondary contributions are calculated exclusively from Ξ^-, Ξ^0, Ξ^+, $\bar{\Xi}^0$ decays.

Figure 5.16 shows the secondary contributions to the total raw counts. For each particle, there appears a weak p_T dependance at $p_T < 1.5$ GeV/c which reflects the evolving topologies as a function of p_T, and little or no centrality dependance. On average, the secondary contribution for $\bar{\Lambda}$ particles is slightly higher than the secondary Λ contribution. In Au+Au $\sqrt{s_{NN}} = 200$ GeV collisions, the Ξ^-/Λ ratio was reported to be ~ 0.127, while the $\bar{\Xi}^+/\bar{\Lambda}$ ratio was ~ 0.140 independent of centrality [51]. Thus the slight differences in the secondary contributions probably

reflect the higher $\bar{\Xi}^+/\bar{\Lambda}$ ratio compared to the Ξ^-/Λ ratio in Cu+Cu $\sqrt{s_{NN}} = 200$ GeV collisions. Taking into account branching ratios in equation 5.18, the Ω^-/Λ and $\bar{\Omega^+}/\bar{\Lambda}$ ratios for Au+Au $\sqrt{s_{NN}} = 200$ GeV collisions were reported to be $\sim 1\%$ [51], thus the Ω^- and $\bar{\Omega}^+$ contributions to raw Λ and $\bar{\Lambda}$ yields were assumed negligible for this analysis. Finally, another method detailed elsewhere [126, 127] was investigated and found to give consistent secondary contributions with the method in this section.

5.6 Systematic Uncertainties

Conventionally, systematic uncertainties typically associated with corrected V0 yields can have two main sources:

- The ability of the Monte Carlo V0 simulations to reproduce the raw topological and hit distributions
- Variations of raw yields with respect to run conditions

There can also be systematic uncertainties with respect to background calculations for the invariant mass peaks, however the high signal to background ratios and arguably unambiguous choices of background calculation shown in section 5.3, negate the need to pursue these for the current analysis. The first point can be addressed by comparing the real and Monte Carlo topological/hit distributions, and if any mismatches are observed, they need to be understood with an assignment of systematic uncertainty if necessary. The second point can addressed by measuring raw V0 yields as a function of run day, luminosity, and B-field to investigate any changes in detector performance.

5.6.1 Comparison of Raw and Monte Carlo V0 Distributions

Figure 5.17 shows the raw and Monte Carlo distance of closest approach of the V0 to the primary vertex distributions as a function of p_T. The raw Λ and $\bar{\Lambda}$ distributions have had the secondary component from Ξ decays suitably subtracted as these differ from the primary distributions. Especially at low-p_T, the Monte Carlo V0s point more towards the vertex. The differences in the mean of the raw and Monte Carlo distributions range 0.05 to 0.1 cm. The reason is due to how the vertex resolution is treated in the simulation. For real V0s, the true vertex is not known therefore the reconstructed vertex position is used as an estimate which will be subject to a finite resolution smearing effect. However in the Monte Carlo data, the V0s are produced from a known vertex position (which is the reconstructed position), with the afore mentioned smearing missing. The differences observed in figure 5.17 were especially prominent in d+Au $\sqrt{s_{NN}} = 200$ GeV collisions where due to the fewer primary tracks, the vertex resolution was worse leading to larger mismatches than the ones shown [121]. Consequently, the distance of closest approach of the V0 to the primary vertex cut of 0.8 cm is proportionally rejecting more raw V0s than Monte Carlo V0s, leading to the corrected yields being systematically too low. This can be prevented by not placing this cut, however as mentioned previously, there are likely to be other vertices in the event thus the cut prevents contamination from pile-up. A systematic uncertainty will thus be associated for this mismatch with the calculation being described section 5.6.3.

Figure 5.18 shows a comparison of Λ raw and Monte Carlo TPC hit distributions as a function of V0 p_T for both daughters. There appears a p_T dependance for both raw and Monte Carlo distributions. In a given V0 momentum range, the positive daughters have a higher mean number of hits (the proton will carries a larger share of the momentum), while for the pion especially, the mean number of TPC hits

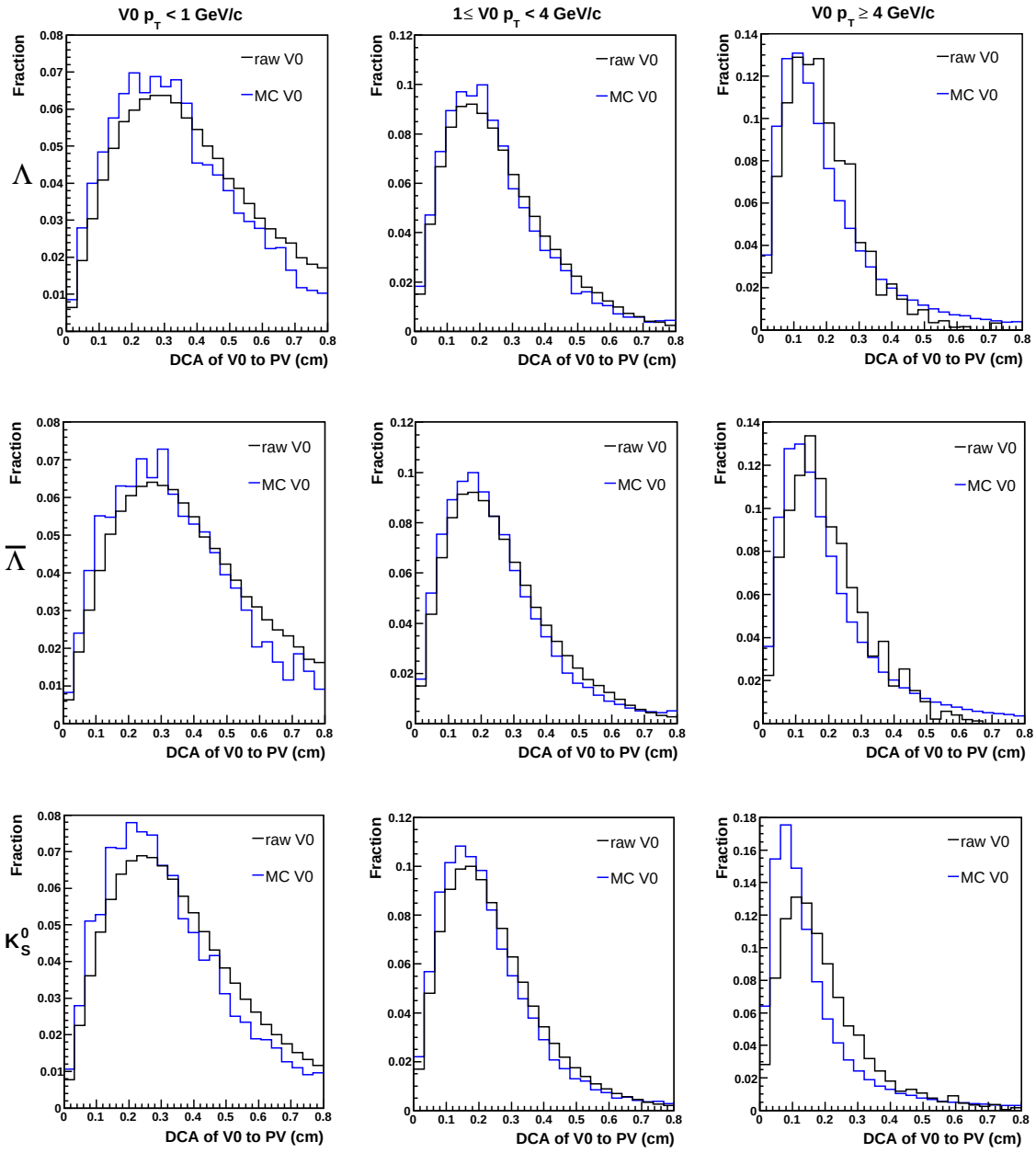

Figure 5.17: Comparison of raw and Monte Carlo (MC) distance of closest approach of the V0 to the primary vertex distributions for Cu+Cu 0-60% collisions.

increases with increasing V0 p_T. This is due to lower p_T tracks having a larger curvature and thus crossing more sector boundaries. Mismatches in the distributions are also observed, and these are most prominent for the lowest p_T pions with the resulting differences being ~ 2 hits between the means of each distribution. There are a couple of possibilities which may have lead to this:

- The TPC Response Simulator does not provide an adequate response for hits near the sector boundaries.
- The TPC Response Simulator does not provide an adequate response for tracks with larger crossing angles with respect to the pad row.

Whatever the reason, the TPC hit cut of 15 appears to be proportionally rejecting more Monte Carlo V0s than real V0s leading to the corrected yields being systematically too low. This is also observed for the $\bar{\Lambda}$ particles in the same figure, and the K^0_S particles in figure 5.19. However, as previously described, this cut cannot be loosened as it prevents split tracks forming V0s. A systematic uncertainty will thus be associated for this mismatch with the calculation again being described section 5.6.3.

Finally, comparisons of the raw and Monte Carlo distance of closest approach of V0 daughter to the primary vertex distributions, decay length distributions, and distance of closest approach of V0 daughters distributions were also made, however no mismatches where found. As the former two are dominated by kinematics and while the later track resolution, this implies that the Monte Carlo simulation reproduces both of these aspects well. The corrected yields for the east ($z < 0$) and west ($z > 0$) sides of the TPC were also compared and found to be consistent within statistical uncertainties.

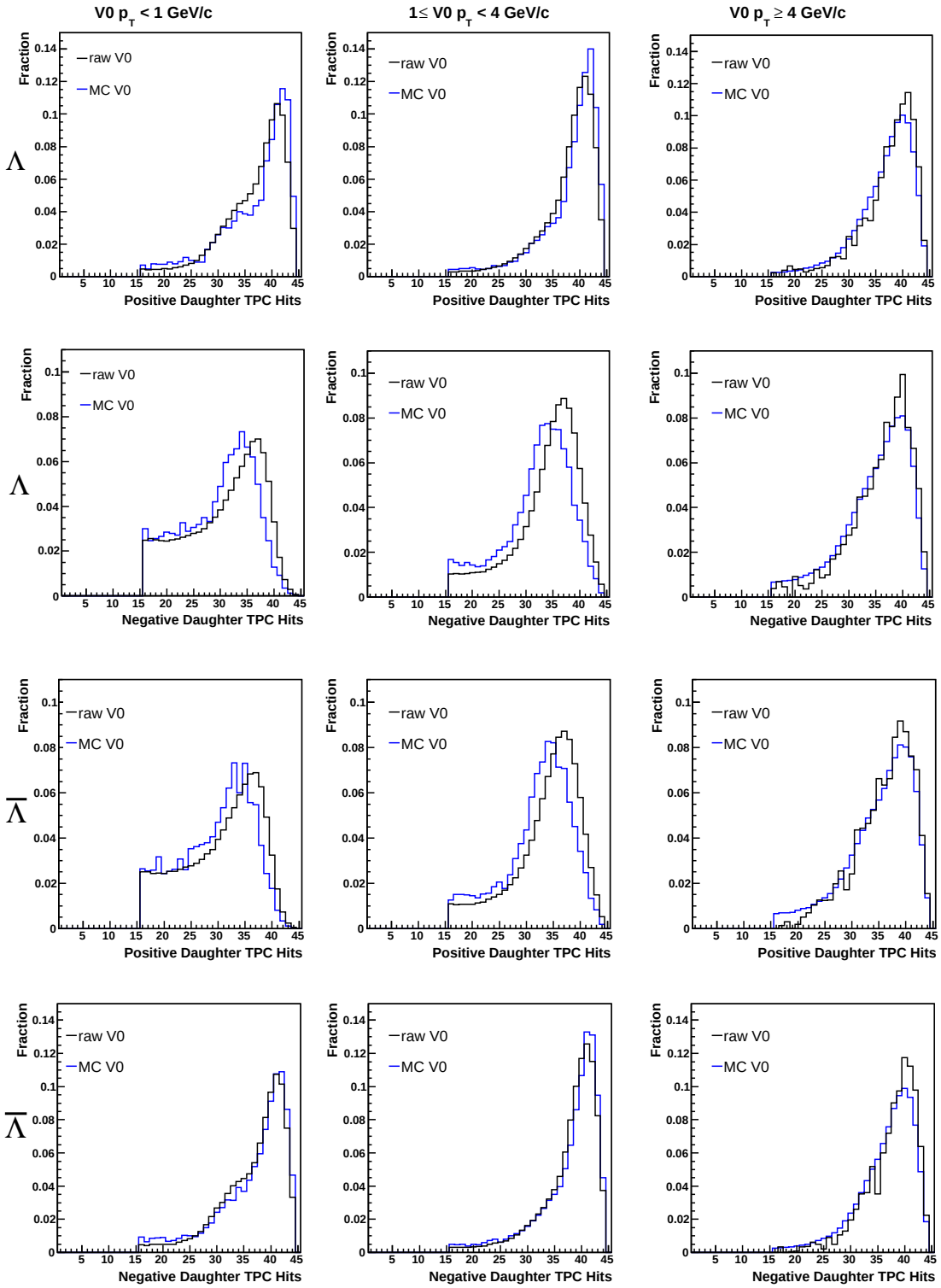

Figure 5.18: Comparison of Λ and $\bar{\Lambda}$ raw and Monte Carlo (MC) TPC hit distributions for Cu+Cu 0-60% collisions.

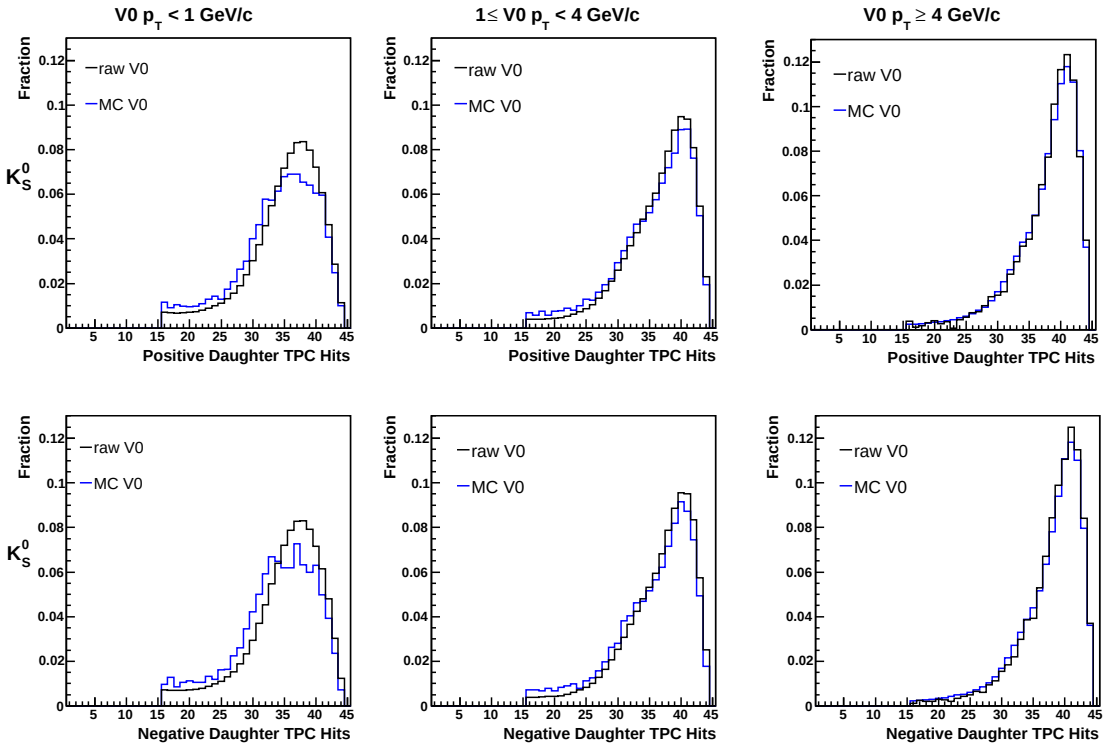

Figure 5.19: Comparison of K^0_S raw and Monte Carlo (MC) TPC hit distributions for Cu+Cu 0-60% collisions.

5.6.2 Run Conditions

Figure 5.20 shows a comparison of low and high luminosity yields. The raw high luminosity V0 yields are $\sim 3\%$ lower independent of p_T. When the corrections were compared in this way, a $\sim 3\%$ difference was also observed with the higher luminosity corrections being lower. Thus the raw yield luminosity dependence arises from the larger TPC occupancy (from pile-up) which serves to slightly inhibit V0 finding. No systematic uncertainty will be associated with this as the corrected yields are stable with respect to luminosity.

Figure 5.21 shows the run day dependence of raw V0 yields. As luminosity may vary on a day by day basis, events with just one vertex candidate were chosen to stop pile-up varying the V0 finding ability. The lines indicate the respective means. As Poisson fluctuations should give 2σ deviations (from the mean) in $\sim 1/20$

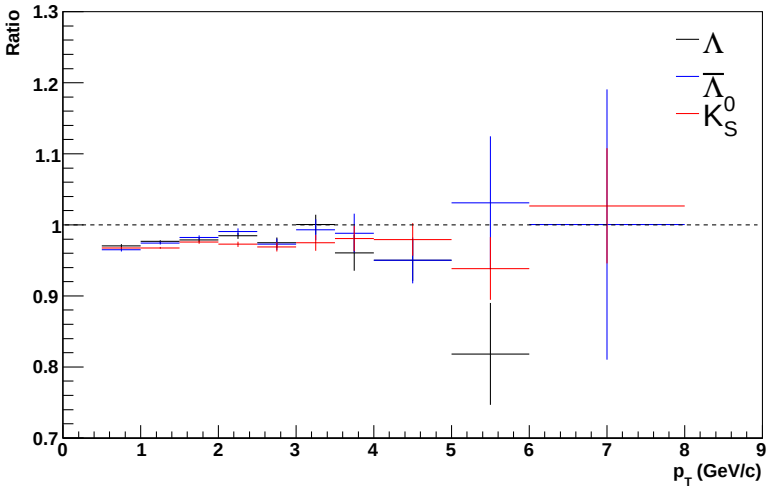

Figure 5.20: Comparison of high and low luminosity raw V0s yields for Cu+Cu 0-60% collisions. High luminosity is defined as events which are taken with a ZDC coincidence rate of above 13 kHz (roughly the mean) while low corresponds to a rate below 13 kHz. Uncertainties are statistical.

occurrences, there are clear non-statistical fluctuations which appear to exhibit a common pattern for all V0 raw yields. This non-statistical component is $\sim 2\%$ of the mean for each case, and is likely due to the varying TPC gas gain caused by atmospheric pressure variations. As the gain is directly related to the pad response, the ADC values used to determine hit position vary causing the reconstruction efficiency to vary. This effect has also been investigated with efficiency studies where the embedded ADC values were varied, and this led to changes in calculated single track reconstruction efficiency [125]. Regarding the corrections shown in section 5.4, as described, the embedded ADC counts were adjusted to match the typical values and thus did not encompass deviations from these typical values. Therefore a systematic uncertainty of 2% will be assigned to the corrected yields as unlike for luminosity, the variations shown in figure 5.21 are not reproduced for the corrections applied. The p_T dependance can not be investigated due the limited statistics for a given day so the uncertainty is applied independent of p_T.

Finally, as two B-field settings were used in the Cu+Cu $\sqrt{s_{NN}} = 200$ GeV run

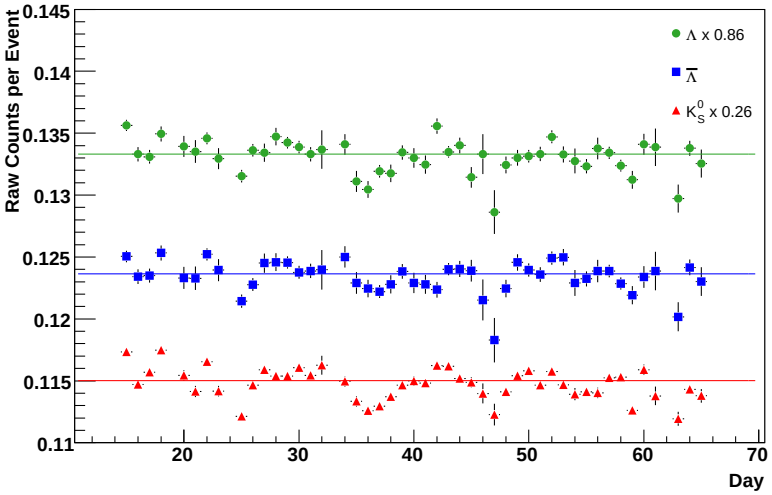

Figure 5.21: Raw V0 yields as a function of run day for Cu+Cu 0-60% collisions. Uncertainties are statistical.

(±0.5T), the raw yields were compared for each setting. Unlike for previous studies [51], the raw yields were consistent within statistics for the full p_T range, thus no systematic uncertainty need be applied.

5.6.3 Uncertainty Assignment

The uncertainties due to the mismatches shown in section 5.6.1 are calculated by producing corrected spectra with an offset applied to the corrections. For the distance of closest approach of the V0 to the primary vertex cut, in order to determine the scale of the uncertainty, corrected spectra are produced with a 0.8 cm cut on the raw yields, and a 0.7 cm cut on the corrections. The 0.1 cm difference (0.8-0.7) represents an upper limit on the difference in the mean of each distribution (raw vs. Monte Carlo) shown in figure 5.17. As the mismatch leads to the corrected yields being too low when the cut of 0.8 cm is applied to both the raw yields and corrections, the offset gives a larger corrected yield as the applied corrections are smaller, and therefore represents the scale of the uncertainty. For the TPC hit cut, the offset chosen is 2 (again upper limit on the difference in the respective means) which gives

a lower corrected yield with a Monte Carlo TPC hit cut of 13. As the corrected yield with a 15 TPC hit cut for both raw yields and corrections is likely to be too high, again the difference corresponds to scale of the systematic uncertainty on the corrected yield. This procedure is applied to all V0s. Figure 5.22 shows the ratios of corrected yields for the offsets applied on the K^0_S particles. These represent the fractional systematic uncertainties associated with both mismatches which become smaller with increasing p_T. This reflects the fact the cuts become increasingly distant from the main distributions as observed in section 5.6.1. Finally, the systematic uncertainties due to run day variations are added in quadrature to those previously calculated.

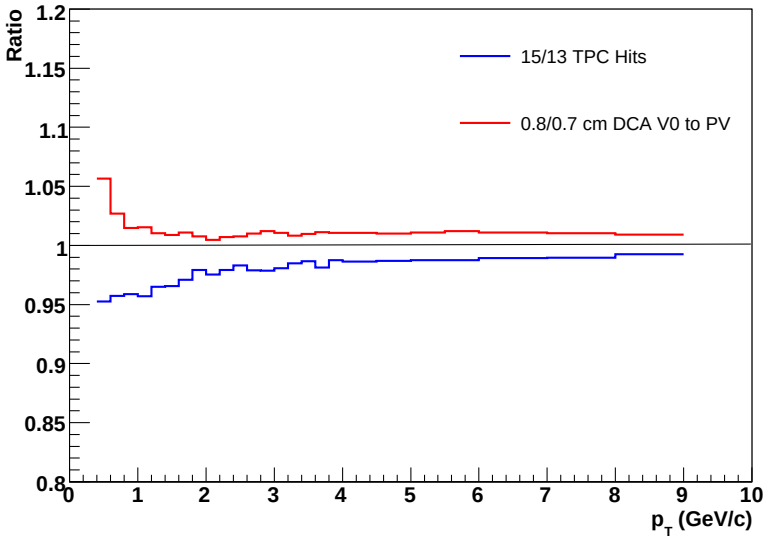

Figure 5.22: Comparison of correction sets for K^0_S particles from Cu+Cu 0-10% $\sqrt{s_{NN}} = 200$ GeV collisions. PV is an abbreviation for Primary Vertex, and DCA is Distance of closest Approach.

Chapter 6

RESULTS AND DISCUSSION

The processes responsible for particle production in heavy-ion collisions are conventionally divided into 3 intervals with respect to p_T. Soft QCD processes are expected to dominate production for $p_T \lesssim 2$ GeV/c, parton coalescence, baryon junction formation and fragmentation may compete for $2 \lesssim p_T \lesssim 5$ GeV/c, and jet fragmentation is expected to dominate for $p_T \gtrsim 5$ GeV/c. Figure 6.1 shows the corrected p_T spectra for the Λ, $\bar{\Lambda}$ and K^0_S particles from ~ 44 million Cu+Cu $\sqrt{s_{NN}} = 200$ GeV collisions. It is obvious that all particles have excellent p_T coverage which enables all of the above to be investigated with detailed comparisons to Au+Au $\sqrt{s_{NN}} = 200$ GeV collisions.

The chapter will start by investigating integrated yields which are dominated by production at low-p_T ($\lesssim 2$ GeV). It will then proceed to examine the mid-p_T and high-p_T yields by calculating Λ/K^0_S ratios and forming nuclear modification factors for the Λ, $\bar{\Lambda}$ and K^0_S particles. Implications for all of the afore will be discussed.

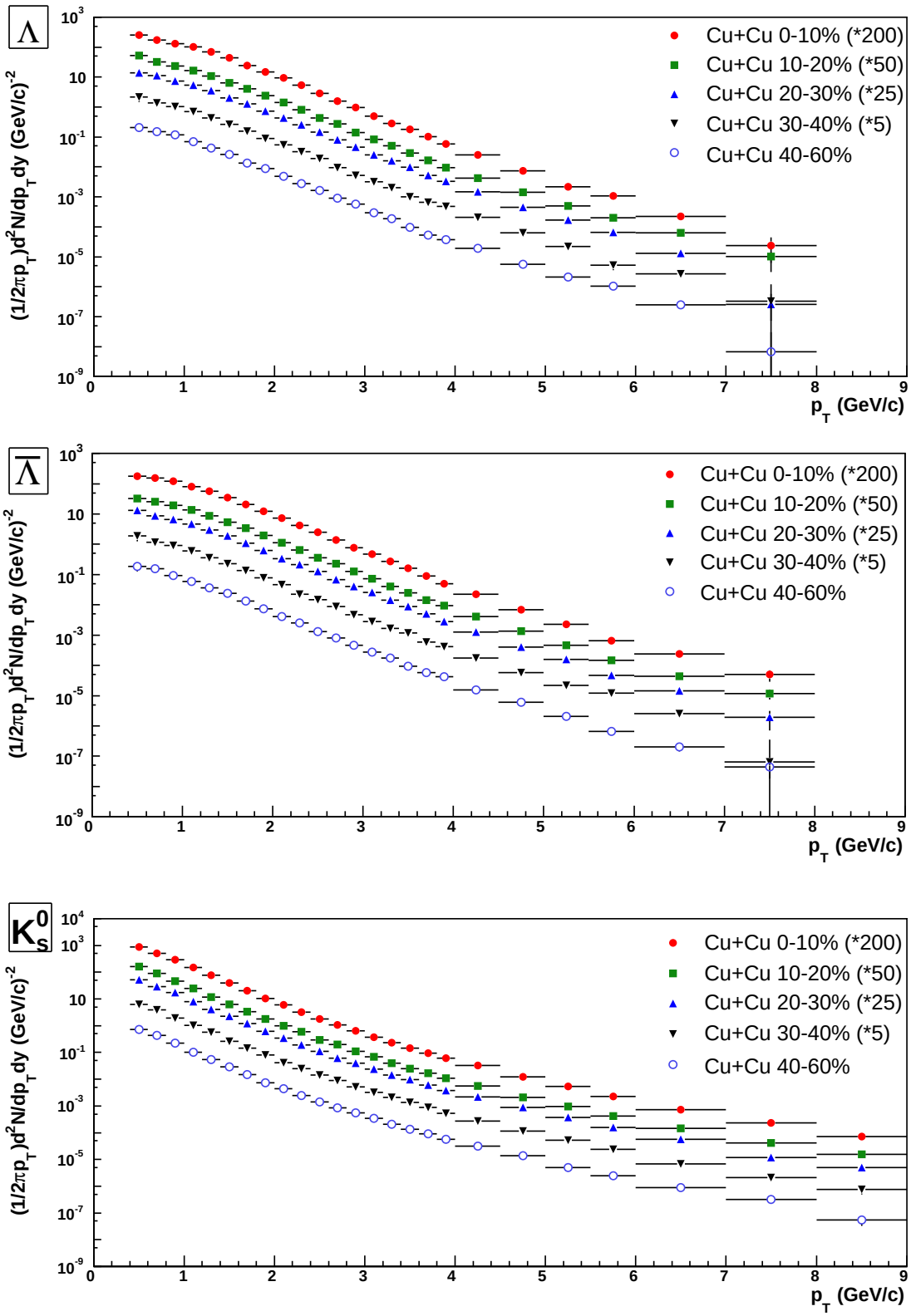

Figure 6.1: Mid-rapidity ($y < |0.5|$) Λ, $\bar{\Lambda}$ and K^0_S spectra for Cu+Cu $\sqrt{s_{NN}} = 200$ GeV collisions. For clarity the uncertainties shown are statistical only, and the Λ and $\bar{\Lambda}$ yields have not been feed-down subtracted.

6.1 Integrated Yields

As the p_T spectra in figure 6.1 are not measured below 0.4 GeV/c, a functional form has to be assumed and fitted in order to extract the integrated yields (dN/dy). For all the V0 particles, the m_T exponential shown in equation 2.6 will be used. It can be rearranged in terms of just dN/dy and T which gives the following expression:

$$\frac{1}{2\pi p_T}\frac{d^2N}{dydp_T} = \frac{dN/dy}{2\pi T(m_0+T)}e^{-\frac{m_T-m_0}{T}} \tag{6.1}$$

where m_0 is the rest mass of the particle. dN/dy and T are free parameters. As the combined statistical and systematic spectra uncertainties were included in the fitting procedure, the reported uncertainties in dN/dy and T will these, and are reported as such. For all particles, the fit range used was $p_T \leq 2$ GeV/c which gave a $\chi^2/DOF \sim 1$ when just the statistical uncertainties were included. Especially for peripheral collisions, a larger fit range led to the χ^2/DOF becoming greater than 1, which in turn shows the exponential description is only applicable at low-p_T. Moreover, as previously mentioned the $p_T \leq 2$ GeV/c range corresponds to $\sim 99\%$ of the integrated yield for all particles when T is of the order of hundreds of MeV, which negates the need to include the higher p_T points. For consistency, the same

Centrality	0-10%	10-20%	20-30%	30-40%	40-60%
Λ	4.93 ± 0.12	3.38 ± 0.10	2.20 ± 0.08	1.45 ± 0.06	0.75 ± 0.03
	339 ± 6	324 ± 7	321 ± 8	313 ± 9	297 ± 9
$\bar{\Lambda}$	4.11 ± 0.1	2.69 ± 0.09	1.90 ± 0.07	1.24 ± 0.06	0.66 ± 0.03
	339 ± 7	337 ± 8	318 ± 8	305 ± 10	298 ± 9
K^0_S	12.7 ± 0.47	8.54 ± 0.37	5.46 ± 0.25	3.57 ± 0.18	1.9 ± 0.10
	284 ± 5	280 ± 5	286 ± 5	284 ± 6	278 ± 6

Table 6.1: Mid-rapidity ($|y| < 0.5$) integrated yields (top row for a given particle) and m_T exponential slope parameters (MeV) for Cu+Cu $\sqrt{s_{NN}} = 200$ GeV collisions. The uncertainties combined statistical and systematic, and the Λ and $\bar{\Lambda}$ yields have been subtracted for weak decay feed down.

procedure was carried out on the previously published Au+Au $\sqrt{s_{NN}} = 200$ GeV

spectra [51, 84] in order to make yield comparisons of both systems [1]. To give Λ and $\bar{\Lambda}$ weak decay feed-down subtracted dN/dy and T values (c.f. section 5.5), the spectra points have these contributions subtracted and then the fit is performed.

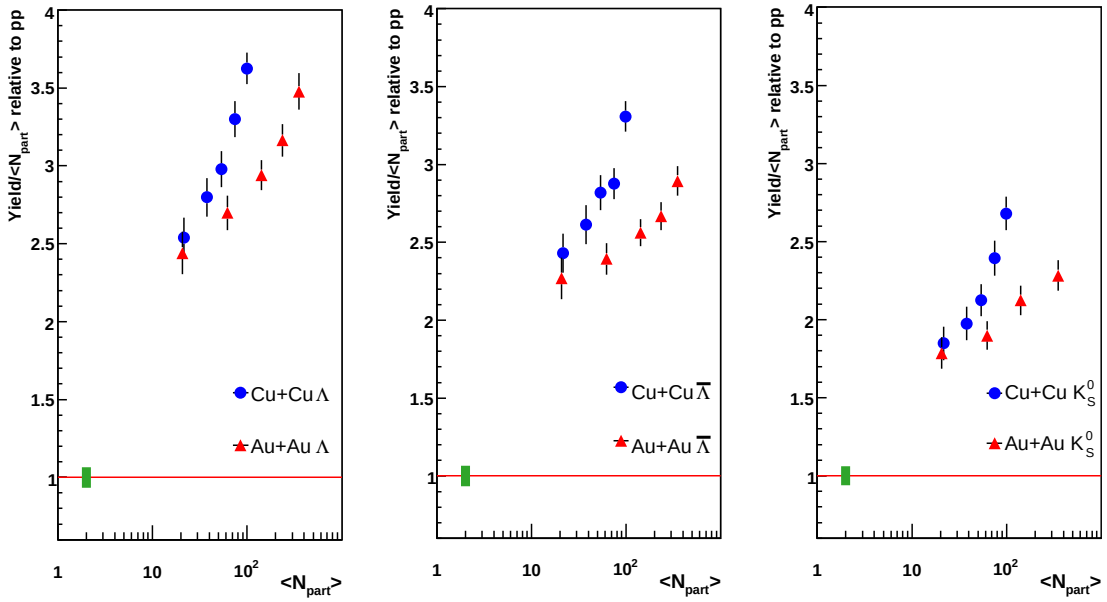

Figure 6.2: Mid-rapidity strangeness enhancement of the Λ, $\bar{\Lambda}$ and K^0_S particles for Cu+Cu and Au+Au collisions with $\sqrt{s_{NN}}$ = 200 GeV. The Λ and $\bar{\Lambda}$ yields have been feed down subtracted in all cases, and the green bars show the normalisation uncertainties. The uncertainties for the heavy-ion points are the combined statistical and systematic.

Figure 6.2 shows the resulting participant scaled mid-rapidity yields for both Cu+Cu and Au+Au $\sqrt{s_{NN}}$ = 200 GeV collisions normalised by the p+p values. The format in figure 6.2 is identical to the one shown in figure 1.5 modulo the fact that the y-axis is shown on a linear scale. In addition to the $\sim 2-4$ enhancements exhibited by all particles for both Cu+Cu and Au+Au collisions, it is quite clear that at a given value of $\langle N_{part} \rangle$ above 60, strangeness production is higher in Cu+Cu

[1] An alternative procedure involves carrying out three fits on the spectra points where the y values correspond to the upper, central, and lower values of the systematic uncertainty. The differences in dN/dy therefore will also reflect the systematic uncertainty on the integrated yield. However, for reasons of practicality, the Au+Au spectra points are only available with the statistical and systematic uncertainties combined which prevents such a method being used for Cu+Cu and Au+Au. In addition, both methods were found to give similar systematic uncertainties in Cu+Cu.

collisions compared to Au+Au. The trend at the AGS and SPS appears to apply at RHIC energies also. As previously mentioned, in the Canonical framework this is surprising as volume (assuming it is proportional to $\langle N_{part} \rangle$) is the controlling factor in strangeness yields per volume as demonstrated in figure 2.8. Moreover, as the extracted chemical freeze-out temperature and baryo-chemical potential (u_b) values for Cu+Cu and Au+Au have been shown to be consistent and independent of system size [128], Canonical predictions for Cu+Cu and Au+Au should also be the same. This is clearly not reproduced by the data. There are other Canonical predictions which assume the correlation volume may scale with $\langle N_{part} \rangle^{1/3}$ or $\langle N_{part} \rangle^{2/3}$ and these give slower rises in E as a function of $\langle N_{part} \rangle$[129]. Although these have been shown to match the Au+Au data better as the Grand Canonical limit is reached later, they also give monotonically rising predictions which are again inconsistent with the combined Cu+Cu and Au+Au data.

These observations point to a failure in the thermal models to describe strangeness yields per unit volume at RHIC. This may be attributed to the fact that volume is difficult to establish in heavy-ion collisions, or that the fireball at chemical freeze-out is not in thermal equilibrium. As a result, this section will focus on specific dynamical interpretations to the observations in figure 6.2 which don't explicitly require the fireball to be in thermal equilibrium. As the V0 behaviour with respect to the differences in Cu+Cu and Au+Au appears the same independent of particle species, and the Λ, $\bar{\Lambda}$ and K particles carry the bulk of strangeness in heavy-ion collisions, bulk strangeness production per participant is highly likely to be higher in central Cu+Cu collisions compared Au+Au collisions with similar $\langle N_{part} \rangle$. In order to approximate total strangeness production at mid-rapidity, the following yield will be calculated:

$$\frac{dN_{\langle s+\bar{s} \rangle}}{dy} = 1.48\frac{dN_{\Lambda}}{dy} + 4\frac{dN_{K^0_S}}{dy} + 1.48\frac{dN_{\bar{\Lambda}}}{dy} \tag{6.2}$$

The factors of 1.48 account for the production of (anti) Σ particles which have

a similar quark content to the Λ particles, and the factor of 4 accounts for the production of $K^{\pm}$ and K^0_L particles [79]. The multi-strange hadrons are neglected due to their small contribution to overall strangeness production ($\sim 8\%$ for central Au+Au $\sqrt{s_{NN}} = 200$ GeV collisions). The left panel in figure 6.3 shows $dN_{\langle s+\bar{s}\rangle}/dy$ per participant in Cu+Cu and Au+Au $\sqrt{s_{NN}} = 200$ GeV collisions scaled by the p+p values as a function of $\langle N_{part}\rangle$. Due to its definition, this measurement follows the same trend as the individual V0 values.

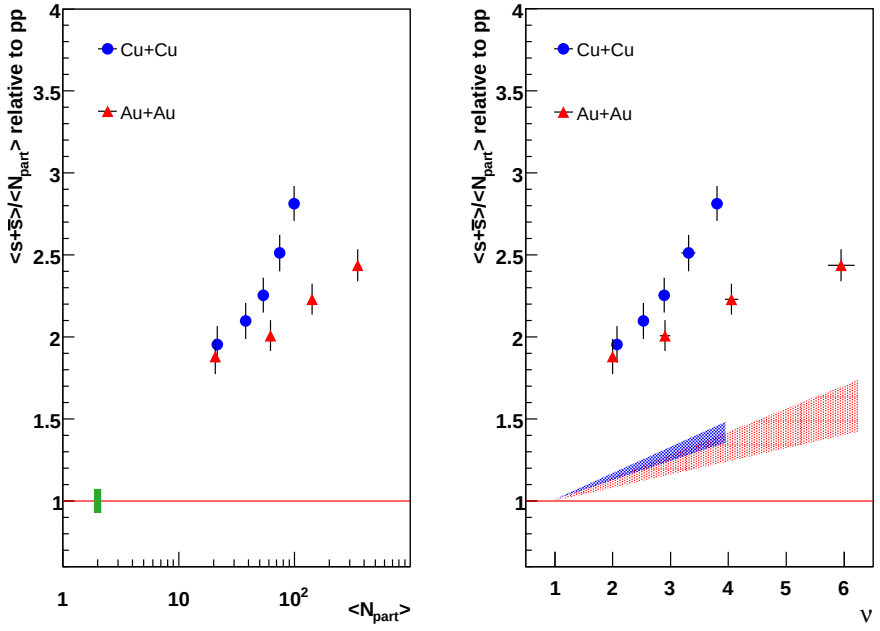

Figure 6.3: Bulk strangeness production per participant in Cu+Cu and Au+Au $\sqrt{s_{NN}} = 200$ GeV collisions as a function of $\langle N_{part}\rangle$ and $\nu(2\langle N_{bin}\rangle/\langle N_{part}\rangle)$. The uncertainties presented are in the same format as figure 6.2. The blue area shows Cu+Cu charged hadron yields per participant derived from the Kharzeev-Nardi fits in section 4.4, while the red area shows the same for Au+Au. The Au+Au x values where taken from here [107].

The right panel in figure 6.3 shows bulk strangeness production per participant as a function of ν $(2\langle N_{bin}\rangle/\langle N_{part}\rangle)$. For the Kharzeev-Nardi relation shown by equation 4.7, when the enhancement factor in equation 1.11 is calculated for charged

hadrons, the following relation applies:

$$\frac{\frac{dN}{d\eta}/N_{part}}{n_{pp}/2} = x(\nu - 1) + 1 \tag{6.3}$$

which is therefore proportional to ν, with x being the gradient that characterises the contribution from hard processes (which scale with N_{bin}) assuming soft processes scale with N_{part}. x has been extracted for Cu+Cu and Au+Au $\sqrt{s_{NN}} = 200$ GeV collisions and for comparison, bulk hadron production per participant is also shown. The respective areas represent the uncertainty in x. Above $\nu = 1$ for both systems, it is clear that the rise in strangeness per participant is more aggressive than for bulk hadronic matter per participant. In light of this, it could be argued that in Kharzeev-Nardi framework, x would be higher for strangeness production (compared to bulk hadron production) due to the higher strange quark mass compared to up and down masses typically produced for bulk hadrons. In other words, as soft processes involve low momentum transfers they would be less amenable to strange quark production compared to the other light quark production. The extreme case would be for the heavy charm quark, and it has indeed been shown experimentally at RHIC energies [130], that charm production scales with the number of binary collisions i.e. it results purely from hard processes as $x \sim 1$. Thus the "enhancement" of strangeness in heavy-ion collisions merely reflects the fact that $0 < x \leq 1$ and $\nu > 1$. However, both Cu+Cu and Au+Au strangeness data appear to show a non-linear rise above $\nu = 1$ which is counter to the predictions made by equation 6.3. Secondly, although arguably not the case for bulk hadron production, x for strangeness production appears to depend on collision system. In the Kharzeev-Nardi framework, this should just depend on the centre of mass energy ($\sqrt{s_{NN}}$) in line with QCD predictions that the relative contribution of hard process to particle production increases with increasing centre of mass energy [131]. It therefore appears that the Kharzeev-Nardi framework is difficult to reconcile with strangeness

production.

The K/π ratios in the left panel of figure 1.7 were found to lie on a common trend when $\langle N_{part} \rangle$ was replaced with the number of inelastic collisions within the nucleus-nucleus penetration time per overlap volume per overlap time. This shown in figure 6.4 and suggests that the differences with respect to strangeness production between the light and heavy systems at the SPS energies, may be due to higher initial energy densities in light systems of a similar $\langle N_{part} \rangle$ to heavy systems. The remainder

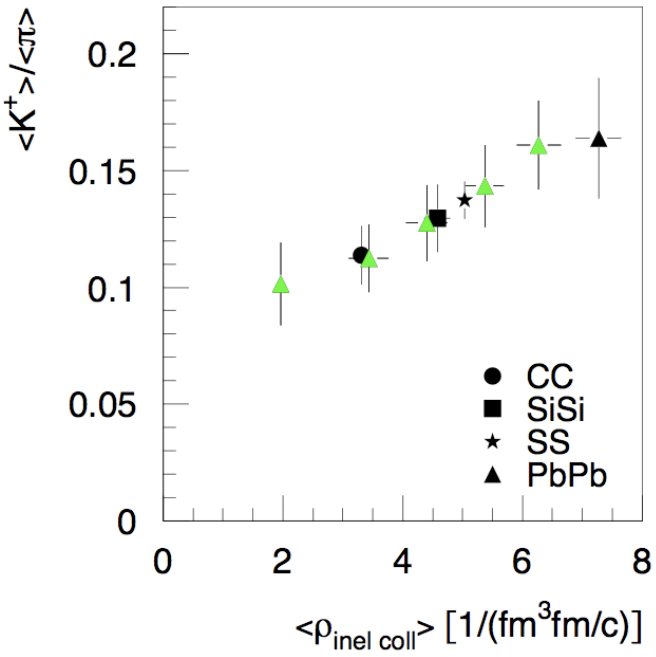

Figure 6.4: The K/π ratio for $\sqrt{s_{NN}} = 17.3$ GeV collisions (as in figure 1.7) as a function of the number of inelastic collisions per collisional overlap volume per collisional overlap time [42].

of this section will adopt a similar approach for bulk strangeness per participant yields from Cu+Cu and Au+Au $\sqrt{s_{NN}} = 200$ GeV collisions. As will become clear later, the energy density numerator will be hadron yields rather than the number of inelastic collisions in order to make more direct comparisons of strangeness to the Bjorken energy density. These comparisons are shown in figure 6.5 and will be discussed as follows. The left most panel shows the dependence on particle density

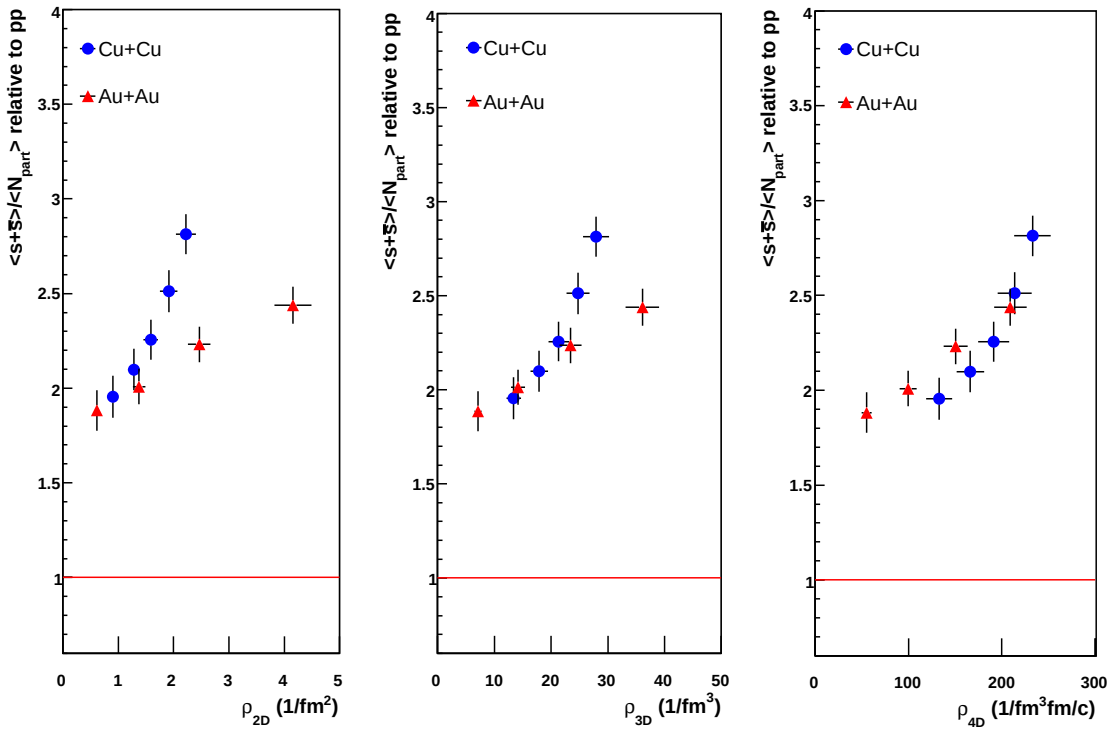

Figure 6.5: Bulk strangeness production per participant in Cu+Cu and Au+Au $\sqrt{s_{NN}}$ = 200 GeV collisions as a function of bulk hadronic densities. The uncertainties presented are again in the same format as figure 6.2. See text for details on density definitions.

which is calculated as follows:

$$\rho_{2D} = \frac{3}{2}\frac{dN_{charge}}{d\eta}\frac{1}{A} \tag{6.4}$$

where dN_{charge}/dy is the mid-rapidity charged hadrons yield[2]. The factor 3/2 aims to include the neutral particles in the density calculation and as mentioned in section 2.2.3, the number of hadrons is expected to be similar to the number of initial quanta on grounds of entropy conversation. The transverse overlap area, A, is calculated from the mean impact parameters (for a given centrality) assuming an ellipsoid

[2]It should also be noted that mid-rapidity charged hadron $dN/d\eta$ for Cu+Cu an Au+Au $\sqrt{s_{NN}}$ = 200 GeV collisions has a very strong relation to the total multiplicity given the "plateau" structure of the $dN/d\eta$ distribution which is centered at $\eta \sim 0$ with the shoulders at $|\eta| \simeq 2$ [112, 116].

overlap shape and spherical Cu and Au nuclei. Both dN_{charge}/dy and the impact parameters are derived from the same Glauber study [107]. The effective nuclear radii for Cu and Au were taken to be the respective mean impact parameter over the full centrality range (which corresponded to half the maximum impact parameters thus double the effective radius here [44]), and this lead to both radii containing 99.3% of the Woods Saxon distribution. The above relation is similar to Bjorken energy density calculated in equation 2.4 as $\rho_{2D} = \epsilon_{bj}(\tau_0/\langle m_T \rangle)$ where $\langle m_T \rangle$ is the mean particle energy (at mid-rapidity), and is used as dE_T/dy has not been determined for Cu+Cu $\sqrt{s_{NN}} = 200$ GeV collisions. When bulk strangeness per participant is ordered with respect to ρ_{2D}, it is clear that the Cu+Cu and Au+Au values do not lie on the same trend. This in turn shows that the Bjorken energy density might not be the appropriate parameter for strangeness per production participant assuming the τ_0 and $\langle m_T \rangle$ have the same values for all Cu+Cu and Au+Au centralities.

Such a failure motivates other forms of particle densities to be investigated. The middle panel shows the strangeness per participant as function of particle production per unit volume which is calculated as:

$$\rho_{3D} = \frac{3}{2}\frac{dN_{charge}}{d\eta}\frac{1}{Al} \tag{6.5}$$

where l is the maximum longitudinal overlap length in z of the colliding nuclei measured in the center of mass frame. As $\gamma \sim 106$ for collisions with a center of mass energy of 200 GeV per nucleon pair, l will be Lorentz contracted compared to heavy-ion collisions with center of mass energies where $\gamma << 1$. For a central Cu+Cu collision, if r_C is the effective nuclear radius $l \sim 2r_c/\gamma = 0.13$ fm, and for central Au+Au collisions $l \sim 0.19$ fm. It differs from the Bjorken calculation as the longitudinal extent of system is governed by the collision region and not the formation time/rapidity range. Compared to Au+Au collisions, this extent is

typically smaller for Cu+Cu collisions, and thus an improvement in relation to ρ_{2D} is observed as all Cu+Cu points move to right. The right panel shows particle production per unit volume per overlap time:

$$\rho_{4D} = \frac{3}{2}\frac{dN_{charge}}{d\eta}\frac{1}{Al\tau_c} \tag{6.6}$$

where τ_c is the crossing time in the nuclear collision which is equal to l in natural units. This measurement is similar to the one shown in figure 6.4. Again for central Cu+Cu and Au+Au collisions, τ_c is $\sim$ 0.13 fm/c and $\sim$ 0.19 fm/c respectively. These values are smaller than the quoted Bjorken formation time of $\tau_0 \sim 0.35$ fm/c. As with ρ_{3D}, there is an improvement in relation to ρ_{2D}, and ρ_{3D} are ρ_{4D} are explicitly correlated given the overlap time and length are equal. Both the ρ_{3D} and ρ_{4D} scalings point to the fact that strangeness production per participant may be controlled by the bulk particle density in space and/or time. Furthermore, given and space and time dimensions used, the correlation also suggests that bulk strangeness is made early when the most energetic collisions are expected to occur.

In terms of dynamics, figure 6.6 attempts to demonstrate why including the overlap length may lead to a better density calculation with regard to strangeness production. The circles indicate where quanta (in Bjorken's terms) are produced in a heavy-ion collision. It is clear that for the high density regime (small l and τ_c), the trajectories of the quanta are more likely to cross perhaps leading to higher numbers of inelastic collisions producing strangeness. In heavy-ion collisions the "quanta" are likely to be dominated by gluons, and at RHIC energies most are predicted to have an energy around the *saturation scale* which has been extracted as $Q_s \sim 1-2$ GeV [109, 132]. Using the uncertainty principle, the respective formation time $\tau_0 \sim 0.2 - 0.1$ fm/c which is close to the previously mentioned crossing times. However, as the de Broglie wave length $\lambda \sim 0.1 - 0.2$ fm is also comparable with the longitudinal extent of the collision zone, such gluons might not be longitudinally

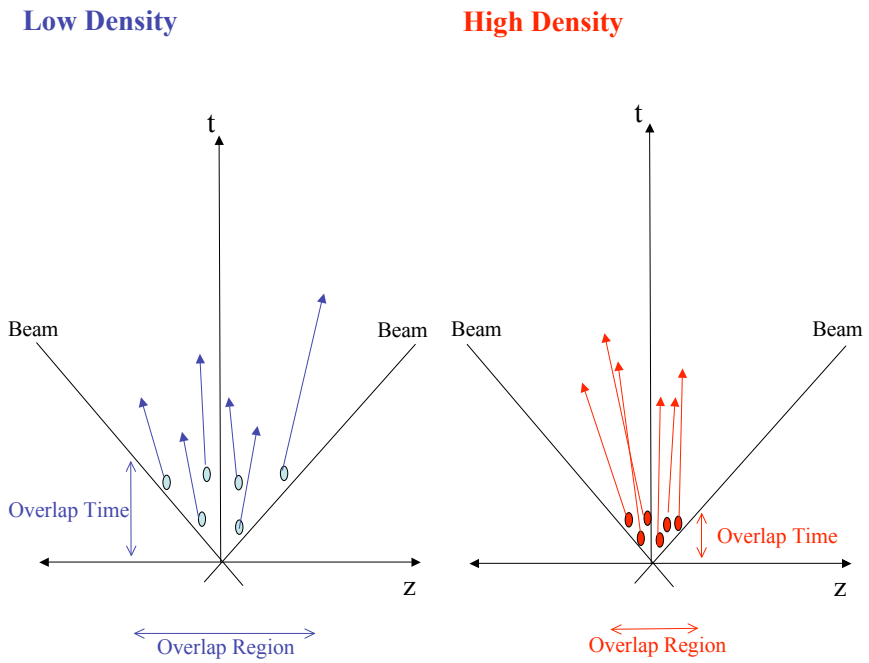

Figure 6.6: Space-time diagram contrasting low and high ρ_{4D} values. The arrows show the possible quanta trajectories, and z is in the longitudinal direction.

separated as implied in figure 6.6. In turn this suggests that higher energy partons may play a significant role in strangeness production, and these will "see" a different collision zone (as they have a smaller λ) compared to gluons with $Q_s \sim 1-2$ GeV which presumably dominate bulk hadron production. This is to be expected given the higher mass of the strange quark compared to the up and down quarks, and if such an rationale is correct, manifests itself in the different yields per participant evolutions shown in the right panel of figure 6.3. In addition, higher energy partons will also have smaller formation times further validating the use of the τ_c as the relevant time coordinate. An alternative and perhaps complementary explanation is that high ρ_{4D} values correspond to high QCD string densities, i.e. more colour rope formation, and this leads to increasing strangeness per participant values with increasing ρ_{4D}.

Finally, it is important to note that assuming a hadronic gas is responsible for

bulk strangeness production in heavy-ion collisions would mean that strangeness is produced during/after the hadron formation time. This is the time it takes for quarks to separate into the size of hadron (0.5-0.8 fm/c), and can be calculated as $t_h \sim 2.4$ fm/c assuming $\langle m_T \rangle \sim 0.57$ GeV and pions dominate the degrees of freedom [133]. The higher t_h compared to the hadron size is due to time dilation as the preformed pion energy is larger than the mass. It is clear that the correlation in right panel figure 6.5 becomes meaningless assuming hadronic interactions drive strangeness production as $t_h >> \tau_c$, and if indeed not merely a consequence, implies parton-parton interactions command such a role which is expected for QGP formation in heavy-ion collisions at RHIC.

6.2 Beyond Bulk Strangeness Production

In the previous section, the majority of strange particle production occurs for $p_T \lesssim 2$ GeV/c. This section aims to investigate production beyond this where soft and hard QCD processes compete. Figure 6.7 shows the Λ/K^0_S as a function of p_T in Cu+Cu and Au+Au with $\sqrt{s_{NN}} = 200$ GeV collisions. Like for Au+Au, the Cu+Cu mid-p_T ratios ($1.5 \lesssim p_T \lesssim 5$ GeV/c) increase from peripheral to central collisions. As described in section 2.3, this can be attributed to parton coalescence and/or baryon junction formation playing an increasingly dominant role for Λ production relative to K^0_S production. The low-p_T ($p_T \lesssim 1.5$ GeV/c) and high-p_T ($p_T \gtrsim 5$ GeV/c) ratios appear common for all systems investigated.

A more careful examination of figure 6.7 indicates the Cu+Cu 0-5% mid-p_T Λ/K^0_S ratios ($\langle N_{part} \rangle \sim 107$), are higher than the Au+Au 20-40% values ($\langle N_{part} \rangle \sim 140$). In order to investigate this further, figure 6.8 shows integrated Λ/K^0_S ratios as a function of the mean number of participants. It is clear that the mid-p_T Cu+Cu values lie on a higher trend than the Au+Au values. This is not the case for low-p_T values as expected from figure 6.7. Relative to Au+Au, for a given mean number

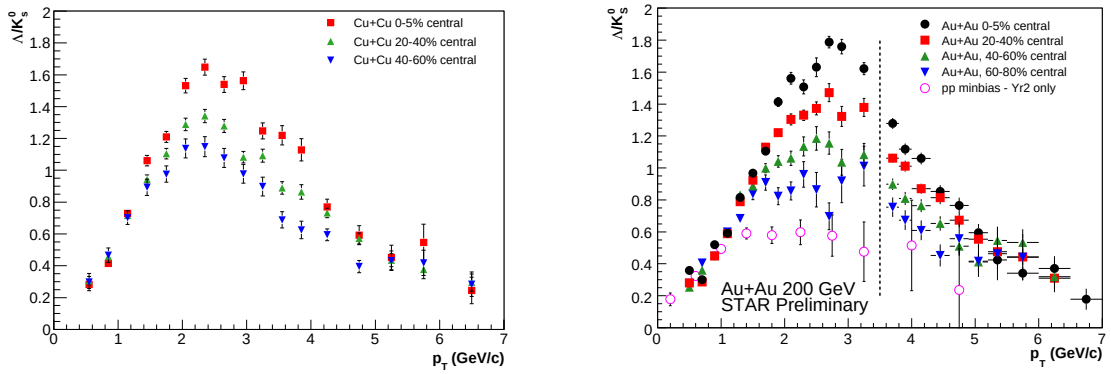

Figure 6.7: Λ/K^0_S in Cu+Cu and Au+Au collisions with $\sqrt{s_{NN}} = 200$ GeV. The Λ yields in Au+Au have not been subtracted for feed-down which was estimated to be $\sim 15\%$. The Cu+Cu data follows suit with a similar feed-down contribution. The uncertainties are statistical in all cases, and the Au+Au data are from [129].

of participants, in Cu+Cu collisions there is either a mechanism enhancing Λ production such as increased coalescence, or a mechanism suppressing K^0_S production such as larger jet quenching. Indeed, it has been predicted that jet quenching might be larger for Cu+Cu collisions at a given $\langle N_{part} \rangle$ due to the mean path length jets transverse being larger [134]. To date, there have been no such parton coalescence and/or baryon junction predictions for excess mid-p_T Λ production in Cu+Cu collisions, however if the thermal strange quark spectrum is enhanced as indicated in the previous section, one may expect such an excess for production via coalescence. In any case, the spatial nuclear geometry appears to be playing an important role in strangeness production for this region of phase space when comparing Cu+Cu and Au+Au at similar $\langle N_{part} \rangle$.

In order to understand the Cu+Cu and Au+Au differences further, figure 6.9 shows R_{AA} for the Λ, $\bar{\Lambda}$ and K^0_S particles from Cu+Cu 0-10% $\sqrt{s_{NN}} = 200$ GeV collisions (right most blue point in figure 6.8) and Au+Au 20-40% $\sqrt{s_{NN}} = 200$ GeV collisions (third red point from the right in figure 6.8). It is clear the baryon-meson differences shown for Au+Au 0-5% collisions in figure 2.12 apply here also. The high-p_T ($p_T \gtrsim 5$ GeV/c) charged hadron R_{AA} values have been measured for

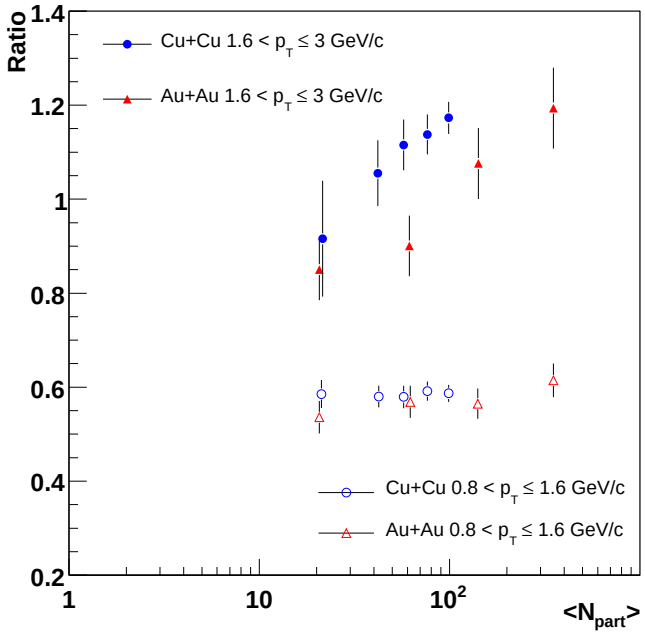

Figure 6.8: Λ/K^0_S ratios as a function of $\langle N_{part} \rangle$ and p_T for Cu+Cu and Au+Au $\sqrt{s_{NN}}$ = 200 GeV collisions. The Λ yields have been subtracted for feed-down in all cases, and the uncertainties are the combined statistical and systematic. The Au+Au data are from [51, 84].

both Cu+Cu 0-10% and Au+Au 20-40% collisions to be $R_{AA} \sim 0.5$ indicated by the magenta arrows. This is higher than $R_{AA} \sim 0.2$ shown in figure 1.6 for central Au+Au $\sqrt{s_{NN}}$ = 200 GeV collisions in the same p_T range, and indicates jets are less suppressed in the smaller systems. The charged hadron similarities for Cu+Cu 0-10% and Au+Au 20-40% R_{AA} values appears to extend to the K^0_S particles; the R_{AA} values are the same for $p_T \gtrsim 1.5$ GeV/c.

However, for the $1.5 \lesssim p_T \lesssim 3$ GeV/c range, the Cu+Cu Λ and $\bar{\Lambda}$ R_{AA} values are systematically higher than the respective Au+Au values. As mentioned in section 1.3.4, the excess baryon R_{AA} values can be attributed to an additional production mechanism beyond fragmentation. Such a mechanism, whether it is parton coalescence and/or baryon junction formation, appears to have a relatively larger contribution in Cu+Cu collisions assuming jet Λ and $\bar{\Lambda}$ production per binary collision is the same for both systems. The assumption is justified when considering K^0_S

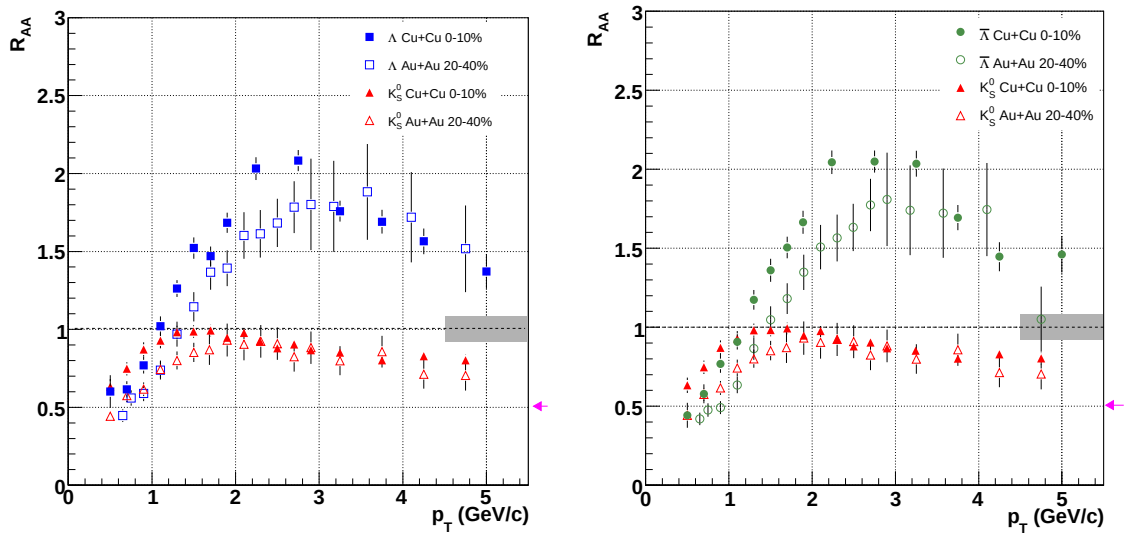

Figure 6.9: R_{AA} for neutral strange particles in Cu+Cu and Au+Au $\sqrt{s_{NN}} = 200$ GeV collisions. All Λ and $\bar{\Lambda}$ yields have had their respective feed-down contributions subtracted. The uncertainties are the combined statistical and systematic for heavy-ions, and the p+p reference is determined by the spectra parameterisation in [61]. The uncertainties for the p+p reference are not propagated to insure that the heavy-ion uncertainties are independent for Cu+Cu and Au+Au comparisons. The Au+Au data are from [51, 84], the grey area represents the uncertainty in the number of binary collisions, and the arrows show approximate charged hadron values for both systems at $p_T \gtrsim 5$ GeV/c [135].

and charged hadron R_{AA} values. Given the fact that soft strangeness production has been shown to be enhanced in Cu+Cu collisions relative to Au+Au collisions of a similar $\langle N_{part} \rangle$, one could argue that this is "leaking" into mid-p_T enhancing Λ production via coalescence. This manifests itself in the higher mid-p_T Λ/K^0_S values for Cu+Cu collisions at a given $\langle N_{part} \rangle$, and higher Cu+Cu Λ and $\bar{\Lambda}$ R_{AA} values. On the other hand, as mentioned in section 2.3.2, an implementation of the HIJING model [90] predicts large baryon R_{AA} values (from junctions) by increasing the string constant for Au+Au collisions relative to p+p. If higher ρ_{4D} values for central Cu+Cu collisions relative to mid-central Au+Au collisions lead to higher strings constants (through more color ropes) in the former, this could also explain why R_{AA} and the mid-p_T Λ/K^0_S ratios are higher for Cu+Cu.

Figure 6.10 shows the alternative nuclear modification factor R_{CP} for the Λ, $\bar{\Lambda}$ and K^0_S particles in Cu+Cu $\sqrt{s_{NN}} = 200$ GeV collisions. This is defined as follows:

$$R_{CP} = \frac{\text{Yield}_{\text{Cu+Cu 0-10\% collisions}}/\langle N_{bin}\rangle}{\text{Yield}_{\text{Cu+Cu 40-60\% collisions}}/\langle N_{bin}\rangle} \tag{6.7}$$

where each yield is divided by the respective number of binary collisions for a given centrality. Compared to figure 6.9, the reference spectra in this case are from pe-

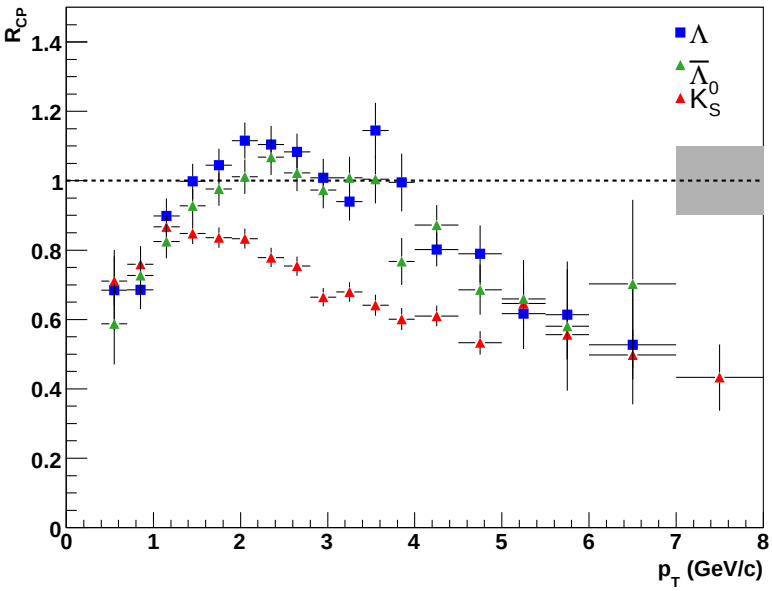

Figure 6.10: R_{CP} for Cu+Cu $\sqrt{s_{NN}} = 200$ GeV collisions. C is 0-10% and P is 40-60%. As the feed down contributions to the Λ and $\bar{\Lambda}$ yields where similar for both centralities, these were not subtracted in order to the extend the measurement further out in p_T. Only statistical errors are shown due to the highly correlated systematic uncertainties. The grey area represents the uncertainty in the number of binary collisions.

ripheral Cu+Cu collisions rather than p+p. This measurement has the advantage of extending the nuclear modification factor out to further p_T[3], but the disadvantage that the reference system might not be free of the previously mentioned enhancement/suppression mechanisms determined by measuring R_{AA}. As with R_{AA}, there

[3]The current V0 yield measurements for p+p $\sqrt{s_{NN}} = 200$ GeV collisions only extend to $p_T \sim 5$ GeV/c [61].

is a clear difference in strange baryon and meson values at mid-p_T. This suggests that in central collisions relative to peripheral, there is an extra source of particle production in addition to jet fragmentation enhancing the Λ and $\bar{\Lambda}$ production. The higher mid-p_T central Λ/K^0_S ratios relative to peripheral collisions support this. However, the highest R_{CP} values ($\sim$ 1.1) are significantly lower than the highest R_{AA} values ($\sim$ 2). This indirectly shows that Cu+Cu 40-60% $\sqrt{s_{NN}}$ = 200 GeV Λ and $\bar{\Lambda}$ yields are also enhanced relative to the p+p reference. A similar observation was first made for Au+Au $\sqrt{s_{NN}}$ = 200 GeV collisions [28].

At high-p_T ($p_T \gtrsim 5$ GeV/c), all R_{CP} values appear to converge to the measured charged hadron R_{AA} values of $\sim$ 0.5 for central Cu+Cu collisions. Assuming jet production dominates this region of phase space, this shows that high-p_T jet suppression occurs for central Cu+Cu collisions. It has been shown for peripheral Cu+Cu $\sqrt{s_{NN}}$ = 200 GeV collisions ($\langle N_{part}\rangle \sim$21) that charged hadron $R_{AA} \sim 1$ for the $p_T \gtrsim 5$ GeV/c which gives a charged hadron $R_{CP} \sim 0.5$ [135]. The value is consistent with the V0 values indicating a common production mechanism for charged hadron and neutral strange particles in the p_T range studied. Regarding Cu+Cu and Au+Au comparisons, this is not possible for V0 R_{CP} with $p_T \gtrsim 5$ GeV/c as the available Au+Au $\sqrt{s_{NN}}$ = 200 GeV yields [51, 84] have insufficient statistics in this p_T range. The charged hadron R_{AA} values for both systems with $\langle N_{part}\rangle \sim$ 100 have been shown to be consistent for $p_T \gtrsim 5$ GeV/c range. Therefore the differences in Cu+Cu and Au+Au geometry at given $\langle N_{part}\rangle$ that are important for soft strangeness production, appear to have little effect on hard charged hadron production.

6.3 Further Model Comparisons

Speculations with regard to the differing strangeness yields per participant trends for Cu+Cu and Au+Au $\sqrt{s_{NN}}$ = 200 GeV collisions, could be explored/qualified further with QCD dynamical string phenomenologies such as the previously mentioned RQMD and HIJING models. In running such models, once may assess how the differing longitudinal extents of the Cu+Cu and Au+Au collisions zones influence particle production via string breaking. The EPOS dynamical model [138, 139] offers an alternative view of particle production in heavy-ion collisions that may also explain the differences in Cu+Cu and Au+Au. In this model, the central region of the collision zone is labelled the *core* and is described via high density QCD string dynamics with a collective flow profile imposed. The core energy density decreases with time and hadronises when it reaches the critical value for QGP formation. Particle production in the *corona* region is governed low density QCD dynamics, and can be thought of as a superposition of p+p collisions.

Figure 6.11 shows both regions for a mid-central Au+Au collision. Regarding particle production, the ratio of the core contribution to the corona contribution increases with centrality. The EPOS model describes both non strange and strange particle yields per participant quite well, and predicts $R_{AA} > 1$ for mid-p_T Λ particles in central Au+Au 0-5% collisions as observed in figure 2.12. For strange particle production, the core contribution dominates for central Au+Au collisions and even commands the greater role for very peripheral Au+Au collisions ($\langle N_{part} \rangle \sim$ 14). When running the EPOS model for Cu+Cu collisions of a similar $\langle N_{part} \rangle$ to Au+Au, it is conceivable that the differing spatial geometries may lead to core being larger in Cu+Cu giving larger strange particle yields. Such an observation would give support to this novel idea of particle production in heavy-ion collisions.

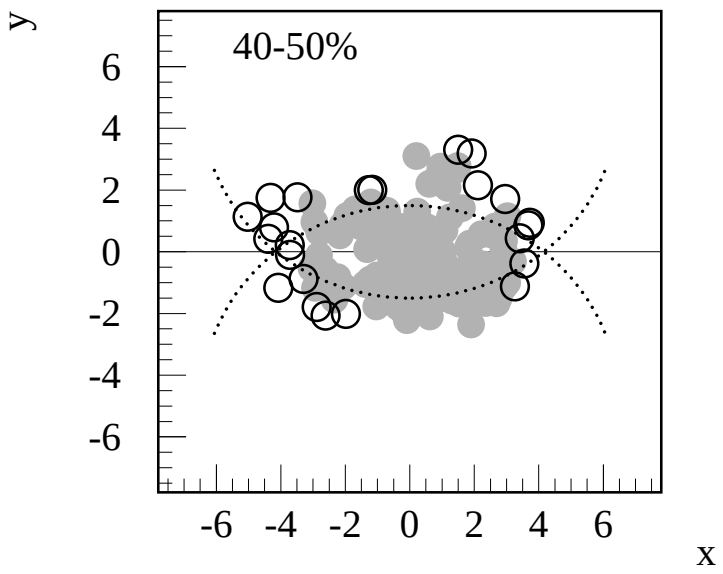

Figure 6.11: Schematic representation of the core (grey area) and corona (circles) in transverse plane of a mid-central Au+Au collision [139]. Units are fm.

Figure 6.12 shows preliminary mid-rapidity K^0_S yields for Cu+Cu and Au+Au $\sqrt{s_{NN}}$ = 62 GeV collisions as a function of $\langle N_{part} \rangle$ [137]. These follow the same pattern as the higher energy results which again highlights the importance of collisional geometry for strangeness production in heavy-ion collisions. This is expected as the 62 GeV energy sits between the AGS/SPS and RHIC 200 GeV energies. As with the Cu+Cu $\sqrt{s_{NN}} = 200$ GeV results, these observations merit energy density investigations and comparisons to QCD dynamical models to determine whether a consistent picture emerges.

For strangeness particle production with $p_T \gtrsim 2$ GeV, this study further warrants V0 yield coalescence predictions for the smaller system sizes. In particular, if they can reproduce the Cu+Cu and Au+Au differences for the Λ/K^0_S ratios and the Λ, $\bar{\Lambda}$ R_{AA} values observed, additional credibility will be given to this view of particle production. The same can be said for baryon junction models, and if one

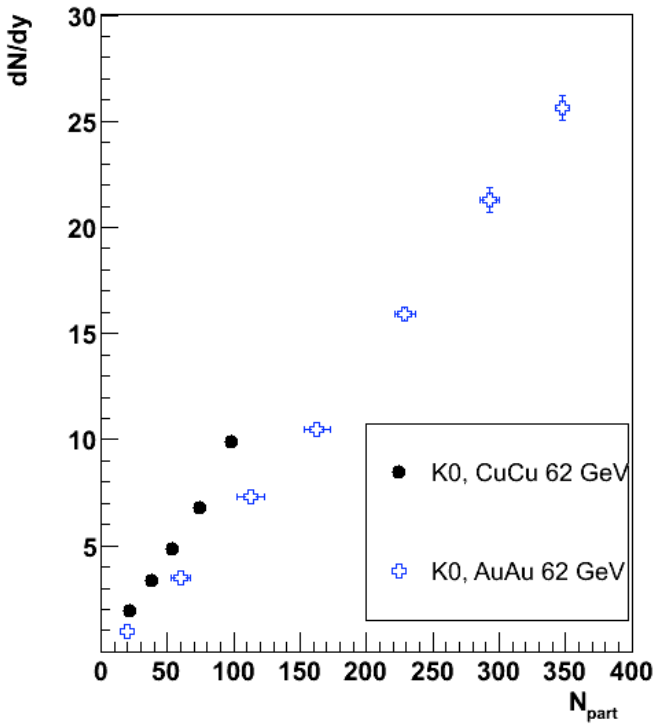

Figure 6.12: Mid-rapidity K^0_S yields for Cu+Cu and Au+Au $\sqrt{s_{NN}}$ = 62 GeV collisions as a function of $\langle N_{part} \rangle$ [137]. Uncertainties on dN/dy are statistical.

model succeeds and the other fails in reproducing the Cu+Cu and Au+Au differences, this will help resolve the current ambiguity with respect to mid-p_T production mechanisms. Finally, angular two particle correlation measurements such as those described in section 1.3.4, offer another possibility to determine the contribution of jet fragmentation to V0 yields. The results could be used to compare the soft and hard contributions to mid-p_T and high-p_T V0 spectra in a more model independent way.

Chapter 7

CONCLUSIONS

This study has shown that collision geometry plays a crucial role in bulk strangeness production for ^{63}Cu+^{63}Cu and ^{197}Au+^{197}Au collisions with $\sqrt{s_{NN}} = 200$ GeV. This manifests itself in mid-rapidity strangeness production per participant being higher in Cu+Cu collisions with $\langle N_{part} \rangle \gtrsim 60$ compared to Au+Au collisions of similar $\langle N_{part} \rangle$. The trend at lower centre of mass energies continues up to RHIC, and questions where the Canonical formalism is appropriate in describing strangeness yields in heavy-ion collisions. The role of energy density has been explored and a common scaling regime was found to describe both Cu+Cu and Au+Au strangeness yields per participant. Such an energy density calculation included the longitudinal dimensions of the colliding ions, and suggested that partons with an energy above 1-2 GeV may play a significant role in strangeness production. In QCD string phenomenology, higher energy densities may also correspond to increased colour rope formation which could also increase per participant strangeness yields. For either case, it was argued that such a scaling is meaningless if hadronic interactions dominate strangeness production thus indicating that partonic interactions assume the role.

Mid-p_T ($2 \lesssim p_T \lesssim 5$ GeV/c) Λ/K^0_S ratios were measured for Cu+Cu collisions, and also found to be higher compared to Au+Au collisions with similar $\langle N_{part} \rangle$. Consequently, the nuclear modification factor R_{AA} for central Cu+Cu and Au+Au

mid-central collisions was measured for the Λ, $\bar{\Lambda}$, and K^0_S particles. The Cu+Cu Λ and $\bar{\Lambda}$ values were found to be higher than the Au+Au values for the mid-p_T range, however both Cu+Cu and Au+Au K^0_S values were consistent in the same range. Such an observation was argued to be consistent with both a quark recombination scenario, and/or a QCD higher string constants in central Cu+Cu collisions. Finally, the other nuclear modification factor R_{CP} was measured at high-p_T ($p_T \gtrsim 5$ GeV/c) and found to be the same for the Λ, $\bar{\Lambda}$ and K^0_S particles at a value of ~ 0.5. This was also consistent with charged hadron values, and because it is less than 1, shows that high-p_T suppression occurs for strange particles in central Cu+Cu collisions.

Appendix A

CUTS FOR CASCADE ANALYSIS

Tables A.1 and A.2 show the topological cuts used to extract cascade yields for the feed down calculation in section 5.5, and figure A.1 shows a cascade topology. The topological cut tuning used the method outlined in section 5.2.2 suitably adjusted for cascades. The bachelor and V0 daughters have $N_{sigma} < 3$ dE/dx placed on them, and there was also a requirement for the bachelor and both V0 daughters to have > 15 TPC hits. Finally, the Ξ^- and $\bar{\Xi}^+$ invariant mass backgrounds were calculated with a 2^{nd} order polynomial fits in order to extract the raw yield.

Cascade Topology	$p_T < 1$ GeV/c	$1 \leq p_T < 3$ GeV/c	$p_T \geq 3$ GeV/c
Decay Length	> 3.6 cm	> 4.3 cm	> 4.8 cm
DCA Bachelor to V0	< 0.8 cm	< 0.8 cm	< 0.8 cm
DCA Cascade to PV	< 0.8 cm	< 0.8 cm	< 0.8 cm
DCA of Bachelor to PV	> 1 cm	> 0.5 cm	> 0 cm

Table A.1: Analysis cuts applied to the Cascades. p_T refers to that of the V0. PV is an abbreviation for Primary Vertex, and DCA is Distance of closest Approach. The conditions apply to the Cascade candidates retained.

V0 Topology	$p_T < 1$ GeV/c	$1 \leq p_T < 3$ GeV/c	$p_T \geq 3$ GeV/c
V0 Vertex to PV	> 0 cm	> 0 cm	> 0 cm
DCA V0 Daughters	< 0.8 cm	< 0.8 cm	< 0.8 cm
DCA V0 to PV	> 0.3 cm	> 0.1 cm	> 0 cm
DCA of Pos Daug to PV	> 0.5 cm	> 0.5 cm	> 0.5 cm
DCA of Neg Daug to PV	> 0.5 cm	> 0.5 cm	> 0.5 cm

Table A.2: Analysis cuts applied to the V0s associated with the Cascades. p_T refers to that of the V0. Pos is an abbreviation for Positive, Neg is Negative, Daug is Daughter, PV is Primary Vertex, and DCA is Distance of closest Approach. The conditions apply to the Cascade candidates retained.

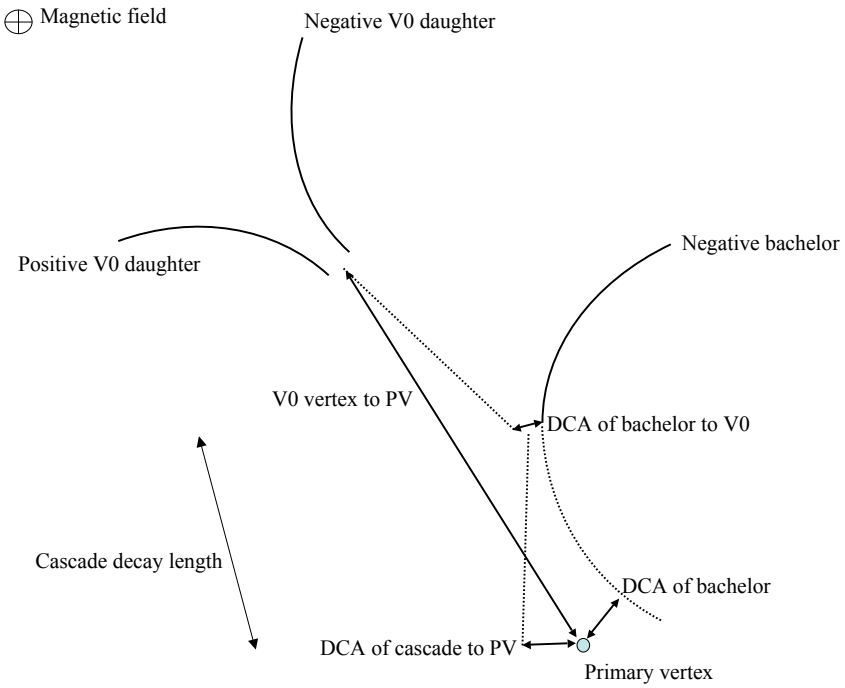

Figure A.1: Topology of a negative cascade. See figure 5.1 for more on the V0 topology.

References

[1] Raymond Brock et al., *Handbook of perturbative QCD: Version 1.0.* Rev. Mod. Phys. 67 (1995) 157

[2] F. Abe et al., Phys. Rev. Lett. 61 (1988) 1819

[3] M. Gell-Mann, Phys. Lett. 8 (1964) 214

[4] J. D. Bjorken and E. A. Paschos, Phys. Rev. 185 (1969) 1975

[5] D. H. Perkins, *Introduction to High Energy Physics*, Cam. Uni. Press 4th Ed,

[6] C. Berger et al., Phys. Lett. B 86 (1979) 418

[7] S. Eidelman, et al., Phys. Lett. B 592 (2004) 1

[8] S. Bethke, J.Phys. G26 (2000) R27

[9] B. Andersson et al., Phys. Rep. 97 (1983) 31

[10] N. F. Mott., Rev. Mod. Phys. 40 (1969) 677

[11] E. Kolb and M.S. Turner, The Early Universe (Addison-Wesley, RedwoodCity, 1990)

[12] M. Alford, J. Berges, K. Rajagopal, Nucl. Phys. B571 (2000) 269

[13] D.H. Rischke, Prog. Part. Nucl. Phys. 52 (2004) 197

[14] F. Karsch., Nucl. Phys. A 698 (2002) 199

[15] O. Kaczmarek, F. Karsch, E. Laermann and M. Lutgemeier, Phys. Rev. D 62 (2000) 034021

[16] F. Karsch, Lecture Notes in Physics 583 (2002) 209.

[17] I. R. Kenyon, *Elementary Particle Physics* (Routledge and Kegan Paul, 1987)

[18] Z. Fodor and S.D. Katz, JHEP 0404 (2004) 050.

[19] C. R. Alltonet al., Phys. Rev. D 66 (2002) 074507; Phys. Rev. D 71 (2005) 054508

[20] R.V. Gavai and S. Gupta, Phys. Rev. D 71 (2005) 114014

[21] Z. Fodor and S. D. Katz, Phys. Lett. B534 (2002) 87; Z. Fodor and S.D. Katz, JHEP 0203 (2002) 014

[22] J. Adams et al. (STAR Collaboration), Nucl. Phys. A 757 (2005) 102

[23] J. Rafelski and B. Müller, Phys. Rev. Lett. 48 (1982) 1066

[24] P. Koch, B. Müller, and J. Rafelski, Phys. Rep. 142 (1986) 167

[25] P. Koch et al., Phys. Rep. 142 (1986) 169

[26] J. Schaffner-Bielich, J.Phys. G30 (2004) R245

[27] E. Andersen et al. (WA97), Phys. Lett. B 449 (1999) 401; F. Antinori et al. (WA97/NA57), Nucl. Phys. A 698 (2002) 118c

[28] B.I. Abelev et al. (STAR Collaboration), arXiv:0705.2511v1 [nucl-ex]

[29] B. Back et al. (PHOBOS Collaboration), Phys. Rev. C 70 (2004) 021902

[30] B.I. Abelev et al. (STAR Collaboration), arXiv:nucl-ex/0703040v1

[31] J. Adams et al. (STAR Collaboration), Phys. Rev. C 71 (2005) 044906

[32] D. Kharzeev, Phys. Lett. B 378 (1996) 238

[33] J. D. Bjorken. Energy loss of energetic partons in quark - gluon plasma: Possible extinction of high momentum jets in hadron - hadron collisions. FERMILAB-PUB-82-059-THY

[34] R. Baier et al., Nucl. Phys. B 483(1997) 291

[35] M. Gyulassy and M. Plumer, Phys. Lett. B 243 (1990) 432

[36] J. Adams et al. (STAR Collaboration), Nucl. Phys. A 757 (2005) 102

[37] S. Adler et al. (PHENIX Collaboration), Phys. Rev. Lett. 96 (2006) 202301

[38] I. Vitev and M. Gyulassy, Phys. Rev. Lett. 89, 252301 (2002); I. Vitev, J. Phys. G 30 (2004) S791

[39] D. Antreasyan, J. W. Cronin et. al., Phys. Rev. D 19 (1979) 764

[40] J. Adams et al. (STAR Collaboration), Phys. Lett. B 595 (2004) 143

[41] L Ahle et al., Phys. Rev. C 60 (1999) 044904.

[42] C Höhne (NA49 Collaboration), Nucl. Phys. A 715 (2003) p474

[43] Helen Caines for the STAR Collaboration, J.Phys. G31 (2005) S101

[44] M. Miller, *Ph.D.Thesis*, Yale University, (unpublished) December 2003

[45] T. Trainor and D. J. Prindle, arXiv:hep-ph/0411217v3

[46] J. D. Bjorken, Phys. Rev. D27 (1983) 140

[47] J. Adams et al. (STAR Collaboration), Phys. Rev. C 70 (2004) 054907

[48] K. Adcox et al. (PHENIX Collaboration), Nucl. Phys. A 757 (2005) 184

[49] A. Krasnitz, Y. Nara and R. Venugopalan, Nucl. Phys. A 717 (2003) 268.

[50] R. Hagedorn, Riv. Nuovo Cimento 6 (1983) 1

[51] J. Adams et al. (STAR Collaboration), Phys. Rev. Lett. 98 (2007) 062301

[52] S. Steinke, J. Rafelski, J.Phys. G32 (2006) S455

[53] I. G. Bearden et al. (NA44 Collaboration) Phys. Rev. Lett. 78 (1997) 2080

[54] F. Retiere and M. Lisa, Phys. Rev. C 70 (2004) 044907

[55] E. Schnedermann et al., Phys. Rev. C 48 (1993) 2462

[56] O. Barannikova for the STAR Collaboration, nucl-ex/0403014

[57] C. Adler et al. (STAR Collaboration), Phys. Rev. Lett. 89 (2002) 092301; J. Adams et al. (STAR Collaboration), Phys. Lett. B 595 (2004) 143; J. Adams et al. (STAR Collaboration), Phys. Rev. C 70 (2004) 041901; J. Adams et al. (STAR Collaboration), nucl-ex/0406003.

[58] J. Cleymans and K. Redlich, Phys. Rev. C 60 (1999) 054908

[59] J. Adams et al. (STAR Collaboration), Phys. Rev. Lett. 92 (2004) 182301

[60] F. Becattini and U. Heinz, Z. Phys. C 76 (1997) 269; F. Becattini, A. Giovannini, and S. Lupia, Z. Phys. C 72 (1996) 491

[61] B I Abelev et al. (STAR Collaboration), Phys. Rev. C 75 (2007) 064901

[62] J. Hormuzdiar, S. D. H. Hsu, and G. Mahlon, Int. J. Mod. Phys. E 12 (2003) 649

[63] M.C. Abreu et al. (NA50 Collaboration), Phys. Lett. B 410 (1997) 337

[64] A. Adare et al. (PHENIX Collaboration), arXiv:nucl-ex/0611020v1

[65] G. Agakishiev et al. (CERES Collaboration) Phys. Rev. Lett. 75 (1995) 1272

[66] G. Agakishiev et al. (CERES Collaboration) Phys. Lett. B 422 (1998) 405

[67] D. Adamova et al. (CERES Collaboration) Phys. Rev. Lett. 91 (2003) 042301

[68] P. Braun-Munzinger and J. Stachel, Nature 448 (2007) 302

[69] J. Adams et al. (STAR Collaboration), Phys. Rev. Lett. 92 (2004) 052302

[70] J. Adams et al. (STAR Collaboration), Phys. Rev. Lett. 92 (2004) 052302

[71] S. S. Adler et al. (PHENIX Collaboration), Phys. Rev. Lett. 91 (2003) 182301

[72] P. F. Kolb and U. Heinz, in Quark Gluon Plasma 3, eds. R.C. Hwa and X.N. Wang (World Scientific, Singapore, 2003), nucl-th/0305084; P. Huovinen, P.F. Kolb, U. Heinz, P.V. Ruuskanen and S. A. Voloshin, Phys. Lett. B 503 (2001) 58; C. Adler et al. (STAR Collaboration), Phys. Rev. Lett. 87 (2001) 182301

[73] S. S. Adler et al. (PHENIX Collaboration), Phys. Rev. C 69 (2004) 034909

[74] N. S. Amelin et al., Phys. Rev. C 44 (1991) 1541; N. S. Amelin et al., Phys. Rev. C 47 (1993) 2299

[75] H. Sorge, H. Stöcker, and W. Greiner, Nucl. Phys. A 498(1989) 567c; H. Sorge, H. Stöcker and W. Greiner, Ann. Phys. N.Y. 192 (1989) 266

[76] F. Wang et al., Phys. Rev. C 61 (2000) 064904

[77] P. Braun-Munzinger et al., Nucl. Phys. A 697 (2002) 902

[78] O. Fochler, Phys. Rev. C 74 (2006) 034902

[79] J. Letessier and J. Rafelski, *Hadrons and Quark-Gluon Plasma* Cam. Uni. Press

[80] A. Tounsi and K. Redlich, arXiv:hep-ph/0111159v1; J. Cleymans, K. Redlich and E. Suhonen, Z. Phys. 51, 137(1991)

[81] M. J. Tannenbaum, Eur. Phys. J. C 43 (2005) 329; J. Phys. Conf. Ser. 27 (2005) 1

[82] J. Adams et al. (STAR Collaboration), Phys. Rev. D 74 (2006) 032006

[83] G. Wilk and Z. Wlodarczyk, Physica A (Amsterdam) 305 (2002) 227

[84] J. Adams et al. (STAR Collaboration), nucl-ex/0601042

[85] B. I. Abelev et al.(STAR Collaboration), Phys. Lett. B 655 (2007) 104

[86] V. Greco, C. M. Ko, P. Levai, Phys. Rev. C 68 (2003) 034904, Phys. Rev. Lett. 90 (2003) 202302

[87] R.J. Fries, B. Muller, C. Nonaka, S.A. Bass, Phys. Rev. C 68 (2003) 044902

[88] I. Vitev and M. Gyulassy, Phys. Rev. C 65 (2002) 041902

[89] M. A. C. Lamont, Brookhaven National Laboratory, *private communication*

[90] V. T Pop et al., Phys. Rev. C. 75, (2007) 014904

[91] J. Adams et al. (STAR Collaboration), Phys. Rev. Lett. 91 (2003) 072304

[92] M. Harrison et., Nucl. Inst. and Meth. A 499 (2003) 235

[93] `http://www.bnl.gov/rhic/RHIC_complex.htm`

[94] K.H. Ackermann et al., Nucl. Inst. and Meth. A 499 (2003) 659

[95] K.H. Ackermann et al., Nucl. Inst. and Meth. A 499 (2003) 630

[96] M. Shao et al. Nucl. Inst. and Meth. A 558 (2006) 419

[97] G. Van Buren et al., Nucl. Inst. and Meth. A 566 (2006) 22

[98] R. Bossingham et al. Technical report, STAR Note 281, STAR Offline Simulations and Analysis Software Design, 1997.

[99] STAR Computing Group, Brookhaven National Laboratory USA

[100] H. Bichsel, Comparison of Bethe-Bloch and Bichsel Functions, STAR Note 439.

[101] W M Yao et al., J. Phys. G: Nucl. Part. Phys. 33 (2006) 1

[102] `www.rhic.bnl.gov/RCF/`

[103] `http://www.cern.ch/minuit`

[104] M. Van Leeuwen, Utrecht University, *private communication*

[105] James Dunlop, Brookhaven National Laboratory, *private communication*

[106] M. Calderon, *Ph.D.Thesis*, Yale University, (unpublished) May 2001

[107] L. Ray and M. Daugherity, arXiv:nucl-ex/0702039v1

[108] A. Bialas et al., Nucl. Phys. B 111 (1976) 46

[109] D. Kharzeev and M. Nardi, Phys. Lett. B 507 (2001) 121

[110] S. Eidelman et al., Phys. Lett. B 592 (2004) 1

[111] C. Adler et al. (PHENIX Collaboration), Phys. Rev. C 71 (2005), 034908

[112] B. B. Back et al. (PHOBOS Collaboration) Phys. Rev. C70 (2004) 021902

[113] X.-N. Wang, M. Gyulassy, Phys.Rev.Lett. 86 (2001) 3496-3499

[114] J. Adams et al. Phys. Rev. Lett. 92 (2004) 112301

[115] J. Adams et al. Phys. Lett. B 655 (2007) 104

[116] B.Alver et al. (PHOBOS Collaboration), arXiv:0709.4008v1

[117] R. E. Ansorge et al., Z. Phys. C 43 (1989) 357

[118] J. Berger, *Ph.D.Thesis*, University of Frankfurt, (unpublished) November 2003

[119] A. Tang, *Ph.D.Thesis*, Kent State University, (unpublished) May 2002

[120] J. Podolanski and R. Armenteros, Phil. Mag. 45 (1945) 13

[121] L. S. Barnby, University of Birmingham, *private communication*

[122] P. G. Jones, University of Birmingham, *private communication*

[123] `http://wwwasdoc.web.cern.ch/wwwasdoc/geantold/GEANTMAIN.html`

[124] B. Lasiuk et al., TPC Respose Simulator, User Guide and Reference Manual, Internal STAR Documentation, Rev. 1.4 (2000).

[125] Y. Fisyak, Brookhaven National Laboratory, *private communication*

[126] M. Lamont, *Ph.D.Thesis*, University of Birmingham, (unpublished) January 2002

[127] H. Jiang, *Ph.D.Thesis*, University of California Los Angeles, (unpublished) 2005

[128] A. Iordanova for STAR Collaboration, arXiv:0710.3902v1

[129] M. Lamont for the STAR Collaboration, J. Phys. G32: (2006) S105

[130] S. Baumgart for the STAR Collaboration, arXiv:0709.4223v1

[131] J. P. Blaizot, A.H. Mueller, Nucl. Phys. B 289 (1987) 847; K. Kajantie, P.V. Landshoff, J. Lindfors, Phys. Rev. Lett. 59 (1987) 2527

[132] A.H. Mueller, Nucl. Phys. B335 (1990) 115; A. H. Mueller, Nucl. Phys. B 572 (2002) 227

[133] T. Falter and U. Mosel, Phys. Rev. C. 66 (2002) 024608

[134] C. Loizides, Eur. Phys. J. C49 (2007) 339

[135] B. Alver et al. (PHOBOS Collaboration), Phys. Rev. Lett. 96 (2006) 212301

[136] J. Adams et al. (STAR Collaboration), Phys. Rev. Lett. 91 (2003) 172302

[137] M. G. Munhoz, University of São Paulo, *private communication*

[138] K. Werner, F. Liu, and T. Pierog, Phys. Rev. C 74 (2006) 044902

[139] K. Werner, Phys. Rev. Lett. 98 (2007) 152301